Enhancing Predictions of Carbonate Dissolution Behavior Using Quantitative Heterogeneity Metrics from XCT Data

by

Ellen P. Thompson

A dissertation submitted in partial fulfillment
of the requirements for the degree of
Doctor of Philosophy
(Environmental Engineering)
in the University of Michigan
2024

Doctoral Committee:

Associate Professor Brian R. Ellis, Chair
Professor Udo Becker
Associate Professor Aline J. Cotel
Professor Valeriy Y. Ivanov
Associate Professor Christian M. Lastoskie

Ellen P. Thompson

ellenpt@umich.edu

ORCID iD: 0000-0003-4418-8976

Dedication

To John, for supporting me through all the ups and downs of grad school.

Acknowledgements

This dissertation was funded by the National Science Foundation (CAREER Grant 1943726), the Alfred P. Sloan Foundation (Grant 2020-12466), and the University of Michigan Department of Civil and Environmental Engineering.

I would like to thank my advisor, Dr. Brian Ellis, for his guidance and support over the past six years. I am sincerely grateful for his enthusiasm and mentorship as I pursued my research interests. I would also like to thank the members of my dissertation committee. Dr. Christian Lastoskie has been incredibly supportive through my MSE and PhD, connected me with mentors in the department, and provides helpful perspective on how my research fits into the real world of energy infrastructure. Dr. Aline Cotel has been a knowledgeable and enthusiastic mentor ever since I met her in the Stream Restoration class. She provides a wonderful example of how to do impactful fundamental research connected with the global community. Dr. Valeriy Ivanov taught one of the most useful courses of my graduate career, Data Analysis in CEE, and continues to be very supportive as I navigate new statistical methods. Dr. Udo Becker welcomed me into his lab when I was a master's student and provided me with important mentors in the Earth Sciences department and thoughtful feedback on my research. Thank you all for your advice and guidance.

This research would not have been possible without the support of many individuals in the CEE department and greater University of Michigan community. Thank you to Dr. Owen Neill and Dr. Zhongrui Li and the Electron Microbeam Analysis Lab for your training and

assistance. Thank you to Dr. Matt Friedman, Dr. Selena Smith, and the CTEES users for your training, collaboration, and troubleshooting of the XCT instrument. Thank you to Tom Yavaraski for your patience and dedication to educating CEE lab users in safety and instrumentation. Thank you to the CEE administrative and student services staff for all of your support and community.

I am immensely grateful to the CEE graduate students I have gotten to know during my time at Michigan. Thank you first to Dr. Anne Menefee for training me on every instrument, welcoming me to the lab group, and being my conference and lab buddy from day one. Thank you to Dr. Jubilee Adeoye, Dr. Ivan Jayawan, and Dr. Wenjia Fan for teaching me so much when I was a new graduate student. Thank you to Kira Tomenchok and Tyler Olson for navigating our first publication experience together, over Zoom during the Covid pandemic. Thank you to Eva Albalghiti for your wisdom, laughter, camaraderie, and advice – I couldn't do this without you. I am forever grateful to the friends I have made in the CEE department during my time at Michigan, including (but not limited to!) Hollie Adejumo, Mira Chaplin, Dr. Kate Dowdell, Maddy Fairley-Wax, Tim Fairley-Wax, Dr. Xavier Fonoll, Kate Harrison, Dr. Katie Langenfeld, Dr. Ernesto Martinez, Dr. Sarah Potgieter, Pedro Puente, Dr. Raghav Reddy, Dr. Maggie Reuter, Dr. Nicole Rockey, Renata Starostka, Dr. Caroline Van Steendam, Dr. Matt Vedrin, Dr. Brett Wagner, and Dr. Kuang Zhu. Thank you all for being my community and sharing the ups and downs of grad school.

Thank you to my friends and family, near and far, who have provided steadfast support and healthy perspective during the tough parts of graduate school.

Thank you to my husband, Dr. John Thompson, for being my partner through all of it.

Table of Contents

Lists of Tables

List of Figures

List of Appendices

Abstract

Carbonate rock formations are common targets for sustainable subsurface energy development, but their chemical reactivity with injection fluid creates complex dissolution pathways that are difficult to predict. Improving predictions of the physical changes that occur in formations due to chemical dissolution is essential for assessing the long-term viability of such projects. X-ray computed tomography (XCT) imagery is commonly used to study rock core samples because it allows for nondestructive 3D visualization of the pore space. Pore network heterogeneities observed from XCT are expected to affect larger-scale reactive transport behavior, but most of the work in this space to date has been done through numerical simulations. Few studies have tested the impact of these heterogeneities in laboratory studies of natural rock samples. In this dissertation, quantitative metrics of heterogeneity were developed from XCT images of limestone samples and tested for their ability to predict various aspects of dissolution. A first step in analyzing XCT data is segmentation of the dataset into pore and mineral space. This step is prone to user subjectivity and has substantial impact on subsequent interpretations of the data. Various combinations of three image processing filters were tested on XCT datasets prior to segmentation, and the use of all three filters in sequence resulted in more consistent porosity estimates that were significantly closer to experimental values. Porosity is a primary characteristic used to predict downstream petrophysical parameters, including permeability, so accurate assessment of porosity is paramount. This filtering process was used in all subsequent studies. Next, a series of core flooding experiments were performed on three

limestones with different diagenetic properties. Cores were XCT scanned before and after dissolution by dilute acid in a high-pressure flowthrough apparatus. Persistent homology was applied to analyze the topology of the pore space in three limestones and observe changes in pore size, connectivity, and spatial distribution. It was observed that permeability increase was driven by the growth of large, connected pore bodies. In the core with the highest degree of along-core heterogeneity prior to reaction, pore sizes became more homogenous due to dissolution. Pore growth was particularly pronounced in pores that were locally large but not the largest in the core. Being able to predict regions with high or low pore size increase could help improve the efficiency of models of larger-scale behavior. Next, fractal dimension was used to investigate the pore space complexity of the limestone samples. Spectral analysis was used to study how the relevant spatial scales of heterogeneity evolved due to dissolution. Smaller heterogeneities lessened in importance, and larger heterogeneities contributed more to overall variance after reaction, suggesting that a larger scale of observation with lower resolution would be preferable after dissolution. The preferential flowpath that developed in each core was isolated; its fractal dimension showed good positive correlation with that of the initial pore space, suggesting that rocks with geometrically complex pore space are likely to experience more complex branching behavior. Optimizing spatial resolution and scale is essential for improving simulations that upscale the phenomena observed in the laboratory. This dissertation contributes to a growing body of work in characterizing carbonate core samples and using those characterizations to predict reactive transport behavior during dissolution. Improving predictions of dissolution behavior is essential for the implementation of sustainable subsurface energy technologies.

Chapter 1 Introduction

1.1 Motivation

Widespread scientific evidence suggests that global climate change has been accelerated by post-industrial anthropogenic greenhouse gas (GHG) emissions, especially CO_2. In the United States, the electric power sector remains a major source of GHG emissions, accounting for 25% of GHG emissions in 2021 (EPA, 2023). Mitigating the harm of global climate change requires a transition from traditional fossil fuel sources to carbon-neutral and carbon-negative energy technologies. Geologic carbon capture, sequestration, and utilization (CCUS) has great potential for reducing CO_2 emissions in the energy sector (Celia, 2017). CO_2 captured at point sources or through direct air capture can be injected into the subsurface for permanent geologic sequestration, creating a carbon sink to reduce atmospheric CO_2 concentrations. Utilization of CO_2 in the subsurface has shown promise as well. Subsurface reservoirs could be used for compressed gas energy storage, providing additional energy storage capacity to the grid to enable implementation of intermittent renewable energy sources like wind and solar. CO_2 also has advantageous thermodynamic properties that would make it an effective working fluid in geothermal energy production systems (Adams et al., 2014; Randolph & Saar, 2011). For the success of all of these technologies, reliable prediction of fluid flow through the subsurface is essential. Precise characterization of target formations to predict their flow characteristics is challenging due to their setting in the deep subsurface. Rock core samples from target formations are collected and analyzed in a laboratory setting. In systems where percolation through porous media dominates transport, core sample pore characteristics are used to predict upscaled

reservoir parameters, including permeability and flow dynamics, and are a starting point for forecasting changes in formation behavior over time (Hommel et al., 2018; Ma, 2015; Mostaghimi et al., 2013). Improvement in core sample characterization methods therefore has great potential for impact in the transition to a lower-carbon energy mix.

1.2 Subsurface reactive transport

Carbonate formations (e.g., limestones, dolomites) are common targets for subsurface storage and energy production because they are porous (large storage capacity), permeable (easy to inject), and widely distributed. Carbonates readily dissolve when injected with acidic fluid and can create complex channels of dissolution that are difficult to predict.

Numerous prior works have highlighted the importance of reactive transport regimes in the progression of porosity and permeability in dissolving carbonates. This regime is defined by dimensionless parameters: the advective and diffusive Damköhler numbers (Da_I and Da_{II}, respectively) and the Péclet number (Pe). The Damköhler number describes whether a system is controlled by the transport of reactants or by chemical kinetics. Da_I is defined as the ratio of the characteristic time of advection to the characteristic time of reaction. A system with high Da_I is, therefore, transport-limited: the reactant is consumed faster than the system can carry it to the reaction sites. Likewise, Da_{II} is defined as the ratio of characteristic time of diffusion to characteristic time of reaction. The Péclet number describes the primary mode of transport within a system and is defined as the ratio of characteristic time of diffusion to characteristic time of advection. In a system with high Pe, advection is the primary mode of transport. Prior works have connected these parameters to the characteristics of the reaction front. In a study of porosity-permeability relationships in dissolving limestones, moderate positive values of Da_I yielded the greatest permeability increase for a given porosity increase (Luquot & Gouze, 2009).

Low Da_I and high Pe have been associated with uniform dissolution, moderate Da and high Pe with wormholing, and high Da with face dissolution (dissolution regimes described in more detail below) (Kang et al., 2003; Liu & Mostaghimi, 2017; Menke et al., 2015; Mostaghimi et al., 2016; Qi et al., 2018; Zhang et al., 2022). Dissolution is found to be particularly sensitive to pore space heterogeneity in systems with high Pe and Da (Zhang et al., 2022).

The progression of the reaction front through the dissolving rock tends to follow one of four patterns: (1) uniform dissolution, (2) face dissolution, (3) wormholing, or (4) mixed dissolution. (1) Uniform dissolution tends to occur at very high injection rates with slow chemical kinetics because reactive fluid reaches all areas of the core before it is consumed. (2) Face dissolution tends to occur at very low injection rates so that the reactant is consumed near the injection point and flow through the remainder of the core is nonreactive. (3) Wormholing can occur at moderate injection rates, where advection has time to carry reactive fluid along the length of a main flow channel, but dispersion does not have time to spread the fluid throughout the full area of the core before reaction occurs. (4) Mixed dissolution describes dissolution that shares characteristics of multiple other types (Fredd & Fogler, 1999; Seigneur et al., 2019). Predicting which pattern a system is expected to follow is important, as different dissolution regimes influence different porosity-permeability relationships and thus different long-term formation behaviors.

In engineered subsurface energy systems, site selection and characterization is paramount. Injection speed and chemistry can be controlled to target a specific reactive transport regime for the desired application. Uniform dissolution may be preferable for some applications to increase the volumetric capacity of the pore space within a smaller areal footprint. In others, creating channels of high permeability can be beneficial to carry reactive fluid to distal regions

of the formation. The ability to change these conditions to optimize system performance is dependent on the ability to effectively characterize the reservoir host rock. Core plug samples that are centimeters in length are collected from various areas and depths of a target formation to estimate the petrophysical characteristics of the rock. These are analyzed using a variety of experimental and imaging techniques, and those parameters are used to inform models of system performance.

1.3 X-ray computed tomography

X-ray computed tomography (XCT) is a nondestructive imaging technique that allows for 3D visualization of rock material, making it a highly useful tool for analyzing pore structures *in situ*. The rise in the availability of bench-scale XCT instruments has led to great advances in 3D characterization of geomaterials (Wildenschild & Sheppard, 2013). Its applications are numerous: in addition to providing porosity information, XCT data have been used to characterize many other aspects of the pore space, including mineralogy (Carroll et al., 2013; Qin & Beckingham, 2019), reactive surface area (Lai et al., 2015), pore space fractal dimension (Alfonso et al., 2018; Wu et al., 2019; Xia et al., 2019), pore connectivity (Nakashima & Kamiya, 2007; Qajar & Arns, 2022; Ruspini et al., 2021), wettability and contact angle (Alhammadi et al., 2018; Guo et al., 2020), and saturation (Manoorkar et al., 2021; Sell et al., 2016). Others have simulated transport through porous media using simulation on XCT images (Bijeljic, Mostaghimi, et al., 2013; Bijeljic, Raeini, et al., 2013; Menke et al., 2021; Mostaghimi et al., 2013). All these are possible without physical or chemical damage to the sample, leaving it intact for further analysis.

In an XCT scanner, a cone of X-rays passes through the sample and is captured using a 2D detector at the far end of the scanner. The sample is rotated by small increments, creating

thousands of projections taken at different angles that are then reconstructed into a 3D dataset. The sample material attenuates the X-ray beam, so that each resulting image consists of dark areas where the beam passed through void space and bright areas where the beam passed through dense material. The Lambert-Beer law states that the grayscale value produced by the attenuated X-ray beam is a function of the material thickness and its X-ray attenuation coefficient; however, this law only applies to monochromatic X-ray beams. Bench-scale XCT scanners produce polychromatic X-ray beams, for which the Lambert-Beer law does not apply, meaning that further interpretation is required to quantify the amount of rock material that the beam passes through prior to detection (Wildenschild & Sheppard, 2013).

Great progress has been made in applying and utilizing XCT characterization, but the technology still has some limitations. Compared to other microscopy techniques, bench-scale XCT is a relatively low-resolution method. Bench-scale XCT scanners typically have a voxel resolution limit of around 1-10 μm. This resolution is limited by the diameter of the sample being imaged, as the sample must be far enough from the X-ray source to rotate a full 360° while keeping the full sample width perpendicular to the X-ray beam within the field of view (Cnudde & Boone, 2013). Resolution has been found to impact the accuracy of rock property estimates and the scale of the representative elementary volume (Bazaikin et al., 2017; Huang et al., 2021). Synchrotron scanners use a parallel X-ray beam that allows for geometric magnification and can, therefore, achieve higher (sub-micron) resolution, but they are prohibitively expensive and facilities are limited (Baruchel et al., 2006; Cnudde & Boone, 2013). It is, therefore, of great importance to improve the efficacy and analyze the predictive capacity of digitally derived rock characteristics that can be obtained using bench-scale XCT scanners.

To be useful for any of the above applications, an XCT dataset must first be segmented into its constituent parts: mineral versus pore space. Because the features of interest in a rock sample are often at or below the scale of observation, this process is nontrivial. Most voxels will contain some fraction of mineral and pore space, and their grayscale values will fall somewhere between that of pure rock or pure void, demonstrating so-called "partial-volume effects" (Cnudde & Boone, 2013). Still, prior work has found that coarse imagery with a large amount of partial-volume effects can still contain valuable characteristic information (Louis et al., 2007).

1.4 Research objectives

Previous studies have illustrated the importance of physical heterogeneity within porous rock material in controlling reaction processes under a given reactive transport regime. Liu and Mostaghimi (2017) studied the influence of pore space heterogeneity on dissolution behavior using statistically generated flow fields with different correlation lengths. They found that larger correlation length (i.e., more heterogeneity) is associated with more uniform dissolution or wormholing regimes, and less face dissolution. Navarre-Sitchler and Jung (2017) generated reactive transport models to study the effect of initial permeability heterogeneity and anisotropy on geochemical reaction rates; they found that preferential flow paths were more likely to develop in the more heterogeneous system. These and other numerical studies use statistically generated flow fields that are informed by natural rock characteristics but do not directly represent real samples and therefore cannot be compared to experimental data. Al-Khulaifi et al., (2017) mimicked layered heterogeneity by stacking limestone and dolomite core samples and found that physical heterogeneity had a greater influence than intrinsic reaction rates on the effective reaction rates in dissolving core samples. Few studies have made quantitative assessments of heterogeneity from natural rock samples.

The purpose of this dissertation is to use XCT scans of natural rock samples to develop quantitative metrics of structural heterogeneity and assess their utility in predicting experimentally observed dissolution behavior. Use of these metrics can aid in improving predictions of reactive flow behavior in the subsurface, which is essential for the implementation of sustainable subsurface technologies.

1.5 Chapter summaries

Chapter 2 studies the influence of image processing methods on the interpretation of XCT data. The work in this chapter lays a foundation for the work in subsequent chapters by studying the optimal methods for processing XCT data that yield the most accurate and precise results. XCT scans of three limestone and sandstone core samples were subjected to various combinations of three possible image filters: noise reduction, contrast enhancement, and beam hardening correction. The core sample porosity and pore size distributions were compared to experimental values. A computational fluid dynamics (CFD) model was developed to model nonreactive flow through one core, and simulated permeability was compared to laboratory results. It was found that the combination of all three filters resulted in lower porosity variance and values closer to experimental values for both limestones when compared to the unfiltered dataset. The use of the three filters also yielded a closer permeability value to experimental results than the unfiltered dataset. Pore size distributions were studied, but the difference in size detection limits between experimental and digital methods restricted meaningful comparison. These results suggest that the use of image filters could significantly improve digitally derived estimates of physical rock properties. These filters were used for all digital rock analysis for both Chapters 3 and 4. The work in this chapter was published in the peer-reviewed journal article referenced below. Author contributions follow: Ellen P. Thompson performed conceptualization,

writing, and formal analysis. Kira Tomenchok contributed to conceptualization and methodology. Tyler Olson aided in the investigation. Brian R. Ellis supervised and oversaw review and editing.

> **Thompson, E.P.;** Tomenchok, K.; Olson, T.; Ellis, B.R. Reducing user bias in X-ray computed tomography-derived rock parameters through image filtering. *Transport in Porous Media* **2021**, *140*, 493-509.

Chapter 3 studies the influence of pore space topology on pore size evolution in dissolving carbonates. Accurate prediction of pore size change in dissolving carbonates is important for a variety of subsurface applications, as regions of dramatic pore size increase influence system permeability and reactive transport behavior. In this study, three limestone cores were imaged using XCT before and after acid-promoted dissolution. Persistent homology was used to characterize the size, connectivity, and spatial distribution of the macropores within each core sample. All three rocks experienced the greatest size change in already large, connected pores. The sample with the greatest pore size heterogeneity prior to reaction experienced an increase in along-core pore size homogeneity after reaction. The samples with the greatest variance in persistence (a proxy for spatial clustering) experienced the greatest pore body size increase. These findings suggest that persistence heterogeneity analysis of core samples could be used to predict regions of greatest pore size evolution in a dissolving carbonate. This knowledge is beneficial for increasing confidence in the safety and sustainability of subsurface energy development projects. The work in this chapter was published in the peer-reviewed journal article referenced below. In this study, Ellen P. Thompson contributed through conceptualization, formal analysis, investigation, and writing. Brian R. Ellis contributed through funding acquisition, supervision, and oversight of review and editing.

Thompson, E.P.; Ellis, B.R. Persistent homology as a heterogeneity metric for predicting pore size change in dissolving carbonates. *Water Resources Research* **2023***, 59*.

Chapter 4 studies the influence of initial pore space geometric complexity on the complexity of the pore space and preferential flowpaths that develop during dissolution. Complexity is quantified using fractal dimension along the length of the flowpath, calculated from XCT data of three limestone cores before and after core flooding experiments with dilute acid. The dominant scales of fractal dimension heterogeneity along the length of the core are studied using spectral analysis. Higher-frequency heterogeneities are found to contribute less to variance after reaction, suggesting that smaller-scale heterogeneities are washed out and larger-scale heterogeneities become more important. This suggests that as dissolution progresses, a larger spatial scale is necessary to fully capture the variability in geometric complexity. The preferential flowpath that formed in each core was isolated and analyzed. Cores with greater pore space complexity were correlated more complex branching behavior of the preferential flowpaths. Optimizing the scales of observations and the expected shape of the preferential flowpaths is necessary to improve predictions of reservoir behavior in natural systems.

Overall, this work improves the estimates of digitally derived rock parameters and studies novel quantitative metrics of pore space heterogeneity and their influence on dissolution behavior. These findings can be used to improve model predictions of subsurface development performance for a variety of applications (geothermal energy production, CCUS, and more) in which understanding the pathways of dissolution is essential.

1.6 References

Adams, B. M., Kuehn, T. H., Bielicki, J. M., Randolph, J. B., & Saar, M. O. (2014). On the importance of the thermosiphon effect in CPG (CO_2 plume geothermal) power systems. *Energy*, *69*, 409–418. https://doi.org/10.1016/j.energy.2014.03.032

Alfonso, I., Beltrán, A., Abatal, M., Castro, I., Fuentes, A., Vázquez, L., & García, A. (2018). Fractal Dimension Determination of Rock Pores by Multi-Scale Analysis of Images Obtained Using OM, SEM and XCT. *Fractals, 26*(05), 1850067. https://doi.org/10.1142/S0218348X18500676

Alhammadi, A. M., AlRatrout, A., Bijeljic, B., & Blunt, M. J. (2018). Pore-scale Imaging and Characterization of Hydrocarbon Reservoir Rock Wettability at Subsurface Conditions Using X-ray Microtomography. *Journal of Visualized Experiments*, (140), 57915. https://doi.org/10.3791/57915

Al-Khulaifi, Y., Lin, Q., Blunt, M. J., & Bijeljic, B. (2017). Reaction Rates in Chemically Heterogeneous Rock: Coupled Impact of Structure and Flow Properties Studied by X-ray Microtomography. *Environmental Science & Technology, 51*(7), 4108–4116. https://doi.org/10.1021/acs.est.6b06224

Baruchel, J., Buffiere, J.-Y., Cloetens, P., Di Michiel, M., Ferrie, E., Ludwig, W., et al. (2006). Advances in synchrotron radiation microtomography. *Scripta Materialia, 55*(1), 41–46. https://doi.org/10.1016/j.scriptamat.2006.02.012

Bazaikin, Y., Gurevich, B., Iglauer, S., Khachkova, T., Kolyukhin, D., Lebedev, M., et al. (2017). Effect of CT image size and resolution on the accuracy of rock property estimates. Journal of Geophysical Research: *Solid Earth, 122*(5), 3635–3647. https://doi.org/10.1002/2016JB013575

Bijeljic, B., Mostaghimi, P., & Blunt, M. J. (2013). Insights into non-Fickian solute transport in carbonates: Insights Into Non-Fickian Solute Transport in Carbonates. *Water Resources Research, 49*(5), 2714–2728. https://doi.org/10.1002/wrcr.20238

Bijeljic, B., Raeini, A., Mostaghimi, P., & Blunt, M. J. (2013). Predictions of non-Fickian solute transport in different classes of porous media using direct simulation on pore-scale images. *Physical Review E, 87*(1), 013011. https://doi.org/10.1103/PhysRevE.87.013011

Carroll, S., Hao, Y., Smith, M., & Sholokhova, Y. (2013). Development of scaling parameters to describe CO2–rock interactions within Weyburn-Midale carbonate flow units. *International Journal of Greenhouse Gas Control, 16*, S185–S193. https://doi.org/10.1016/j.ijggc.2012.12.026

Celia, M. A. (2017). Geological storage of captured carbon dioxide as a large-scale carbon mitigation option. *Water Resources Research*, *53*(5), 3527–3533. https://doi.org/10.1002/2017WR020841

Cnudde, V., & Boone, M. N. (2013). High-resolution X-ray computed tomography in geosciences: A review of the current technology and applications. *Earth-Science Reviews, 123*, 1–17. https://doi.org/10.1016/j.earscirev.2013.04.003

EPA. (2023). *Inventory of U.S. Greenhouse Gas Emissions and Sinks: 1990-2021* (No. EPA 430-R-23-002). Retrieved from https://www.epa.gov/ghgemissions/inventory-us-greenhouse-gas-emissions-and-sinks-1990-2021

Fredd, C. N., & Fogler, H. S. (1999). Optimum Conditions for Wormhole Formation in Carbonate Porous Media: Influence of Transport and Reaction. *SPE Journal, 4*(03), 196–205. https://doi.org/10.2118/56995-PA

Guo, R., Dalton, L. E., Fan, M., McClure, J., Zeng, L., Crandall, D., & Chen, C. (2020). The role of the spatial heterogeneity and correlation length of surface wettability on two-phase flow in a CO2-water-rock system. *Advances in Water Resources, 146*, 103763. https://doi.org/10.1016/j.advwatres.2020.103763

Hommel, J., Coltman, E., & Class, H. (2018). Porosity–Permeability Relations for Evolving Pore Space: A Review with a Focus on (Bio-)geochemically Altered Porous Media. *Transport in Porous Media, 124*(2), 589–629. https://doi.org/10.1007/s11242-018-1086-2

Huang, R., Herring, A. L., & Sheppard, A. (2021). Effect of Saturation and Image Resolution on Representative Elementary Volume and Topological Quantification: An Experimental Study on Bentheimer Sandstone Using Micro-CT. *Transport in Porous Media, 137*(3), 489–518. https://doi.org/10.1007/s11242-021-01571-9

Kang, Q., Zhang, D., & Chen, S. (2003). Simulation of dissolution and precipitation in porous media. *Journal of Geophysical Research: Solid Earth, 108*(B10). https://doi.org/10.1029/2003JB002504

Lai, P., Moulton, K., & Krevor, S. (2015). Pore-scale heterogeneity in the mineral distribution and reactive surface area of porous rocks. *Chemical Geology, 411*, 260–273. https://doi.org/10.1016/j.chemgeo.2015.07.010

Liu, M., & Mostaghimi, P. (2017). Characterisation of reactive transport in pore-scale correlated porous media. *Chemical Engineering Science, 173*, 121–130. https://doi.org/10.1016/j.ces.2017.06.044

Louis, L., Baud, P., & Wong, T.-F. (2007). Characterization of pore-space heterogeneity in sandstone by X-ray computed tomography. *Geological Society, London, Special Publications, 284*(1), 127–146. https://doi.org/10.1144/SP284.9

Luquot, L., & Gouze, P. (2009). Experimental determination of porosity and permeability changes induced by injection of CO2 into carbonate rocks. *Chemical Geology, 265*(1–2), 148–159. https://doi.org/10.1016/j.chemgeo.2009.03.028

Ma, J. (2015). Review of permeability evolution model for fractured porous media. *Journal of Rock Mechanics and Geotechnical Engineering, 7*(3), 351–357. https://doi.org/10.1016/j.jrmge.2014.12.003

Manoorkar, S., Jackson, S. J., & Krevor, S. (2021). Observations of the impacts of millimetre to centimetre scale heterogeneities on relative permeability and trapping in carbonate rocks. *Water Resources Research*. https://doi.org/10.1029/2020WR028597

Menke, H. P., Bijeljic, B., Andrew, M. G., & Blunt, M. J. (2015). Dynamic Three-Dimensional Pore-Scale Imaging of Reaction in a Carbonate at Reservoir Conditions. *Environmental Science & Technology, 49*(7), 4407–4414. https://doi.org/10.1021/es505789f

Menke, H. P., Maes, J., & Geiger, S. (2021). Upscaling the porosity–permeability relationship of a microporous carbonate for Darcy-scale flow with machine learning. *Scientific Reports, 11*(1), 2625. https://doi.org/10.1038/s41598-021-82029-2

Mostaghimi, P., Blunt, M. J., & Bijeljic, B. (2013). Computations of Absolute Permeability on Micro-CT Images. *Mathematical Geosciences, 45*(1), 103–125. https://doi.org/10.1007/s11004-012-9431-4

Mostaghimi, P., Liu, M., & Arns, C. H. (2016). Numerical Simulation of Reactive Transport on Micro-CT Images. *Mathematical Geosciences, 48*(8), 963–983. https://doi.org/10.1007/s11004-016-9640-3

Nakashima, Y., & Kamiya, S. (2007). Mathematica Programs for the Analysis of Three-Dimensional Pore Connectivity and Anisotropic Tortuosity of Porous Rocks using X-ray Computed Tomography Image Data. *Journal of Nuclear Science and Technology, 44*(9), 1233–1247. https://doi.org/10.1080/18811248.2007.9711367

Navarre-Sitchler, A., & Jung, H. (2017). Complex Coupling of Fluid Transport and Geochemical Reaction Rates: Insights from Reactive Transport Models. *Procedia Earth and Planetary Science, 17*, 5–8. https://doi.org/10.1016/j.proeps.2016.12.004

Qajar, J., & Arns, C. H. (2022). Chemically Induced Evolution of Morphological and Connectivity Characteristics of Pore Space of Complex Carbonate Rock via Digital Core Analysis. *Water Resources Research, 58*(3). https://doi.org/10.1029/2021WR031298

Qi, N., Chen, G., Fang, M., Li, B., Liang, C., Ren, X., & Zhang, K. (2018). Damköhler number-based research on dividing dissolution patterns in carbonate acidizing. *Journal of Petroleum Science and Engineering, 170*, 922–931. https://doi.org/10.1016/j.petrol.2018.06.070

Qin, F., & Beckingham, L. E. (2019). Impact of image resolution on quantification of mineral abundances and accessible surface areas. *Chemical Geology, 523*, 31–41. https://doi.org/10.1016/j.chemgeo.2019.06.004

Randolph, J. B., & Saar, M. O. (2011). Combining geothermal energy capture with geologic carbon dioxide sequestration. *Geophysical Research Letters*, *38*(10). https://doi.org/10.1029/2011GL047265

Ruspini, L. C., Øren, P. E., Berg, S., Masalmeh, S., Bultreys, T., Taberner, C., et al. (2021). Multiscale Digital Rock Analysis for Complex Rocks. *Transport in Porous Media, 139*(2), 301–325. https://doi.org/10.1007/s11242-021-01667-2

Seigneur, N., Mayer, K. U., & Steefel, C. I. (2019). Reactive Transport in Evolving Porous Media. *Reviews in Mineralogy and Geochemistry, 85*(1), 197–238. https://doi.org/10.2138/rmg.2019.85.7

Sell, K., Saenger, E. H., Falenty, A., Chaouachi, M., Haberthür, D., Enzmann, F., et al. (2016). On the path to the digital rock physics of gas hydrate-bearing sediments –processing of in situ synchrotron-tomography data. *Solid Earth, 7*(4), 1243–1258. https://doi.org/10.5194/se-7-1243-2016

Wildenschild, D., & Sheppard, A. P. (2013). X-ray imaging and analysis techniques for quantifying pore-scale structure and processes in subsurface porous medium systems. *Advances in Water Resources, 51*, 217–246. https://doi.org/10.1016/j.advwatres.2012.07.018

Wu, Y., Tahmasebi, P., Lin, C., Zahid, M. A., Dong, C., Golab, A. N., & Ren, L. (2019). A comprehensive study on geometric, topological and fractal characterizations of pore systems in low-permeability reservoirs based on SEM, MICP, NMR, and X-ray CT experiments. *Marine and Petroleum Geology, 103*, 12–28. https://doi.org/10.1016/j.marpetgeo.2019.02.003

Xia, Y., Cai, J., Perfect, E., Wei, W., Zhang, Q., & Meng, Q. (2019). Fractal dimension, lacunarity and succolarity analyses on CT images of reservoir rocks for permeability prediction. *Journal of Hydrology, 579*, 124198. https://doi.org/10.1016/j.jhydrol.2019.124198

Zhang, Y., Jiang, F., & Tsuji, T. (2022). Influence of pore space heterogeneity on mineral dissolution and permeability evolution investigated using lattice Boltzmann method. *Chemical Engineering Science, 247*, 117048. https://doi.org/10.1016/j.ces.2021.117048

Chapter 2 Reducing User Bias in X-Ray Computed Tomography-Derived Rock Parameters through Image Filtering

*Reprinted from: Thompson, E. P., Tomenchok, K., Olson, T., & Ellis, B. R. (2021). Reducing User Bias in X-ray Computed Tomography-Derived Rock Parameters through Image Filtering. *Transport in Porous Media*, *140*(2), 493–509. https://doi.org/10.1007/s11242-021-01690-3.

2.1 Introduction

Reliable prediction of fluid flow through the subsurface is essential for numerous applications including subsurface energy technologies such as geothermal energy production, enhanced oil recovery, and geologic carbon sequestration. In systems where percolation through porous media dominates transport, core sample porosity is a primary characteristic that is used to predict upscaled reservoir parameters including permeability and flow dynamics, and is a starting point for forecasting changes in formation behavior over time (Hommel et al., 2018; Ma, 2015; Mostaghimi et al., 2013). Consistent, accurate determination of core porosity is therefore an imperative first step in modeling fluid transport in these systems.

X-ray computed tomography (XCT) allows nondestructive 3D imaging of rock material, making it an exceedingly useful tool for visualizing pore structures *in situ*. XCT imagery can provide geometric and topological information about the pore space that is crucial to predicting flow behavior in porous media, like pore throat size and pore connectivity (Bazaikin et al., 2017; Lindquist et al., 2000). The rise in availability of bench-scale XCT instruments has led to great advances in 3D characterization of geomaterials (Wildenschild & Sheppard, 2013). Yet, reliable

segmentation of XCT datasets into pore- and non-pore voxels, or individual mineral species, remains challenging. Traditional thresholding-based approaches to segmentation (e.g., global thresholding, watershed, hysteresis) are sensitive to user bias (Iassonov et al., 2009). Ample research into the efficacy of various segmentation methods suggests that the optimal segmentation technique would minimize user supervision to reduce the influence of user subjectivity (Deng et al., 2016; Iassonov et al., 2009; Leu et al., 2014; Pini & Madonna, 2016). Machine learning has therefore gained popularity as a method for XCT segmentation and analysis.

Trainable Weka Segmentation (TWS) is an open-source machine learning tool developed for Fiji (Schindelin et al., 2012) that leverages multiple image parameters to segment a dataset based on user-defined training classes (Arganda-Carreras et al., 2017). Originally developed for biological sciences research, TWS is also very useful in geoscience applications because it can segment large 3D datasets efficiently and with reduced user oversight. It has been used, for example, for classification of wetting phases in XCT scans of saturated reservoir rock (Alhammadi et al., 2018), as well as for in situ contact angle and fluid-fluid interfacial angle measurements (Garfi et al., 2020). Others have used TWS to determine crystal size distribution from scanning electron microscope (SEM) images of volcanic rock (Lormand et al., 2018, p. 20).

Machine learning reduces subjectivity but does not completely eliminate user bias from the segmentation process; a classified dataset is only as good as its training data. Segmentation of the same core with different input training data can result in variable overall porosity estimates. Prior work suggests that other downstream parameters, including permeability, are even more sensitive than porosity to differences in the initial binary segmentation (Leu et al., 2014). It is

therefore critical to improve the reproducibility of initial segmentation in order to make meaningful predictions of flow and transport through a rock system from XCT sample data.

Image filtering of XCT datasets can reduce the impact of scan artifacts on the segmentation process. Binary classification of the XCT dataset into pore space and non-pore space is complicated by the presence of sub-voxel sized features. This results in partial volume effects: middling grayscale values in voxels that contain both pore and rock material (e.g., at pore boundaries), and interpretation of these poorly defined edges can be highly subjective. Noise from a number of sources (the X-ray source, the detector, the sample holder, etc.) is inherent to XCT image collection (Leu et al., 2014). High noise levels can cause misclassification, particularly if global thresholding is used for segmentation and image contrast is low. Filters attempt to correct for these factors in order to improve image quality and simplify the segmentation process.

Prior works have analyzed the impact of image enhancement protocols on digital rock properties. Müter et al. (2012) found that segmentation using Otsu thresholding was improved by the application of edge-enhancing and noise-reducing filters, especially at high levels of Gaussian blurring. Sell et al. (2016) tested numerous noise reduction and edge detection filters and found that gas hydrate saturation levels calculated from CT imagery were significantly impacted by the image enhancement protocols prior to segmentation by combined watershed and region growing techniques. Shulakova et al. (2013) compared signal-to-noise ratios after application of various noise suppression filters and found than an edge-preserving filter optimized noise reduction while maintaining important feature boundaries.

In this study a dual filter approach was employed to address these CT imaging artifacts, coupling contrast enhancement and noise reduction filters. Prior work suggests that dual filtering

can improve segmentation results in rocks with complex pore networks and feature sizes near voxel resolution, and that applying a noise reduction filter without first applying a contrast enhancement filter leads to erasure of small features (Müter et al., 2012). Here, an unsharp mask was used to enhance contrast at pore-rock boundaries, followed by an edge-preserving bilateral filter to reduce blur and noise (Ushizima et al., 2011). Anisotropic diffusion and median filtering were also considered as noise reduction filter options, but both can suffer instability and inefficiency because they solve partial differential equations iteratively. Bilateral filtering uses range and domain filtering and is therefore a preferred method for large datasets (Tomasi & Manduchi, 1998). In a comparative study using images with a resolution of less than 5 μm, a bilateral filter outperformed a median filter (med3) when Gaussian noise had low variance ($\sigma < 75$), and at three times the speed (Ushizima et al., 2011). Because of the low Gaussian noise variance and large size of the XCT dataset used in this study, a bilateral filter was selected.

Beam hardening is another inherent artifact of bench-scale XCT imaging. Bench-scale XCT instruments use a polychromatic beam of X-rays, and the beam's lower frequencies are preferentially attenuated as it passes through the sample material. The result is a relatively high-frequency, high-energy (hardened) beam. A beam passing through the center of a sample (i.e., a greater amount of material in a cylindrical sample) has hardened by the time it passes through the bulk of the material, reducing the effective attenuation coefficient of the center material compared to that of the edges. Upon reconstruction, this manifests as brightening near the edges of the sample. The segmented dataset then shows artificial radial variation in local porosity. Reconstruction XCT software can reduce beam hardening, but programs often over- or under-correct. Synchrotron XCT instruments, which use a monochromatic beam, do not produce this artifact (Wildenschild & Sheppard, 2013). But because synchrotron facilities are not widely

available, beam hardening correction is important for most XCT users. Khan et al. (2015) developed an algorithm specifically for cylindrical rock cores that fits a 2D quadratic polynomial for removal of beam hardening artifacts in classically filtered back-production reconstructed slices. Their code was adapted for the scans used in this study.

The purpose of this study is to introduce and assess a pre-segmentation image filtering workflow to improve the reproducibility of the TWS output and therefore the confidence in rock behavior predictions based on XCT data. To evaluate the effectiveness of the proposed workflow, XCT scans of three rock core samples were examined. Porosities were computed from the dataset after various filter combinations were applied, and those values were compared to experimental measurements. Further investigation into additional rock parameters -- pore size distribution and permeability -- was performed in a case study of one rock core scan. From the segmented dataset, a computational mesh of the pore space was generated, and flow was simulated using OpenFOAM to estimate permeability ("OpenFOAM," 2019). Digitally derived values were validated using an experimental flow-through permeability test. The results of this study support the hypothesis that the application of these three filters prior to the definition of training sets for TWS results in improved output consistency.

2.2 Methods

2.2.1 Laboratory Methods

This study analyzed three core samples of 5.1 cm length x 2.5 cm diameter, all purchased from Kocurek Industries. The cores included: Indiana Limestone, a carbonate from the Mississippian period; Edwards Limestone, a more heterogeneous carbonate from the Lower Cretaceous; and Upper Devonian Berea Sandstone. Kocurek provided expected mineral characteristics for the samples based on analysis of other cores in their inventory (Table 2.1).

Table 2.1: Expected rock properties provided by sample supplier.

Sample	**Expected porosity (%)**	**Expected permeability (mD)**	**Mineral content**
Indiana Limestone	14-18	16-20	97 % Calcite, 3% Montmorillonite
Edwards Limestone	33-35	65-85	100% Calcite
Berea Sandstone	20-22	370-400	91% Quartz, 9% Kaolinite

An XCT scan of each core was taken in the Computed Tomography in Earth and Environmental Sciences (CTEES) facility at the University of Michigan, using a Nikon XT H 225 ST industrial CT scanner. The voxel resolution of each scan was 28 μm; additional scan parameters are included in Appendix Table A.1. The XCT dataset was reconstructed using Nikon CT Pro 3D software, and the built-in beam hardening correction was applied.

Mercury intrusion porosimetry (MIP) was used to determine porosity and pore size distribution experimentally. MIP was performed on material of the same type and from the same supplier using a Micromeritics AutoPore V in the Biointerfaces Institute at the University of Michigan. Two to three intact cubes of rock material, each roughly 1 cm^3, were inserted into the penetrometer bulb. The total sample mass was 3.102 g, 3.2441 g, and 1.8954 g for Indiana Limestone, Edwards Limestone, and Berea Sandstone, respectively. The porosimeter took measurements at 50 different target pressures ranging from 3400 Pa to $4.2x10^8$ Pa. Volume distribution results were compared to digital results.

Core permeability for the Indiana Limestone sample was determined experimentally using a high-pressure flow-through apparatus. Water maintained a confining pressure of 13.8 MPa around the core at ambient temperature. Deionized water flowed through the core at a constant flow rate of 1 mL/min. Upstream and downstream pressure transducers continuously monitored fluid pressure upstream and downstream of the core. Permeability was calculated based on this pressure differential using Darcy's Law.

2.2.2 Image Preparation, Filtering, and Segmentation

Each CT dataset was first prepared for filtering. All steps of initial image preparation were performed using Fiji, an install of ImageJ bundled with many image processing plugins (Schindelin et al., 2012). The incomplete image slices at the very ends of the cores were cropped out of the dataset, resulting in a 1050-slice TIFF stack with 1000x1000 pixels per slice. The Analyze Particles function generated a silhouette mask of the core for each image slice. When this mask was multiplied by the original dataset and the threshold was adjusted, the background voxels all assumed a grayscale value of 0. This allowed analysis of the core in isolation from background interference.

Following initial image preparation, eight different combinations of filters were applied to the dataset prior to training class definition in order to assess their influence on the variability of segmentation results. The combinations tested are listed in Table 2.2 and are described in more detail below. For each filter combination, eight repetitions of training set definition and TWS classification were performed.

Table 2.2: Image filter combinations applied prior to TWS

Task	Unsharp mask filter (Un)	Bilateral filter (Bil)	Beam hardening correction (BH)	Trainable Weka segmentation
1				X
2	X			X
3	X	X		X
4	X	X	X	X
5			X	X
6		X		X
7		X	X	X
8	X		X	X

Unsharp mask filter: An unsharp mask with a Gaussian blur radius (σ) of 5 pixels and a mask weight of 0.4 was subtracted from the original image in order to enhance feature edges. These values were selected based on the conclusions of Müter et al., (2012), who found that segmentation results were optimal at σ values between 3 and 5, and that the results were not very sensitive to changes in either input parameter.

Bilateral filter: The algorithm described by Ushizima et al. (2011) was used for parameterization of the bilateral filter. This method turns patches of regions of interest (ROI) into parameters for the bilateral filter. Ten to fifteen ROIs of known material were defined, and Fiji was used to calculate the mean and standard deviation of XCT values within each ROI.

These were input into the MATLAB script FindSigmaR (see Appendix A), which outputted a σ_r value for the bilateral filter. Here σ_r represents the range of voxel intensities, which is assumed to be equal to the largest intensity variation within any ROI. The bilateral filter spatial domain parameter, σ_d, was assigned a value of 3 (Ushizima et al., 2011)

Beam hardening correction: A built-in beam hardening correction was applied during reconstruction using Nikon CT Pro 3D, but the output datasets showed beam hardening overcorrection. A MATLAB script (see Appendix A) adapted from Khan et al. (2015) was applied to fit a polynomial function to the XCT dataset and remove beam hardening artifacts. Figure 2.1 demonstrates the improvement: it shows the average XCT value at varying radial distances from the center of the core in one image, before (red triangles) and after (blue circles) this script was applied. Before the script was applied, the image had radially decreasing XCT values: the edge was darker than the center of the core. After the script was applied, the values were more uniform. Linear regressions were fit to the datasets of each to illustrate the differences in slope.

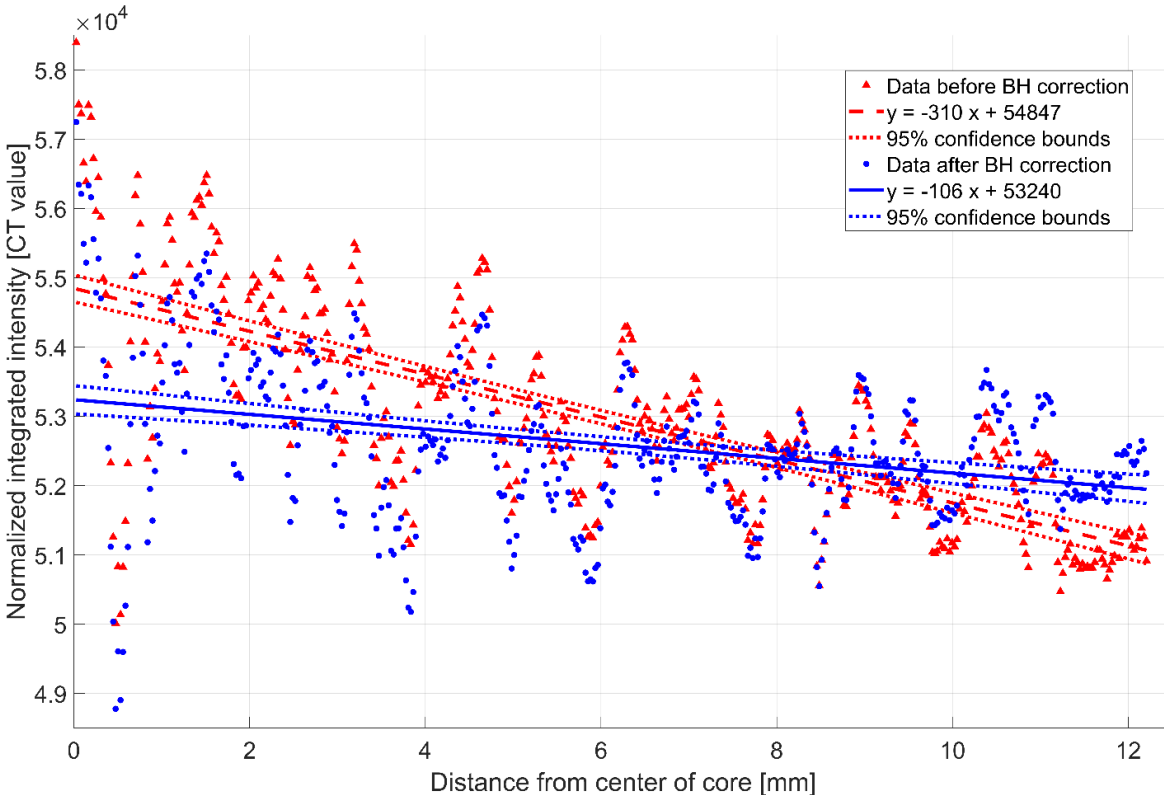

Figure 2.1: Average intensity by radial distance of one XCT image slice, with beam hardening correction done by XCT software (red triangles) and correction done by Khan et al. (2015). MATLAB code (blue circles). Linear regressions and their 95% confidence intervals are shown for each dataset.

A filtering workflow diagram for the fully filtered (Un+Bil+BH) case, and an image showing the effects of these filters, is shown in Figure 2.2. After the beam hardening correction, training sets were defined. Using the freehand selection tool in TWS, a user selected three regions in each of pore and rock space and added them to the training classes. The user did not select the same pixels each time; rather, they identified features (i.e., a single pore, or a single mineral grain) from the dataset on a case-by-case basis in order to allow for user bias in feature selection. The resulting training classes were approximately 100-200 pixels each. An example demonstrating the type of training data selected and associated segmentation results is shown in Figure 2.3 (note that this example is for illustrative purposes only; training data used for the study were selected from different spatial regions across the dataset). These training data were used to classify the full image using TWS.

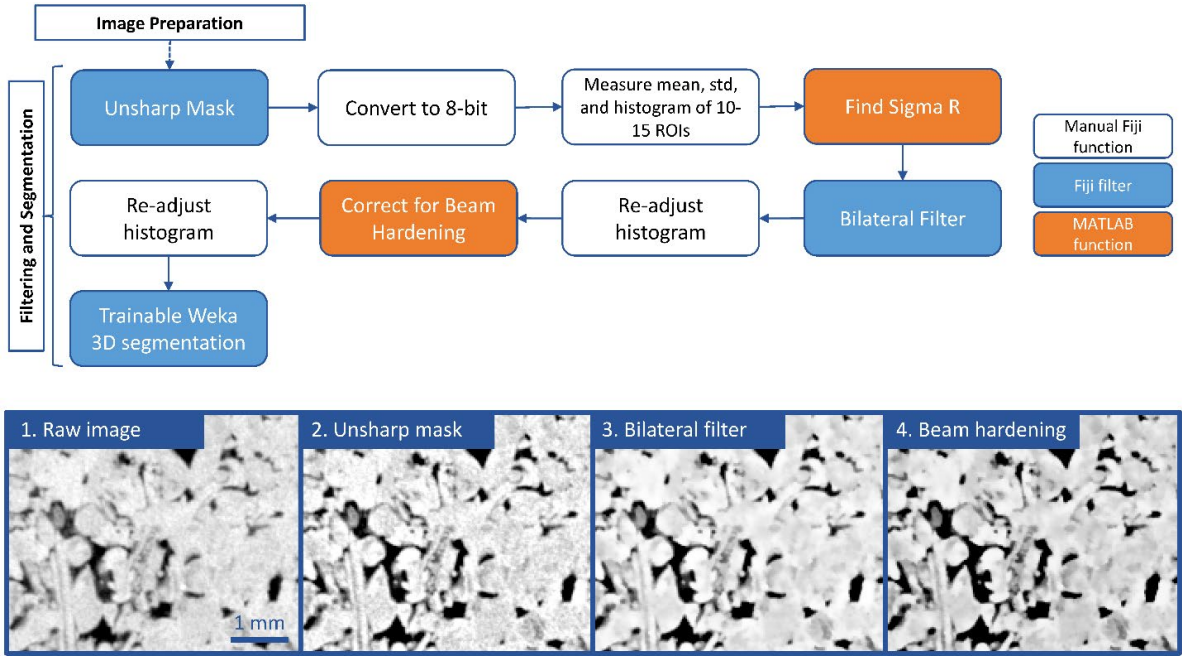

Figure 2.2: Top: Image filtering and segmentation workflow. Completed with manual Fiji functions, Fiji filters, and MATLAB scripts (see Appendix A for code). Bottom: A series of images showing the effects of each filter on a small section of the CT dataset.

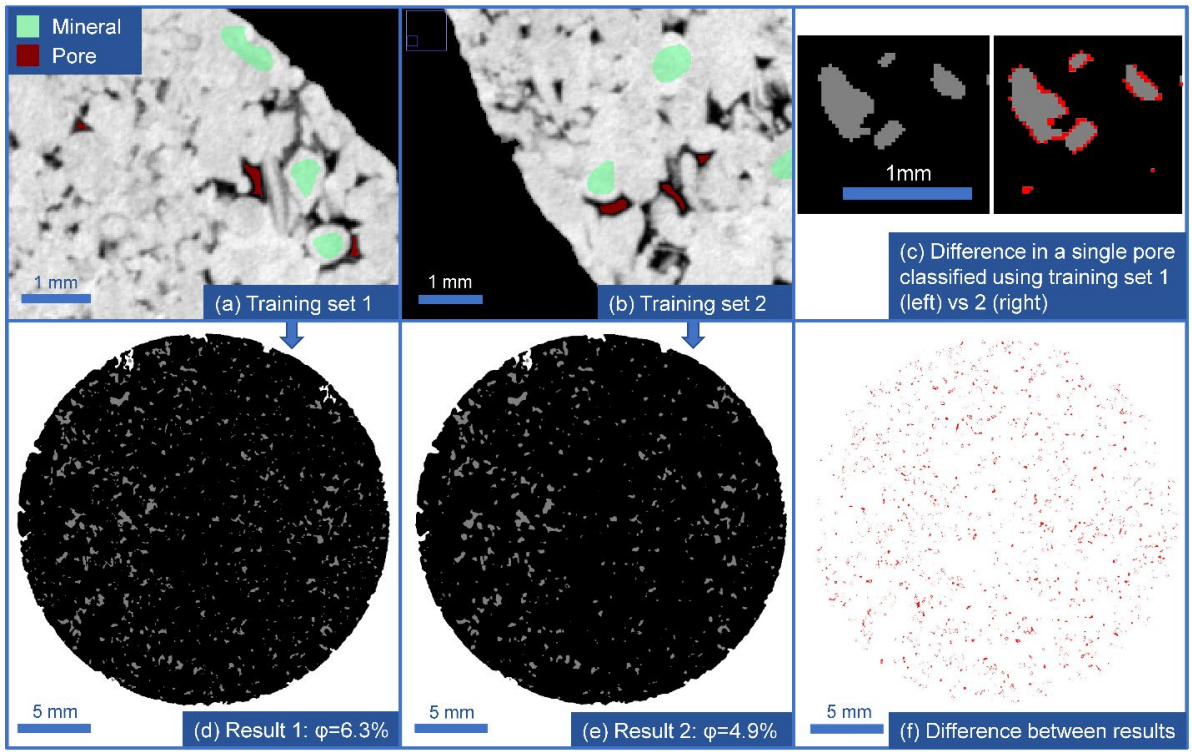

Figure 2.3: An example illustrating different segmentation results ((d) and (e)) based on different sample training sets ((a) and (b)). The red and green regions are regions that the user defined as pore and mineral, respectively. (c) shows the differences at the pore level in pore size and connectivity, and (f) shows the difference in pore pixel assignment of the full image

2.2.3 Indiana Limestone Pore size distribution

Pore volume distributions computed from the segmented Indiana Limestone datasets were compared to experimental results. To digitally quantify the pore volume distribution, the methods described in Münch et al. (2006) were used. The Disconnect Particles plugin was used to disconnect pores at their bottlenecks, with a k value of 0.7. This value, k, is a nondimensional parameter between 0 and 1 that defines the allowable degree of constriction above which pores are defined as distinct. It is a function of the relative radii of the pores and their constriction points, and the value was selected based on visual inspection. To measure the volume and radius of each pore in 3D (assuming spherical pores), the Particle Size Distribution plugin was used (Müter et al., 2012). A substack of the first 200 image slices was used for each iteration to decrease processing time.

2.2.4 Indiana Limestone Permeability simulation

From a subsection of the segmented Indiana Limestone dataset, the BoneJ plugin for Fiji generated a surface file for the solid (Doube et al., 2010). The boxMesh utility for OpenFOAM was used to create a uniform cubic grid cell structure enclosing the surface file domain. The snappyHexMesh mesh generator identified and extracted surface features from the surface file, refined the mesh near those features, and then "snapped" the mesh to the surface file, thus creating a computational mesh of the negative (pore) space for flow simulation. The substack started at the same slice for each iteration, but the length of the substack varied from 50 to 500 slices (1.4 to 14 mm) in order to achieve snappyHexMesh breakthrough at a constant box mesh resolution of one grid cell per voxel. This mesh resolution was limited by computational processing ability. Steady-state, nonreactive flow through the mesh was simulated using simpleFoam ("OpenFOAM," 2019). Boundary conditions were defined to mimic the laboratory

experimental permeability conditions described in Section 2.1. No-slip conditions were applied to the four side walls and to the grain-fluid interface. Pressure at the outlet was held constant at atmospheric pressure, and pressure at the inlet was calculated during flow. Water was flooded through the domain at a rate of 1 mL/min. Steady state inlet pressure was observed, and permeability was determined using Darcy's Law. Figure 2.4 illustrates the model setup.

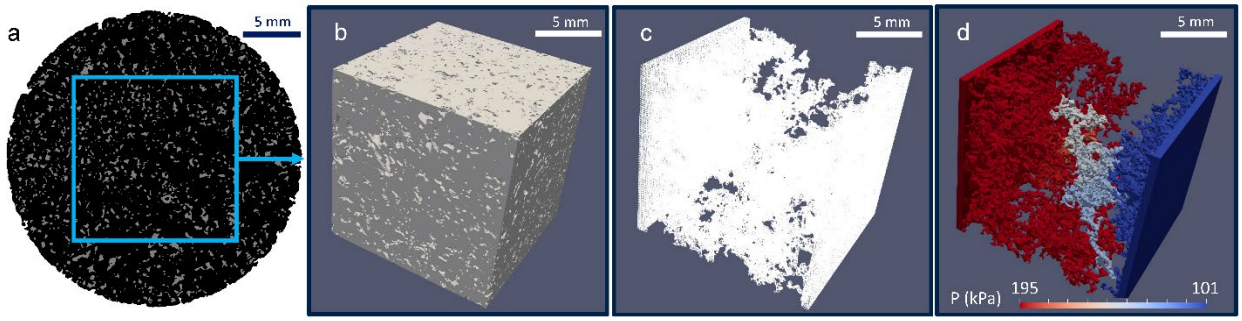

Figure 2.4: OpenFOAM permeability simulation setup. (a) Subsection was taken from binarized segmented dataset. (b) Surface file of rock material was generated. (c) Mesh was generated in OpenFOAM using blockMesh and snappyHexMesh. (d) simpleFoam was run and pressure difference was used to infer permeability.

2.3 Results & Discussion

2.3.1 Overall porosity

Figure 2.5 shows overall porosity results for the segmented datasets, grouped by filter combination. Box plots of the Indiana Limestone, Edwards Limestone, and Berea Sandstone core data are shown in purple, yellow, and dark blue, respectively. The median value is illustrated with a red line, the boxes represent the 25^{th}-75^{th} percentiles, and whiskers show the most extreme values that are not outliers. Outliers are defined here as points that fall more than 1.5 interquartile ranges (IQR) outside the box. Additional data from a higher-resolution scan of Berea Sandstone material (described in more detail below) are shown in light blue. Experimental porosity values from MIP are shown with dashed lines

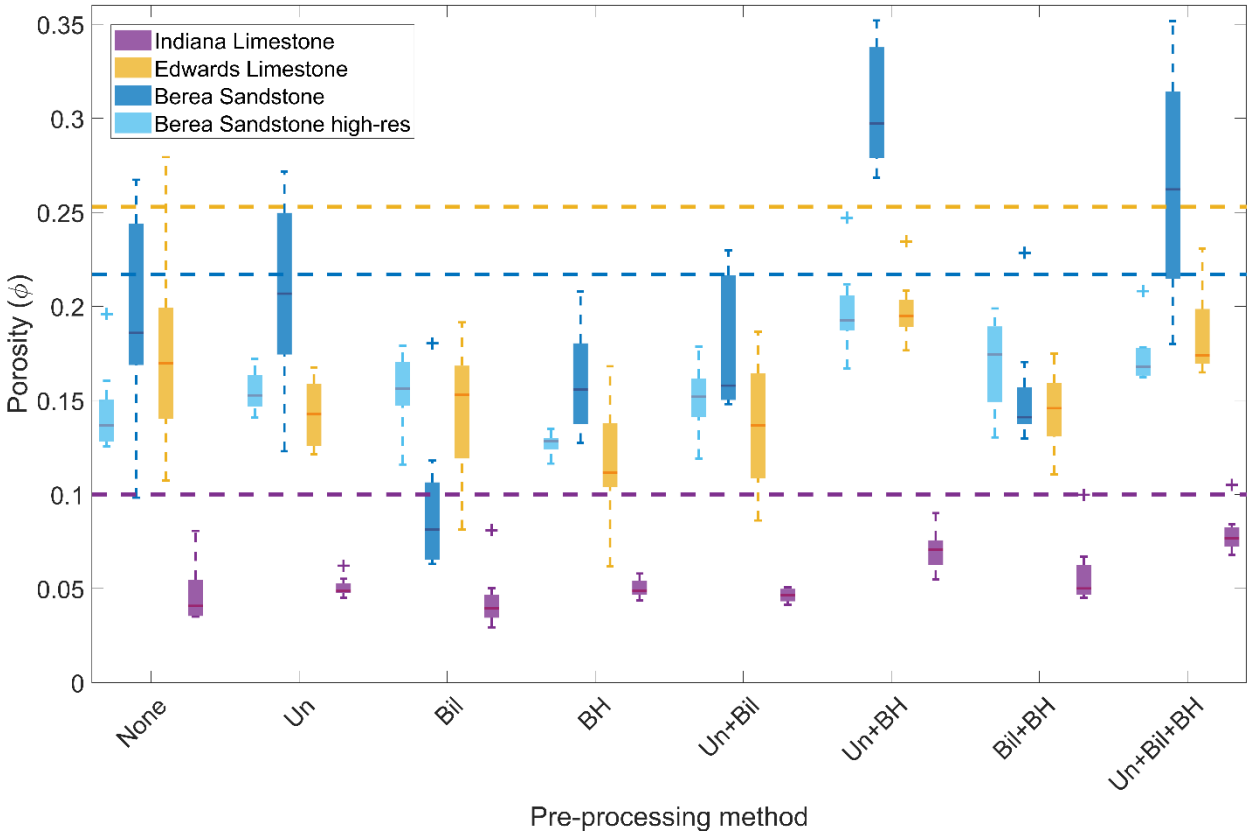

Figure 2.5: Box-and-whisker plots showing porosity values from segmented datasets processed using various filter combinations. The red line shows the median, the boxes contain the 25th-75th percentiles, and outliers fall more than 1.5 IQR outside the boxes. The dashed lines show experimental porosity determined by MIP. Un = unsharp mask, Bil = bilateral filter, and BH = beam hardening correction. n=8 for each filter combination

A few patterns arise that are consistent between the two limestone samples (Indiana Limestone in purple and Edwards Limestone in yellow): the fully filtered (Un + Bil + BH) datasets show higher average porosity and reduced variance compared to the unfiltered (None) case. The cases closest to experimental values are the (Un + BH) and (Un + Bil + BH) cases. The similarity between the (Un + BH) and (Un + Bil + BH) cases, along with the fact that the bilateral filter alone shows little change from the unfiltered dataset data, suggests that the bilateral filter is relatively unimportant for these datasets. The bilateral filter is applied to reduce noise; this suggests that noise in these datasets contributes less to segmentation output variability than poor edge definition and beam hardening artifacts do. These data also suggest that the unsharp mask is particularly important for narrowing the range of values obtained through

segmentation. All values, regardless of filter method, are lower than the experimental value found using MIP. This is most likely due to the presence of sub-voxel porosity in the relatively low-resolution datasets. The digital method is unable to resolve pores smaller than 1 pixel (28 μm, in this study) in radius. If a particular voxel contains, for example, 40% pore space and 60% mineral, it will be classified as mineral. The presence of small pores is therefore consistent with an underestimation of bulk porosity.

Initial analysis of the Berea Sandstone (dark blue) core scan shows quite different results. Variance is not reduced through the use of the three filters. The (Un + BH) and (Un + Bil + BH) cases again give the highest porosity values, but in this case, they are overestimates compared to the experimental data. It is suspected that these inconsistent results are due, at least in part, to the small grain and pore size of this rock material. All three core scans used the same voxel resolution, which was sufficient to identify distinct pore and mineral regions in the limestone samples. The grain size of the sandstone was close to the voxel resolution of the scan, making it more vulnerable to partial volume effects and therefore more challenging to identify training regions that were wholly made up of pore or mineral.

A small (~1 cm^3) rough block of Berea Sandstone material was scanned at higher resolution (8 μm per voxel), and the study was repeated on this scan. The results are shown in light blue and referred to as "high-res scan." This case shows more similar results to the limestone example. The (Un + BH) and (Un + Bil + BH) cases show the closest values to the MIP porosity (shown with a dark blue dashed line), with the (Un + BH) case providing a slightly closer value to the measured porosity. Variance is lower in the (Un + Bil + BH) case than the (None) case. As described above, the beam hardening correction used in this study was specifically written for cylindrical core samples, so it was not being used as designed when

applied to a non-cylindrical sample. It appeared to have similar effect on this rough chunk of material as was seen in the cylindrical limestone samples.

The study of the Berea Sandstone highlights the importance of selecting high enough scan resolution to allow for precise and reliable segmentation of an XCT dataset. The tradeoff between sample size and scan resolution is a physical limitation of the benchtop XCT scanner. The voxel resolution of the core samples analyzed in this study was the highest-possible resolution that allowed for capture of the entire core height. These data may recommend a secondary, higher-resolution scan, as well as experimental methods, to validate segmentation results of a low-resolution scan.

Only three regions in each of pore space and mineral space (six total regions) were used to define the training classes for TWS input, because increased amounts of training data corresponded to prohibitively high processing times. A prior work compared TWS outputs using varying numbers of training regions and found that 10 regions was preferable to 3 for their segmentation of SEM data for crystal size distribution analysis(Lormand et al., 2018). In order to ensure that the limited training dataset size used here did not falsely skew the porosity results, an additional analysis was performed to test varying numbers of training regions. A single filtered dataset of the Indiana Limestone scan (Un + Bil + BH) was used and segmentation was performed using 6, 20, 30, and 40 training regions (divided evenly between pore and mineral regions). This process was repeated three times for each number of regions. Results are shown in Appendix Figure A.1. A pairwise t-test was performed at the $\alpha=0.05$ level to compare the 6-ROI mean porosity to the 20-, 30-, and 40-ROI mean porosities, respectively. Likewise, a pairwise f-test was performed at the $\alpha=0.05$ level to compare variances. No significant differences in mean

or variance were found at this confidence level. These results suggest that the porosity results obtained in this study would not have differed significantly had more training regions been used.

A sensitivity analysis was performed for the Indiana Limestone (Un + Bil + BH) case on the three filter parameters that had been selected based on prior works. This included the bilateral filter spatial radius (BS), the unsharp mask Gaussian blur radius (UR), and the unsharp mask weight (UW). In order to reduce processing time, the analysis was performed on a 100-slice substack from the center of the dataset. This substack length was deemed to be statistically representative of the full dataset: for n=10 100-slice stacks, the coefficient of variation (i.e., the standard deviation normalized by the mean) was less than 10%(Zhang et al., 2000). The base case (BS = 3, UR = 5, UW = 0.4) was compared to test cases with one changed parameter, with eight repetitions each. Results are shown in Figure 2.6.

Pairwise t- and f-tests at the α=0.05 were used to compare mean and variances of the base case against each test case. The bilateral filter spatial radius (red) had no significant difference in mean or variance at this confidence level for any of the tested values. As discussed above, the bilateral filter had little effect on the results from the full core analyses, and this sensitivity analysis suggests that this finding would hold true even after changing the bilateral filter parameters. The unsharp blur radius (blue) had significantly different mean values for the UR = 2 and UR = 3 cases, but at UR $\geq$ 4 no significant difference from the base case was observed. The variance was lower in the UR = 3 case, higher in the UR = 8 case (due to one far outlier), and otherwise not significantly different from the base case. These results suggest that using a blur radius above a minimum value is important, but above that point the value does not make a difference. The largest difference was observed in the unsharp mask weight (green) test cases. Each case had a different mean value from the base case, increasing from the lowest value for the

lowest mask weight to the highest value for the highest mask weight. Variance was consistent across all cases. These data suggest that a mask weight of 0.5 would have been better suited for this particular rock core, as the mean of the UW = 0.5 test case was closest to the experimental porosity of 0.10. This highlights the value of a pre-analysis testing different filter parameters on a representative sub-volume in order to optimize filtering on a case-by-case basis.

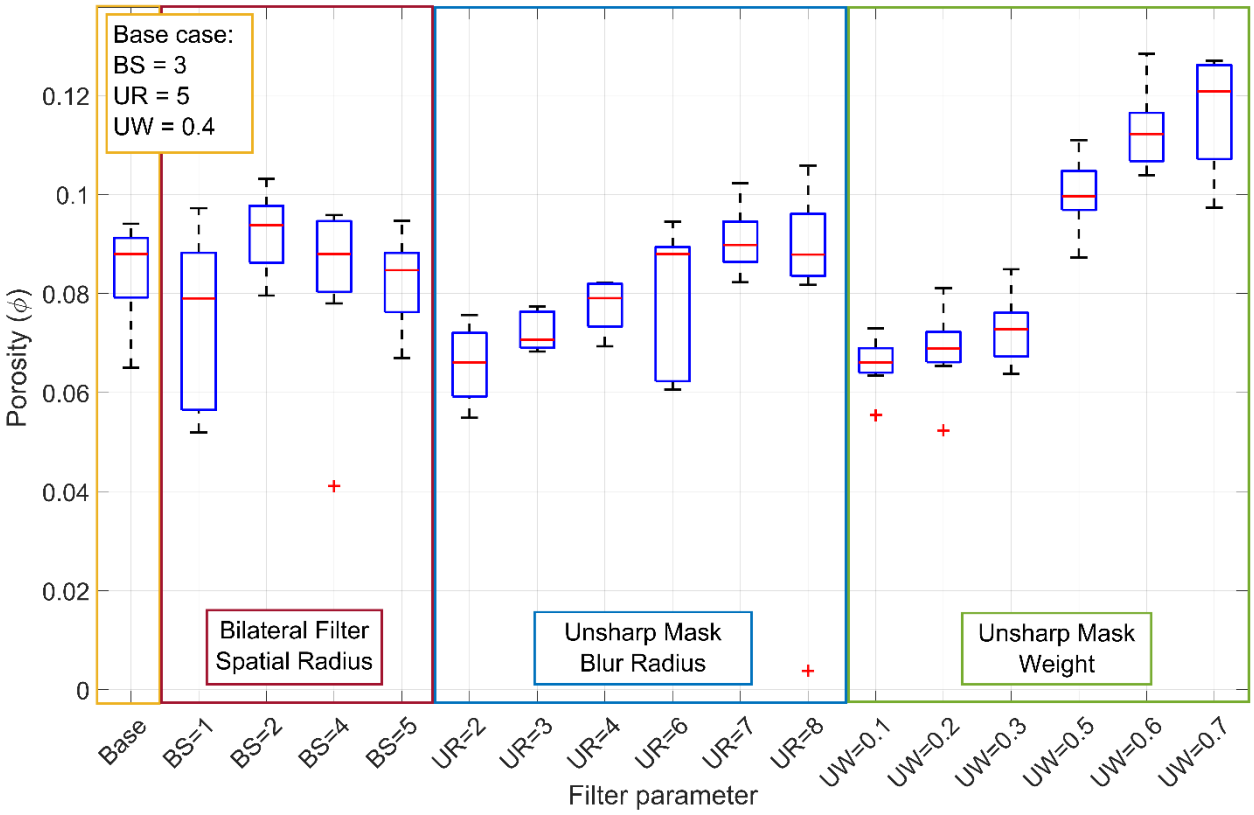

Figure 2.6: Box and whisker plot results of filter parameter sensitivity analysis. A base case (yellow) was compared to cases in which one parameter value was changed: bilateral filter spatial radius (red), unsharp mask blur radius (blue), or unsharp mask weight (green). Red lines show medians, boxes show 25th-75th percentiles, and whiskers show most extreme values that are not outliers. Outliers (red plus signs) are points that fall further than 1.5 IQR outside of the box.

2.3.2 Indiana Limestone Pore Size Distribution

As a case study on the Indiana Limestone core scan, pore volume distributions were generated based on the digitally derived data and experimental MIP data (Figure 2.7). Digital data were binned based on the size thresholds of the porosimeter in order to compare volume

fractions. The distributions calculated from the XCT data show little variance compared to the experimental data. Pores with radii around 50 to 500 µm (roughly 2 to 18 voxels) dominate the pore volume fraction. The full MIP dataset (black dotted line) shows a much wider distribution of sizes, with approximately 23% of the pore volume fraction made up of sub-micron pores. This figure highlights that, as expected, comparison between digital and experimental data is hampered by difference in resolution(Nimmo, 2004). Digital analysis is unable to resolve pores smaller than 1 XCT voxel, whereas MIP can detect pores down to 10s of nm. We see very little difference between the XCT datasets with different filter combinations. Image filtering cannot overcome the loss of resolution from bench-scale XCT imaging. Even when MIP data are truncated to only include those pores that the XCT data could possibly resolve (radius greater than 1 XCT voxel), they still have greater variance because of that difference in resolution.

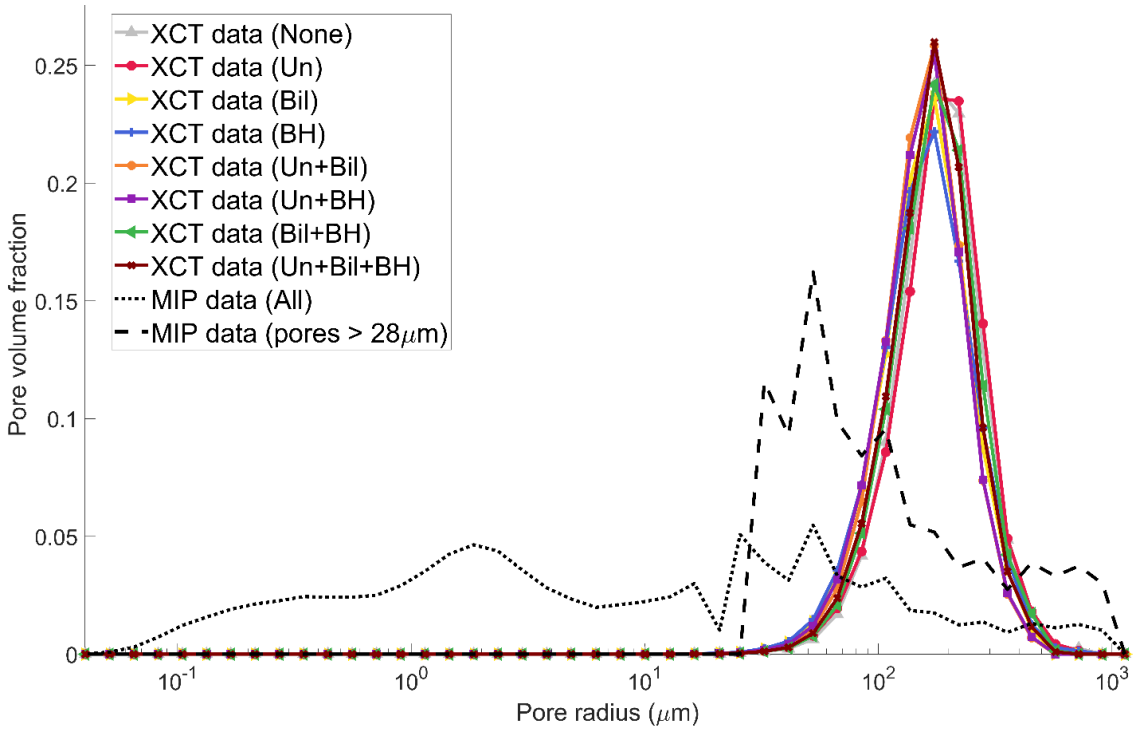

Figure 2.7: Pore volume distribution as a function of pore radius. Digitally derived distributions for each filtered combination are shown in solid lines. Experimental MIP data are shown including all pores (black dotted line) and only pores bigger than the voxel size of the XCT data (black dashed line)

A single-case sensitivity analysis was performed on the impact of the Disconnect Particles parameter, k. The (Un + Bil + BH) datasets were aggregated and analyzed with k values ranging from 0.0 to 1.0 (Figure 2.8). More detailed data from this analysis are provided in Appendix Table A.2.

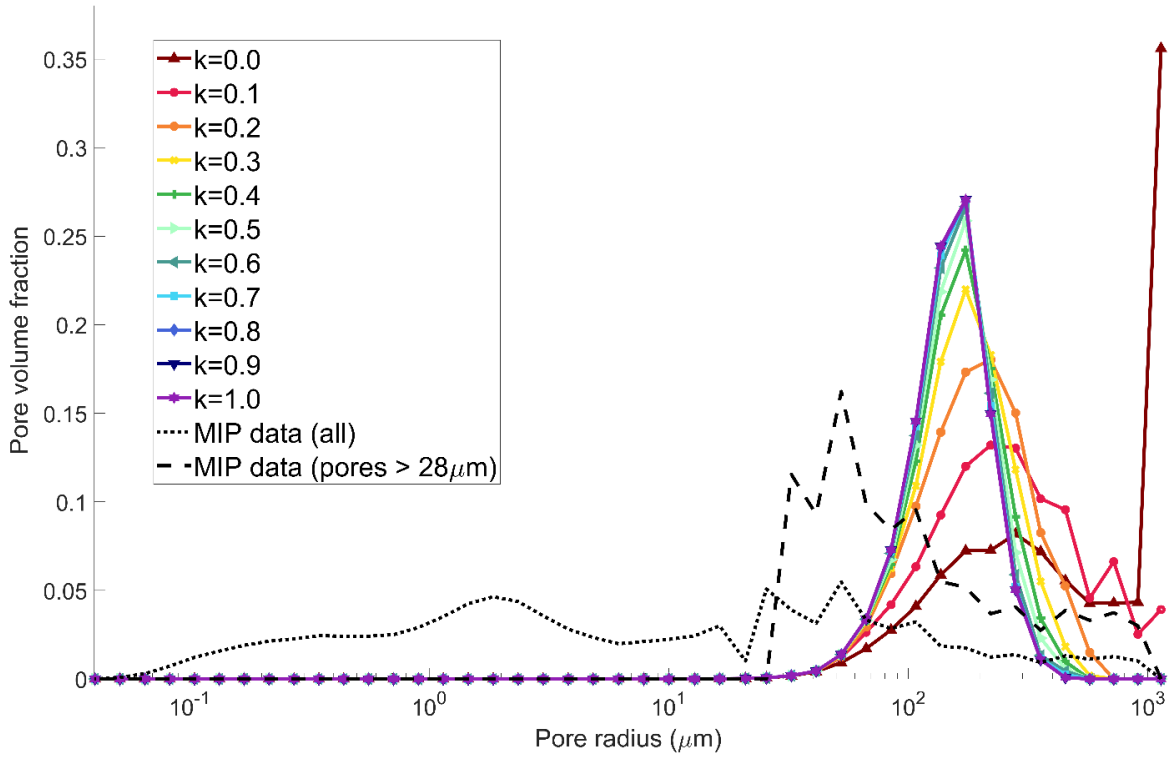

Figure 2.8: Sensitivity case study on Disconnect Particles parameter, k, ranging from k=0.0 in dark red (no disconnection of adjacent pores) to k=1.0 in violet (high disconnection.

The resulting data show that pore size distributions begin to converge at k values above ~0.5. Low k values (i.e., low disconnection) correspond with a poorer approximation of the most abundant pore radii found using MIP but a better representation of the largest pores (>500 µm radius), except for the k=0.0 case (dark red), which severely overestimates the abundance of pores > 1 mm in diameter. These data suggest that k value selection is a trade-off between nearer estimation of the peak values in the experimental pore size distribution curve and improved representation of the distribution of macropores. Either option could be preferable depending on

the use case. The selection of k=0.7 in this study prioritized representation of smaller pores in an effort to represent the pore sizes that dominate the pore volume fraction. No alternative k value selection offers a substantial improvement towards this goal, as this parameter cannot correct for the difference in resolution between experimental data and XCT-derived data.

2.3.3 Indiana Limestone Simulated Permeability

A case study of permeability simulations was performed on the Indiana Limestone core. In order to explore the reproducibility of simulated permeability values from these segmented datasets, the segmented datasets associated with the maximum, median, and minimum porosity were used to generate computational meshes with which to simulate permeability using OpenFOAM. The range of these values is shown in Figure 2.9.

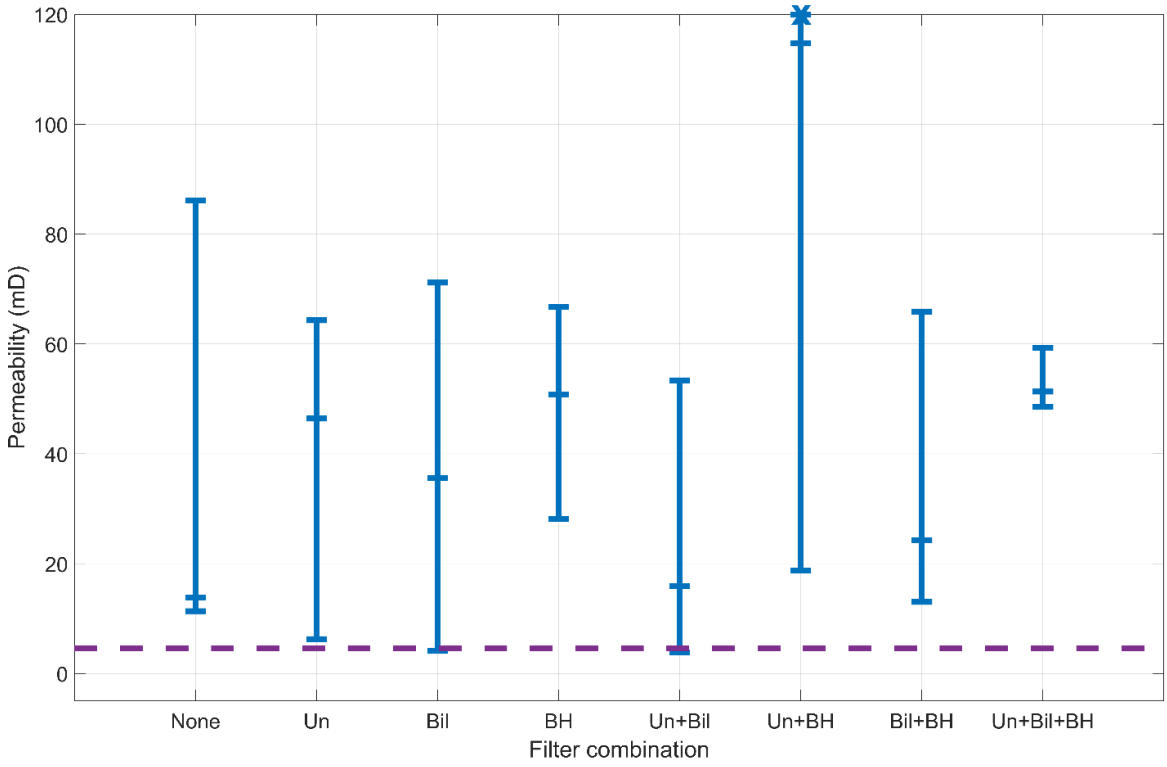

Figure 2.9: Simulated permeability ranges from segmented datasets processed using various filter combinations. The markers indicate permeabilities simulated from the maximum, median, and minimum porosity datasets from each filter combination. The asterisk on the Un+BH range shows an outlier value. The dashed purple line shows experimental permeability. Un = unsharp mask, Bil = bilateral filter, and BH = beam hardening correction.

The dataset with all three filters applied shows the smallest range of simulated permeability values. This is likely due to the small range of porosity values derived from this dataset and illustrates that variation in the initial segmentation process can amplify the differences in simulated downstream processes. Porosity variances were also very small for the Un, BH, and Un + Bil datasets, yet these do not show much reduction in simulated permeability range. This discrepancy may be related to differences in pore connectivity rather than porosity itself, which is a topic for further exploration.

These data suggest that the application of the three filters did improve reproducibility of permeability simulations but did not improve estimation of the permeability value itself. The overestimation of permeability compared to experimental data could be partially attributed to the difference in pore size distribution. The higher fraction of larger pore radii seen in the digital pore size distribution is consistent with an overestimation of permeability. This is further evidence that rock parameter predictions derived from bench-scale CT data are affected by low voxel resolution. We would still expect to see improved reproducibility with a higher resolution scan and may also see an improved permeability value estimate. The overestimation of permeability could also be an illustration of limitations of the OpenFOAM simulation. This method seeks to predict permeability, an upscaled parameter, from a subsection of an already small-scale sample. Heterogeneity within the core (which would be likely in a carbonate due to the presence of fossil fragments) could introduce error to the simulated estimates because a substack was used instead of the whole core length. The mesh resolution and subsection length used here were at the upper limits of the computing capability currently in place. Future work will implement high performance computing resources in order to explore whether increased

subsection size and mesh resolution promote agreement between simulated and experimental results.

2.4 Conclusions

The results of this study support a recommendation to use image filtering prior to the definition of training classes for XCT segmentation by machine learning algorithm. Here, a three-stage workflow was considered for binary segmentation of three core samples: an unsharp mask for contrast enhancement, an edge-preserving bilateral filter for noise reduction, and a beam hardening correction.

In the two limestone samples, the datasets that had all three filters applied had reduced variability in overall porosity and a closer porosity value to the experimental MIP value compared to the unfiltered cases. The XCT data from the sandstone core showed inconclusive results, but segmentation was made difficult due to the scan resolution being close to pore and grain size. A higher-resolution scan of a small sample of the Berea Sandstone showed the same variance reduction and prediction improvement seen in the limestone samples.

Simulated permeability on the Indiana Limestone core also showed an improvement in reproducibility after the application of these three filters. Pore size distribution was studied for the Indiana Limestone core, but the ability to compare these data to experimental results was hampered by differences in resolution between the XCT and MIP analyses. Access to higher-resolution synchrotron XCT instruments is limited for most researchers, and thus there is value in improving the results that can be obtained using the widely available bench-scale XCT.

Improving the reproducibility of XCT segmentation results is essential for many subsurface applications, as this step is critical for the prediction of subsurface fluid behavior. Here, identification of the pore network and its applications for fluid flow were studied in

mineralogically simple rock samples. These methods may also assist in the segmentation of different mineral species, which could identify mineral species accessible to fluid-rock interactions. For any application, increasing XCT segmentation consistency and limiting user bias would improve the confidence in any downstream predictions made using those data, as modeling flow through porous media at the reservoir scale depends strongly on information gathered from rock core samples.

2.5 References

Alhammadi, A. M., AlRatrout, A., Bijeljic, B., & Blunt, M. J. (2018). Pore-scale Imaging and Characterization of Hydrocarbon Reservoir Rock Wettability at Subsurface Conditions Using X-ray Microtomography. *Journal of Visualized Experiments*, (140), 57915. https://doi.org/10.3791/57915

Arganda-Carreras, I., Kaynig, V., Rueden, C., Eliceiri, K. W., Schindelin, J., Cardona, A., & Sebastian Seung, H. (2017). Trainable Weka Segmentation: a machine learning tool for microscopy pixel classification. *Bioinformatics, 33*(15), 2424–2426. https://doi.org/10.1093/bioinformatics/btx180

Bazaikin, Y., Gurevich, B., Iglauer, S., Khachkova, T., Kolyukhin, D., Lebedev, M., et al. (2017). Effect of CT image size and resolution on the accuracy of rock property estimates. *Journal of Geophysical Research: Solid Earth, 122*(5), 3635–3647. https://doi.org/10.1002/2016JB013575

Deng, H., Fitts, J. P., & Peters, C. A. (2016). Quantifying fracture geometry with X-ray tomography: Technique of Iterative Local Thresholding (TILT) for 3D image segmentation. *Computational Geosciences, 20*(1), 231–244. https://doi.org/10.1007/s10596-016-9560-9

Doube, M., Kłosowski, M. M., Arganda-Carreras, I., Cordelières, F. P., Dougherty, R. P., Jackson, J. S., et al. (2010). BoneJ: Free and extensible bone image analysis in ImageJ. Bone, 47(6), 1076–1079. https://doi.org/10.1016/j.bone.2010.08.023Garfi, G., John, C. M., Berg, S., & Krevor, S. (2020). The Sensitivity of Estimates of Multiphase Fluid and Solid Properties of Porous Rocks to Image Processing. *Transport in Porous Media, 131*(3), 985–1005. https://doi.org/10.1007/s11242-019-01374-z

Hommel, J., Coltman, E., & Class, H. (2018). Porosity–Permeability Relations for Evolving Pore Space: A Review with a Focus on (Bio-)geochemically Altered Porous Media. *Transport in Porous Media, 124*(2), 589–629. https://doi.org/10.1007/s11242-018-1086-2

Iassonov, P., Gebrenegus, T., & Tuller, M. (2009). Segmentation of X-ray computed tomography images of porous materials: A crucial step for characterization and quantitative analysis of pore structures. *Water Resources Research, 45*(9). https://doi.org/10.1029/2009WR008087

Khan, F., Enzmann, F., & Kersten, M. (2015). Beam-hardening correction by a surface fitting and phase classification by a least square support vector machine approach for tomography images of geological samples. *Solid Earth Discussions, 7*(4), 3383–3408. https://doi.org/10.5194/sed-7-3383-2015

Leu, L., Berg, S., Enzmann, F., Armstrong, R. T., & Kersten, M. (2014). Fast X-ray Micro-Tomography of Multiphase Flow in Berea Sandstone: A Sensitivity Study on Image Processing. *Transport in Porous Media, 105*(2), 451–469. https://doi.org/10.1007/s11242-014-0378-4

Lindquist, W. B., Venkatarangan, A., Dunsmuir, J., & Wong, T. (2000). Pore and throat size distributions measured from synchrotron X-ray tomographic images of Fontainebleau sandstones. *Journal of Geophysical Research: Solid Earth, 105*(B9), 21509–21527. https://doi.org/10.1029/2000JB900208

Lormand, C., Zellmer, G. F., Németh, K., Kilgour, G., Mead, S., Palmer, A. S., et al. (2018). Weka Trainable Segmentation Plugin in ImageJ: A Semi-Automatic Tool Applied to Crystal Size Distributions of Microlites in Volcanic Rocks. *Microscopy and Microanalysis, 24*(6), 667–675. https://doi.org/10.1017/S1431927618015428

Ma, J. (2015). Review of permeability evolution model for fractured porous media. *Journal of Rock Mechanics and Geotechnical Engineering, 7*(3), 351–357. https://doi.org/10.1016/j.jrmge.2014.12.003

Mostaghimi, P., Blunt, M. J., & Bijeljic, B. (2013). Computations of Absolute Permeability on Micro-CT Images. *Mathematical Geosciences, 45*(1), 103–125. https://doi.org/10.1007/s11004-012-9431-4

Münch, B., Gasser, P., Holzer, L., & Flatt, R. (2006). FIB-Nanotomography of Particulate Systems—Part II: Particle Recognition and Effect of Boundary Truncation. *Journal of the American Ceramic Society, 89*(8), 2586–2595. https://doi.org/10.1111/j.1551-2916.2006.01121.x

Müter, D., Pedersen, S., Sørensen, H. O., Feidenhans'l, R., & Stipp, S. L. S. (2012). Improved segmentation of X-ray tomography data from porous rocks using a dual filtering approach. *Computers & Geosciences, 49*, 131–139. https://doi.org/10.1016/j.cageo.2012.06.024

Nimmo, J. R. (2004). Porosity and Pore Size Distribution. In D. Hillel & J. L. Hatfield (Eds.), *Encyclopedia of Soils in the Environment* (Vol. 3, pp. 295–303). Elsevier.

OpenFOAM. (2019, November 17). (Version v1906). OpenCFD. Retrieved from https://www.openfoam.com/

Pini, R., & Madonna, C. (2016). Moving across scales: a quantitative assessment of X-ray CT to measure the porosity of rocks. *Journal of Porous Materials, 23*(2), 325–338. https://doi.org/10.1007/s10934-015-0085-8

Schindelin, J., Arganda-Carreras, I., Frise, E., Kaynig, V., Longair, M., Pietzsch, T., et al. (2012). Fiji: an open-source platform for biological-image analysis. *Nature Methods, 9*(7), 676–682. https://doi.org/10.1038/nmeth.2019

Sell, K., Saenger, E. H., Falenty, A., Chaouachi, M., Haberthür, D., Enzmann, F., et al. (2016). On the path to the digital rock physics of gas hydrate-bearing sediments –processing of in situ synchrotron-tomography data. *Solid Earth, 7*(4), 1243–1258. https://doi.org/10.5194/se-7-1243-2016

Shulakova, V., Pervukhina, M., Müller, T. M., Lebedev, M., Mayo, S., Schmid, S., et al. (2013). Computational elastic up-scaling of sandstone on the basis of X-ray micro-tomographic images: Computational elastic up-scaling of sandstone. *Geophysical Prospecting, 61*(2), 287–301. https://doi.org/10.1111/j.1365-2478.2012.01082.x

Tomasi, C., & Manduchi, R. (1998). *Bilateral filtering for gray and color images*. In Sixth International Conference on Computer Vision (IEEE Cat. No.98CH36271) (pp. 839–846). Bombay, India: Narosa Publishing House. https://doi.org/10.1109/ICCV.1998.710815

Ushizima, D., Parkinson, D., Nico, P., Ajo-Franklin, J., MacDowell, A., Kocar, B., et al. (2011). *Statistical segmentation and porosity quantification of 3D x-ray microtomography*. In A. G. Tescher (Ed.) (p. 813502). Presented at the SPIE Optical Engineering + Applications, San Diego, California, USA. https://doi.org/10.1117/12.892809

Wildenschild, D., & Sheppard, A. P. (2013). X-ray imaging and analysis techniques for quantifying pore-scale structure and processes in subsurface porous medium systems. *Advances in Water Resources, 51*, 217–246. https://doi.org/10.1016/j.advwatres.2012.07.018

Zhang, D., Zhang, R., Chen, S., & Soll, W. E. (2000). Pore scale study of flow in porous media: Scale dependency, REV, and statistical REV. *Geophysical Research Letters, 27*(8), 1195–1198. https://doi.org/10.1029/1999GL011101

Chapter 3 Persistent Homology as a Heterogeneity Metric for Predicting Pore Size Change in Dissolving Carbonates

*Reprinted from: Thompson, E. P., & Ellis, B. R. (2023). Persistent Homology as a Heterogeneity Metric for Predicting Pore Size Change in Dissolving Carbonates. *Water Resources Research*, *59*(9), e2023WR034559. https://doi.org/10.1029/2023WR034559

3.1 Introduction

Predicting changes in reservoir flow properties due to precipitation and dissolution is essential for numerous subsurface energy technologies, including the safe and reliable implementation of subsurface carbon capture, utilization, and storage (CCUS). Permeability evolution in porous media through mineral dissolution and precipitation has been described using various forms of the Kozeny-Carman relation since its original development in the early 20th century(Carman, 1937; Hommel et al., 2018; Kozeny, 1927). These relationships predict permeability change as a function of porosity change. But relationships determined strictly from porosity can overestimate permeability because they cannot account for tortuosity and pore connectivity(Mostaghimi et al., 2013). Geoscientists have recently looked to topology – a branch of mathematics that studies the spatial relationships and connectedness of geometric features – to address this(Suzuki et al., 2021).

Persistent homology is a tool borrowed from algebraic topology which describes the topological features of a space as a function of spatial resolution. It has recently been applied as a heterogeneity metric in the characterization of geomaterials. The key output of a persistent

homology analysis is a persistence diagram (PD). In classical topology, features in a space are described as simplicial complexes. The features are grown or shrunk incrementally, and the distances at which simplicial complexes of different dimensions appear (birth) and disappear (death) are recorded. These are visualized in a Cartesian coordinate system with birth distance on the x-axis and death distance on the y-axis. The distance from the x=y diagonal represents a feature's *persistence*: the distance between birth and death.

The same principle can be applied to digital imagery; in this case, the filtration process applies to structures of pixels or voxels instead of simplicial complexes. Existing void features are grown or shrunk by incremental numbers of voxels and their birth-death intervals are plotted (Figure 3.1). These void features are referred to as "holes" and identified by their topological dimension. A 0- dimensional hole is a pore body, a 1-dimensional hole is a loop, and a 2-dimensional hole is a grain. The number of features of the *n*th dimension is called the Betti number b_n. Each dimension is plotted on a separate PD_n. Because the connectivity of each type of pore feature is isolated, it is possible to track changes in the quantity and size of each independently.

Topological analysis has proven a useful tool for describing the heterogeneity of a pore space and using it to predict flow behavior. Jiang et al., (2018) described the heterogeneity of rock pore space using PD heterogeneity analysis on a sphere cloud extracted from XCT data using Dong & Blunt's maximal ball method(Dong & Blunt, 2009). They found that PD heterogeneity analysis was consistent with pore velocity distribution analysis. Others have used topological characteristics to predict permeability during single-phase, non-reactive flow. Moon et al., (2019) developed a computationally efficient method for determining statistical representative elementary volume (REV) based on the persistence diagram, and a statistical

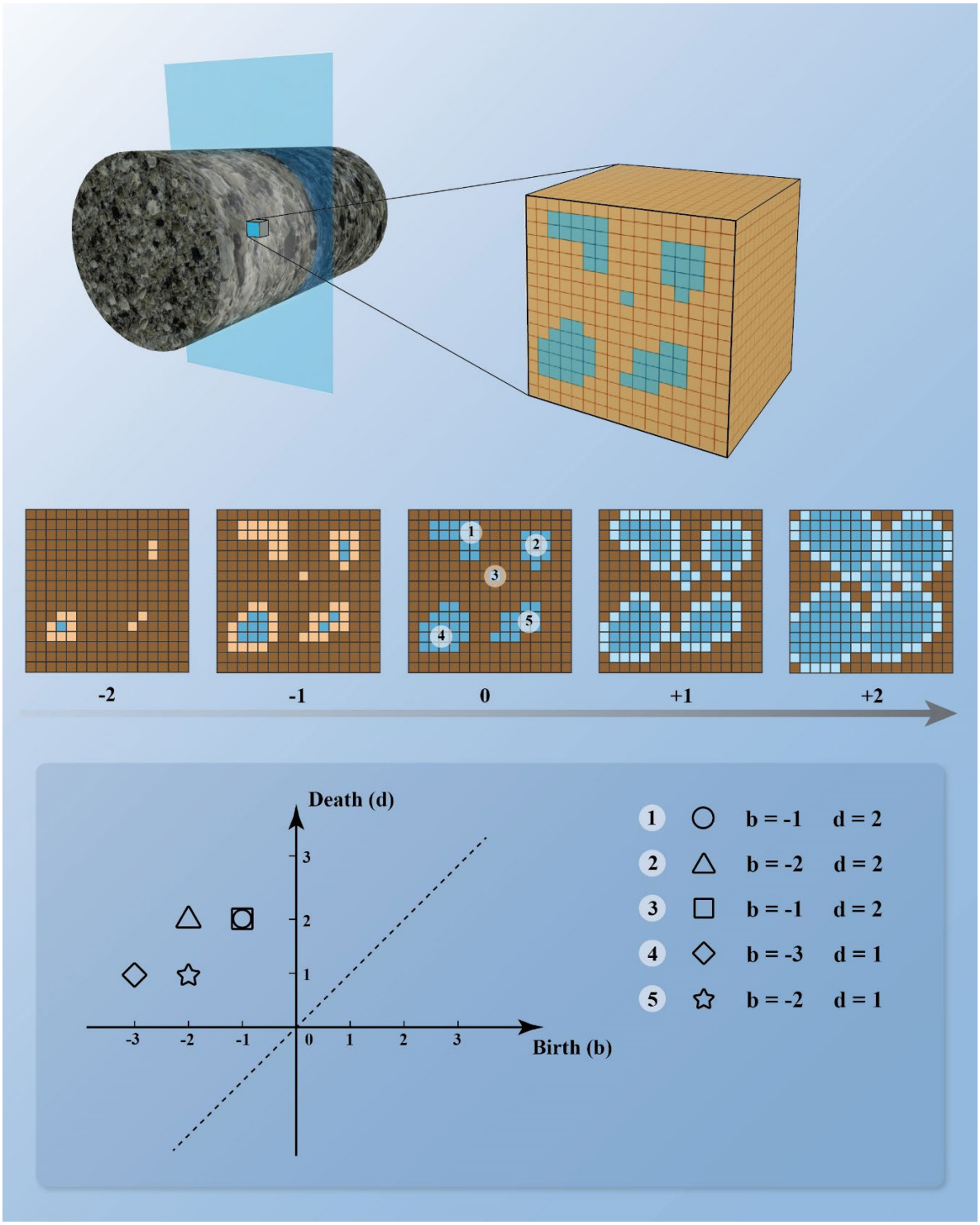

Figure 3.1: Demonstration of the process of converting XCT data into PDs. A XCT dataset is segmented into pore and mineral voxels (here shown in blue and brown, respectively). The diamorse algorithm incrementally shrinks (negative direction) and grows (positive direction) the pore space by one voxel per step and records the distance at which each pore feature closes off (birth) and merges with other pores (death). These points are plotted on a Cartesian plane.

model to predict permeability and tortuosity based on their topological summaries. Suzuki et al., (2021) estimated the number of flow paths and fracture aperture using persistent homology and found excellent agreement between permeability estimated from persistent homology and calculated using direct numerical simulation on artificial fracture networks. Robins et al., (2016) used birth-death diagrams to analyze percolation radii in grain material and found good correlation between critical percolation lengthscales and persistent homology in grain packs and well-sorted sandstones. PD analysis of wetting and nonwetting fluids in a two-phase system has shown good correlation with trapping efficiency in a variety of sandstone systems (Herring et al., 2019).

A few more recent studies have begun to explore the relationship between pore space topology and reactive transport behavior. Lisitsa et al., (2020) introduced persistence analysis as a tool to classify reactive transport behavior in a numerically simulated dissolving carbonate system under different reactive transport scenarios. By using a bottleneck algorithm to cluster simulation scenarios, they successfully separated cases that resulted in homogenous dissolution, wormhole formation, and dissolution front formation. Following on this work, Prokhorov et al. (2022) expanded to 3D numerical simulations using an immersed boundary level set approach for reactive transport modeling. They tested the influence of input parameters (pressure drop, molecular diffusion coefficient, and inlet pH) on changes in pore space topology and studied the influence of topological changes on system permeability and tortuosity, and again found that persistent homology could be used to identify matrix dissolution scenarios.

To date, little work has been done to experimentally benchmark the topological changes predicted in numerical studies. Accurate prediction of pore topology changes under the influence

of chemical change would be extremely useful for predicting the evolution of upscaled reservoir system properties like permeability.

In this study, persistent homology was used to analyze the topological features of three carbonate rocks from XCT scans. We observed the changes in pore network topology that occurred during dissolution, and these topological changes allowed us to infer the driving mechanisms of permeability increase in three limestone carbonates. In all three, permeability increase was primarily due to expansion of already connected, large pores. In the two more homogenous samples, the increase in connected pore size steadily decreased from inlet to outlet, suggesting the growth of connected pores and the emergence of preferential flow paths as the reaction front progresses through the core. In the more heterogeneous sample, the degree of size change was correlated to the initial size of the largest outlier pores. The initial size of the locally large pores showed strong negative correlation with their size change, indicating that the largest pores remain relatively unchanged over the course of dissolution and the core had a net increase in pore size homogeneity. The standard deviation of persistence was found to have a positive correlation with the size change of connected pore bodies when the samples were considered in aggregate, suggesting that increased pore spatial heterogeneity corresponds to a greater degree of channeling. Topological analysis offers a novel metric by which we can measure pore structure heterogeneity and determine its utility for predicting pore space evolution under reactive flow conditions.

3.2 Materials and Methods

This study was performed on three types of limestone with various levels of initial pore network heterogeneity (Indiana Limestone, Edwards Limestone, Lueders Limestone), supplied

by Kocurek Industries. Persistence analysis was performed on XCT scans of sample material after multiple stages of dissolution.

Indiana Limestone is an oolitic limestone from the Mississippian Period, now found in southern Indiana, USA. It has a relatively homogenous composition made up of shells and shell fragments (especially echinoderms and bryozoans) with trace amounts of clays in some areas. Like other Paleozoic tropical limestones, it contained few aragonite sources during initial deposition. Low aragonite content resulted in poor initial cementation, which made it susceptible to mechanical and chemical compaction upon burial, resulting in smaller pore spaces between grains (Dodd & Nelson, 1998).

Edwards Limestone is a porous, permeable limestone from the early Cretaceous, located in south-central Texas, USA. Its beds consist of calcarenites and calcilutites primarily made up of miliolid-fossil biomicrite and oyster-rudist biolithite. Some beds have undergone extensive dolomitization and chertification, though Fourier Transform InfraRed (FTIR) minerology data from Kocurek Industries indicates that the core plug used in this study comes from a section of 100% calcite. Exposure to meteoric water shortly following deposition caused enlargement of some pore spaces, increasing pore size heterogeneity (Abbott, 1975).

The Lueders formation is a member of the Wichita Group in northern Texas, USA. It is a mid-Permian formation consisting of intercalated fluvial and shallow marine material. The limestone beds are dominated by sand-sized fossil fragments and algal pellets (Buczynski & Chafetz, 1987; Varnes et al., 1958). Much of the pore space is moldic, having formed through the preferential dissolution of fossil pieces. This contributes to the overall complexity of the pore network (Morrow & Buckley, 2006).

Pre-reaction pore size distributions were determined experimentally by mercury intrusion porosimetry (MIP) using a Micromeritics AutoPore V in the BioInterfaces Institute at the University of Michigan. Because this analysis technique is destructive, the measurement was performed on small pieces of sample material that were cut from the core plugs prior to imaging and experimentation. Though the portion of the core used for MIP analysis was not included in the topological analysis, it was assumed to be sufficiently representative of the pore size distribution. Two to three roughly cube shaped pieces of intact rock material were inserted into each penetrometer bulb. The total sample masses of each were: 3.6685 g for Indiana Limestone, 2.9820 g for Edwards Limestone, and 4.1258 g for Lueders Limestone. Figure 3.2 shows cumulative pore volume data for these samples. This figure also indicates the XCT resolution used for imaging in the study. The gap in the Lueders data resulted from instrument malfunction that caused it to skip recording those data points. These data indicate that only a small fraction of the total pore volume (approximately 16%, 10%, and 6% for Indiana, Edwards, and Limestone, respectively) consisted of pores with diameters greater than the XCT resolution. Sub-micron resolution would be necessary to fully resolve even 10% of the Lueders pore volume, and a voxel resolution on the order of 100s of nm would be necessary to fully resolve a majority of the pore volume for this sample. Sub-resolution porosity registers as variations in XCT grayscale values depending on the X-ray attenuation of void and mineral space. A binary segmentation algorithm binarizes each voxel into pore versus mineral based on its grayscale value, creating an estimate of true sample porosity. This highlights an inherent limitation of using XCT data to characterize the pore networks of carbonates. Still, XCT scans at 15 µm or coarser resolution have been effective for observing and predicting pore network properties in carbonates in many prior studies (e.g., S. Liu & Huang, 2021; Siddiqui et al., 2006; Sukop et al., 2013; Yoo et al.,

2021). With this known limitation in mind, this study focuses primarily on the largest pores in these samples, which could be characterized with the greatest confidence. In addition, prior works imaged at resolutions below 5µm have highlighted the importance of pores > 60 µm as critical pathways for permeability increase in dissolving carbonates (Qajar & Arns, 2022). While 15 µm resolution cannot possibly resolve all pores within a carbonate, this resolution was selected as a means of observing those macropores important to dissolution while also allowing along-core visualization of flow pathway development.

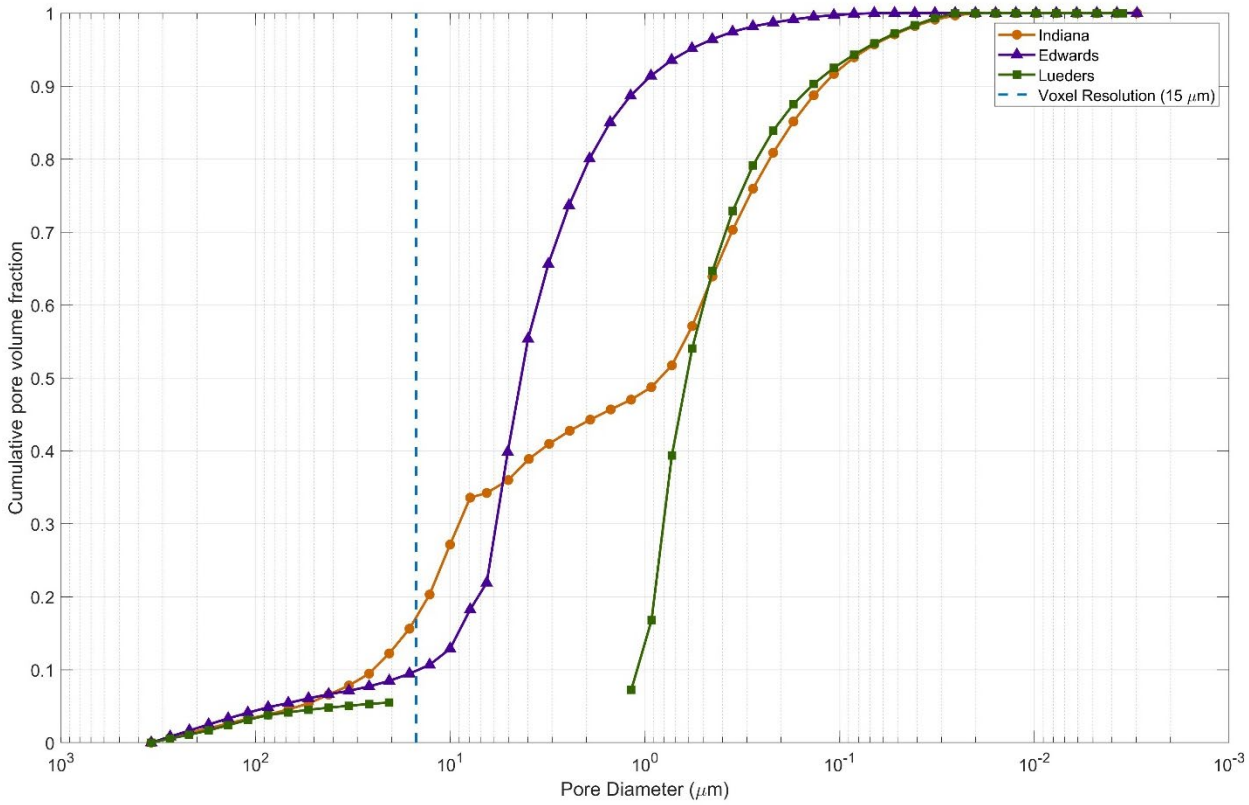

Figure 3.2: Cumulative pore volume fraction data by MIP, with Indiana Limestone shown in orange, Edwards Limestone in purple, and Lueders Limestone in green. A dashed blue line indicates the voxel resolution of the XCT scans used in this study. The gap in Lueders data is due to instrument malfunction.

XCT images were taken in the Computed Tomography in Earth and Environmental Sciences (CTEES) facility at the University of Michigan, using a Nikon XT H 225 ST industrial CT scanner. A full list of scan parameters is included in Appendix Table B.1. The XCT datasets

were reconstructed using Nikon CT Pro 3D software. XCT scans were taken at 15 μm resolution to allow for precise visualization of pores and pore throats. Voxel resolution selection is necessarily a tradeoff between accurate representation of small features and REV size (Peng et al., 2012). Prior work has found that standard topological metrics – Betti numbers and Euler characteristic – can be consistently estimated when sample size is larger than about 15 correlation lengths (Bazaikin et al., 2017). Analysis of the rock cores that were used for this study showed correlation lengths around 50 μm, with correlation length here defined as the distance at which the autocorrelation length of longitudinally averaged porosity falls below a value of 1/e (Elson et al., 1983). A 2.5 cm-diameter sample scanned at 15 μm voxel resolution can therefore be assumed to be sufficiently representative of the sample's pore topology.

Initial and final porosity and permeability values for each sample are shown in Table 3.1. Porosity was determined by the saturation method before and after reaction. Porosity by mercury intrusion porosimetry (MIP) is also provided for a small portion of each sample that was removed prior to reaction and shows reasonable agreement with the saturation method results. Slight variation could be due to slight differences in porosity between the small piece of material used for MIP and the full core plug, or due to differences in precision between MIP and the saturation method. Pre-reaction porosity determined by image analysis is also included, and shows considerable underestimation of the porosity, particularly for the Lueders sample (indicated with a *). As discussed above, this is to be expected for an XCT scan of a low porosity, low permeability rock sample due to the large proportion of sub-resolution porosity. Permeability was determined using Darcy's Law by flowing deionized water through pre-saturated cores at five different flow rates and measuring upstream-downstream pressure differential.

Table 3.1: Porosity and permeability values for each rock core.

Core Sample	Indiana Limestone	Edwards Limestone	Lueders Limestone
Pre-Reaction Porosity (MIP)	0.15	0.24	0.14
Pre-Reaction Porosity (Image Analysis)	0.10	0.21	0.01*
Pre-Reaction Porosity (Saturation Method)	0.17	0.25	0.11
Post-Reaction Porosity (Saturation Method)	0.18	0.27	0.13
Pre-Reaction Permeability (mD)	32	9.8	0.12
Post-Reaction Permeability (mD)	240	170	54

Core samples were reacted with pH 3 HCl to induce calcite dissolution in a high-pressure flowthrough apparatus. Core samples were held by viton sleeves and confining pressure was applied using water to maintain a pressure differential between confining and internal flow pressure of at least 3.4 MPa (500 psi). Upstream and downstream flow was controlled using floating distribution plugs. The inlet plug maintained a constant volumetric flowrate, and the outlet plug was held at atmospheric pressure. Permeability was estimated during reaction by monitoring upstream and downstream pressure using pressure transducers. A transport-limited reactive flow regime was maintained, and advective transport dominated over diffusive transport.

A more detailed description of reactive transport is included in the Results and Discussion section.

Scans were taken prior to reaction and at two time points after reaction. Scans were processed using the filtering process described in Thompson et al. (2021), which in their study yielded more accurate and more consistent porosity values than segmentation of raw image stacks. This filtering process includes an unsharp mask filter for contrast enhancement, a bilateral filter for noise reduction, and a beam hardening correction. Processed scans were segmented using Trainable Weka Segmentation, a machine learning segmentation tool for ImageJ (Arganda-Carreras et al., 2017). Figure 3.3 shows sample image data from the original tomograms, post-processing, and after binary segmentation. Core samples were 2.5 cm in diameter and 4 cm in length. Scans at 15 μm voxel resolution resulted in scan volumes of approximately 2000x2000x2600 voxels. These volumes were cropped to 2000 slices to generate volumes of consistent size that cropped out scanning artifacts near the ends of the cores. Scans were divided into eight 250-slice (3.75 mm) subsections to observe along-core variation. Persistence analysis was performed on the segmented 3D subsections using the diamorse package developed by Vanessa Robins and Olaf Delgado-Friedrichs (Delgado-Friedrichs et al., 2015; V Robins et al., 2011). This Python package first computes the signed Euclidean distance transform from a binary segmented image dataset to identify the Euclidean distance from each voxel to the nearest pore-grain boundary. It then determines persistence birth-death values for each pore based on the distance transform.

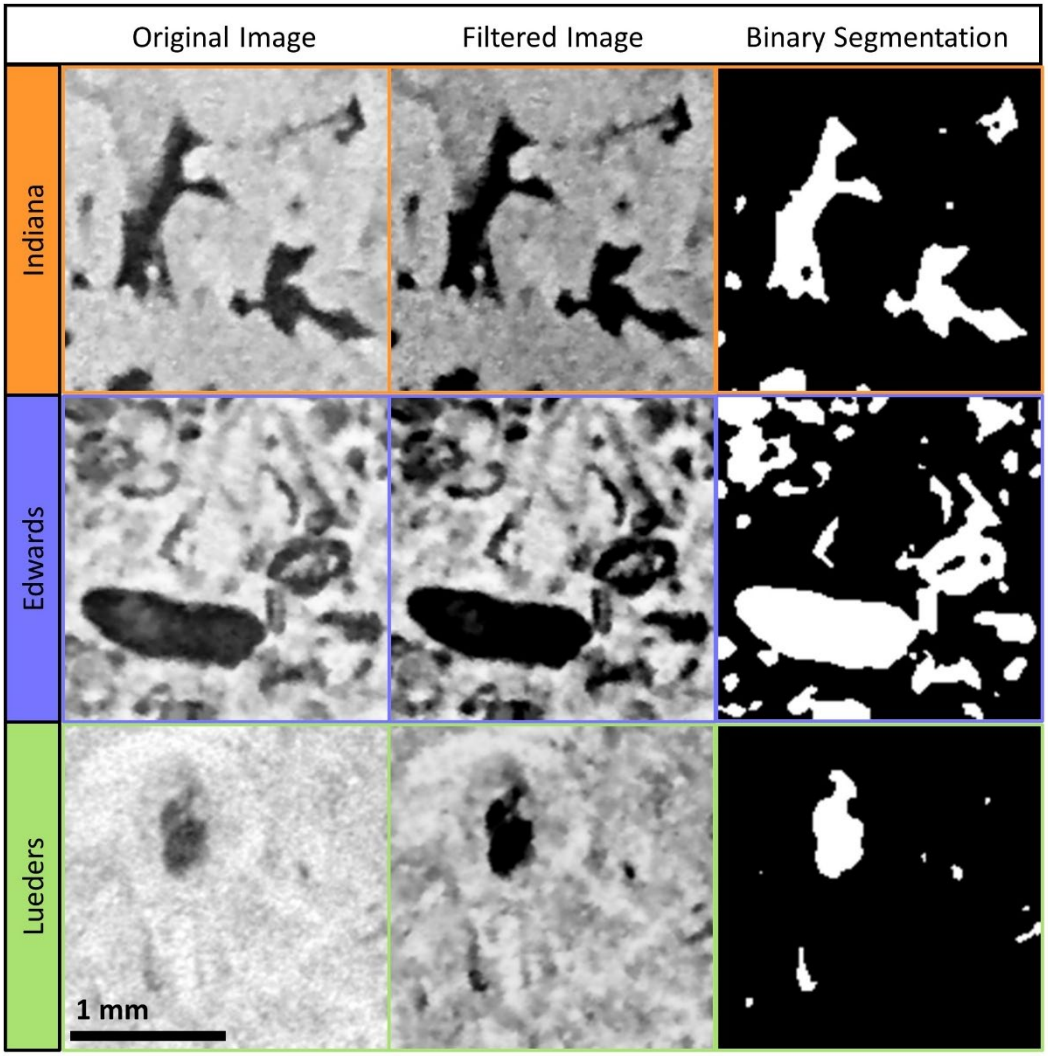

Figure 3.3: Sample XCT data showing the original tomograms (left), filtered images post-processing (center), and after binary segmentation (right).

3.3 Data

Persistence diagram interpretation follows as described in Herring et al., (2019). In a 3D binarized XCT scan in which mineral space is represented by 1s and pore space is represented by 0s, three dimensions of topological features can be observed and interpreted as follows. Examples of each type of feature are illustrated in Figure 3.4.

0^{th} dimension topological features represent pore bodies. Their birth values are negative because they appear as the pore phase shrinks. Their death values are positive if death occurs by

disappearance as the pore phase expands, suggesting that the pore body is isolated from flow channels. These pores (negative birth, positive death) are shown in the second quadrant (Q2) of the PD. A negative death value suggests that a pore death occurs as the pore space shrinks. Thus, 0^{th} dimensional features in the third quadrant (Q3) represent pore bodies within connected pore space. The birth value of a feature in either quadrant represents its size (radius), as computed using the Euclidean distance to the nearest pore boundary. Its persistence represents its degree of isolation from other features of the same dimension. Figure 3.4(b) illustrates a typical 0^{th} dimensional PD.

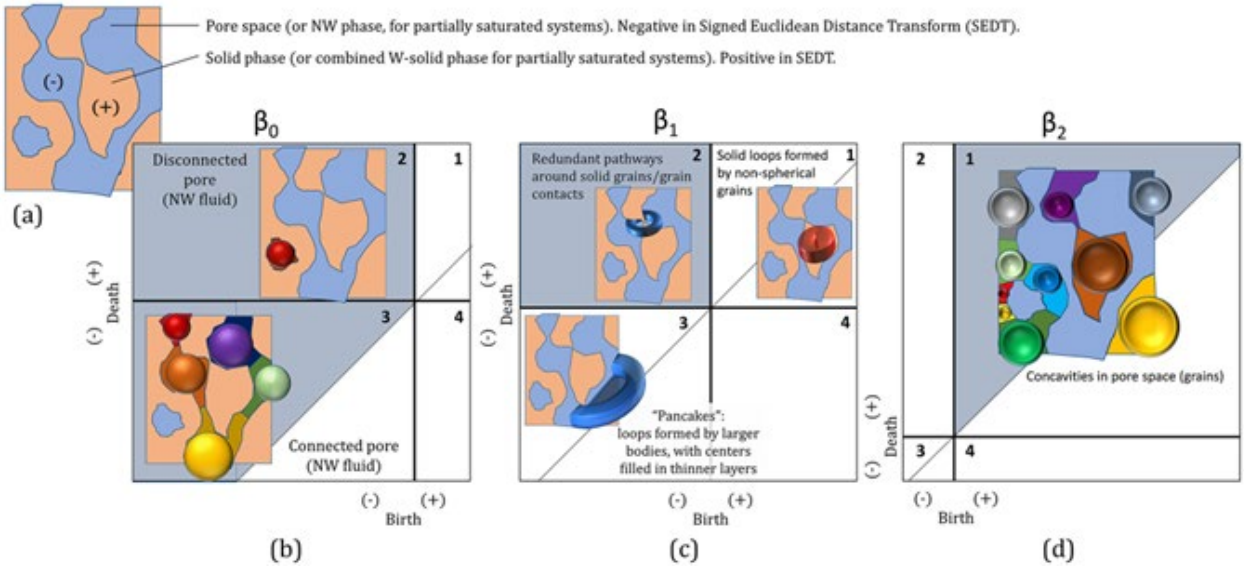

Figure 3.4: Figure reprinted from Herring et al., (2019) serves as a guide for PD interpretation. (a) Shows an example sketch of pore vs mineral space, and (b)-(d) show 0^{th}-2^{nd} dimension example pore geometries, respectively.

1^{st} dimension topological features represent flow channels or loops within the porous media. Features with positive-positive birth-death values (first quadrant, Q1) both appear and disappear as the pore phase expands and therefore represent mineral space with some concavities that allow them to be detected in the 1^{st} dimension. Negative birth values indicate channels that appear as the mineral phase expands. Features in Q2 disappear when they encounter solid phase; these are toroidal loops around grain spaces. The birth values of these points correspond to the

width of the narrowest pore throat in the loop, and the death value represents the diameter of the grain that the pore loop encloses. Those in Q3 disappear when they encounter other pore space, indicating narrower channels within the loop that allow pore bodies to merge. Figure 3.4(c) shows possible features within the 1st dimensional PD space.

The complement to 0th dimensional features, 2nd dimensional features represent convex mineral grains. The points in this PD fall primarily in Q1 and the death value of these points indicates the size of the grains. Figure 3.4(d) shows possible geometries of these features. 2nd dimensional data are available but are not the focus of this study.

3.4 Results and Discussion

Initial analysis focuses on the 0^{th} dimensional PDs of the three rocks described above at the sections closest to the core inlet and outlet (Figure 3.5). In the following diagram, the inlet changes are shown in the top row and outlet changes in the bottom row for each rock sample. PD diagrams show progress of reaction from left to right. Color bars indicate density of datapoints. 0^{th} dimension PDs of both the Indiana and Edwards Limestones show little change over the course of reaction close to the outlet, but substantial expansion into Q3 near the inlet. The increase in number and size of large, negative points indicate more, larger connected pore bodies along the flow channel. The large, negative birth values of these points indicate large pore radii, and the varying death values indicate varying degrees of spatial isolation from other pore spaces. The relatively little change in the Q2 features demonstrates that permeability increase in this case is unlikely to be driven by breakthrough to previously isolated pore bodies, but instead by widening of existing connected pore spaces. Higher change closer to the inlet suggests that preferential flow paths could be forming as the reaction progresses along the length of the core. This suggests that the fast reaction rate caused the fluid to quickly decrease in reactivity as it

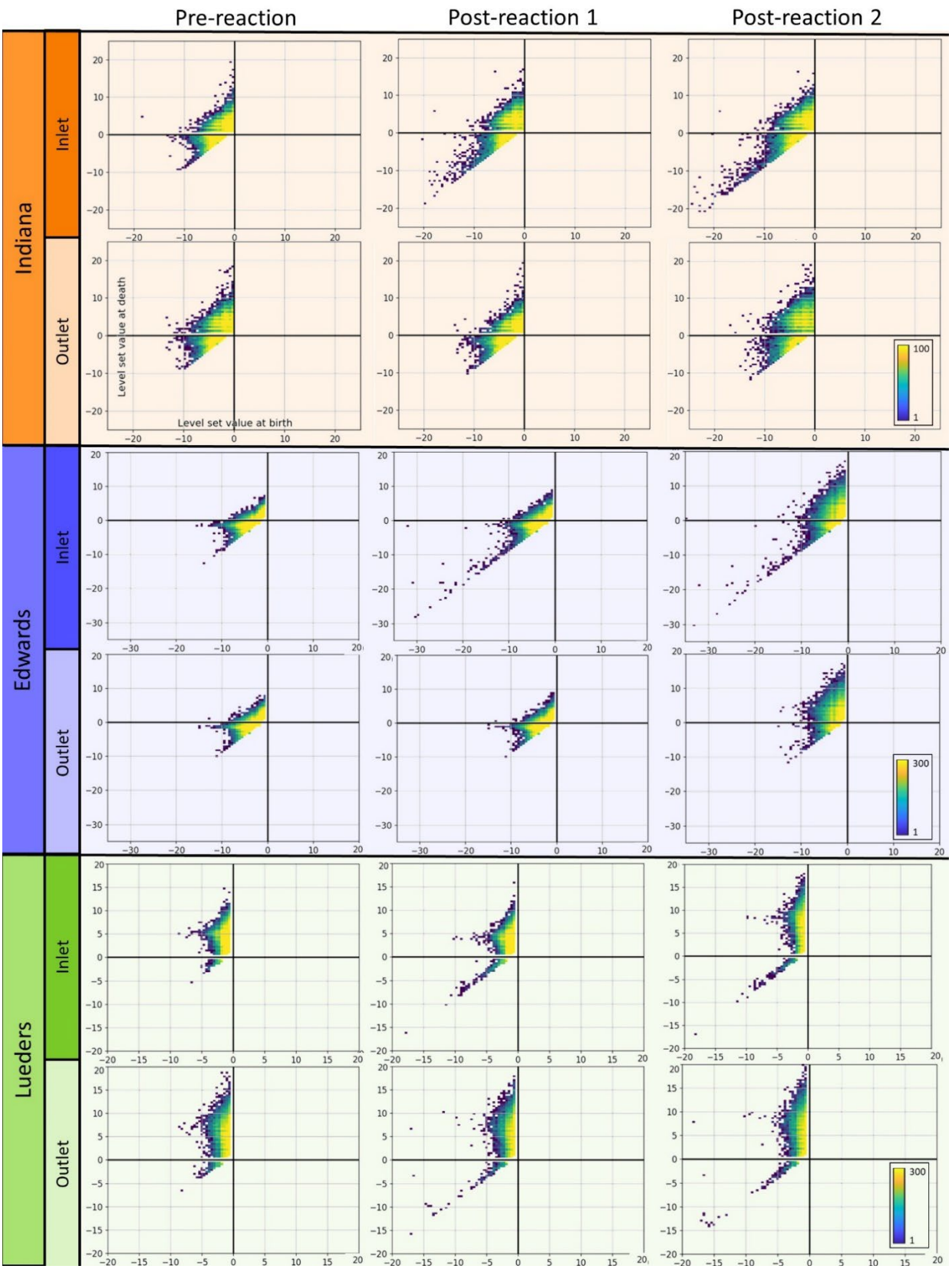

Figure 3.5: 0^{th} dimension PDs from the subsections closes to the inlet and outlet for each rock.

progressed through the rock, resulting in an unstable reaction front that effectively confined dissolution reactions to a few existing channels. A more detailed discussion of reactive transport behavior is included below. Figure 3.6 shows downsampled post-reaction scans with large flow channels highlighted.

The Lueders Limestone 0^{th} dimensional PD also shows expansion into Q3, but to a much lesser extent than Indiana or Edwards Limestone. Where there is expansion, points stay close to the b=d line, indicating low persistence. Unlike both the Indiana and Edwards Limestones, changes were similar at the inlet and outlet; this discrepancy is a topic of further exploration below. The large preferential flowpaths observed near the inlet of each sample are visible in the XCT data; examples are included in Appendix Figure B.1. As seen in Figure 3.6, the Lueders sample contained one very large dominant flow path after reaction.

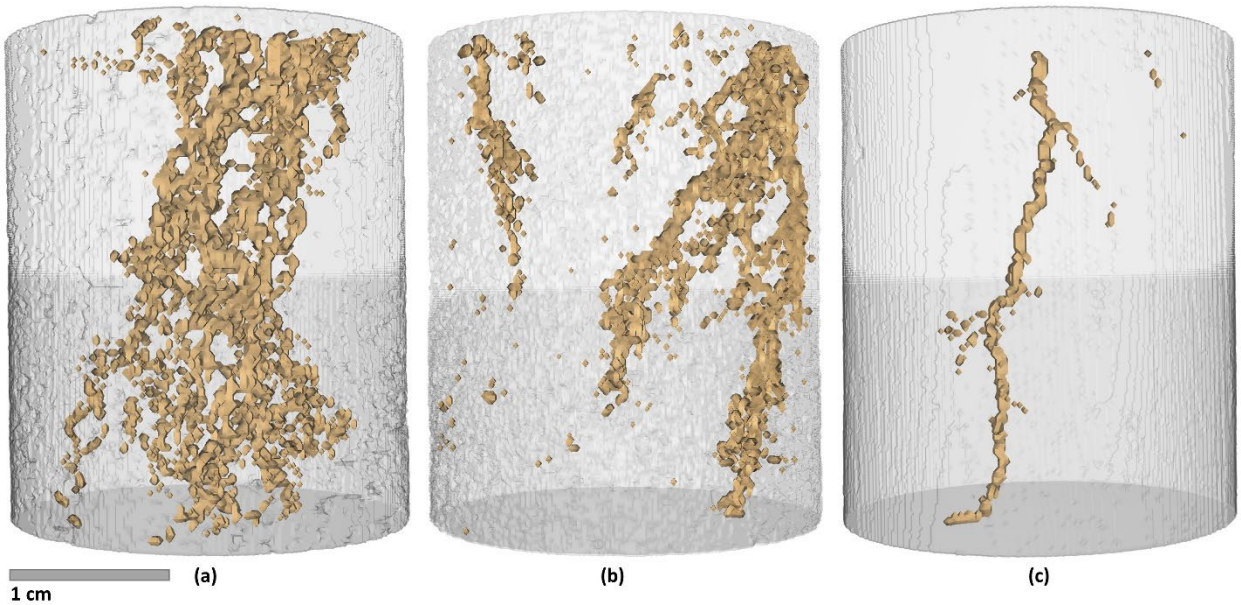

Figure 3.6: Visualizations of large flow channels in post-reaction scans of (a) Indiana Limestone, (b) Edwards Limestone, and (c) Lueders Limestone cores. The inlet is at the top of each image. Images were downsampled to 200x200x200 pixels to highlight the largest flow paths.

Study of the 1st dimension PDs shows relatively little change compared to the 0th dimension PDs (Appendix Figures B.2-B.4). In the Indiana Limestone, the body of the PD cluster remains similar throughout the course of reaction (Appendix Figure B.2). There is some expansion into Q2 and Q3 away from the b=d line indicating some growth of looping pathways within the pore space, particularly close to the inlet. The 1st dimension features of the Edwards Limestone show slightly more change (Appendix Figure B.3). This core experienced spreading in Q2, which indicates an increase in persistence that could be due to narrowing of the inner diameter of loops in the pore space. The most remarkable change is in Q1, where a large increase in both the size and persistence of these 1st dimensional features is observed. This corresponds to a substantial decrease of features in the 2nd dimension and could be due to changes in the geometry of grains that cause them to be captured as 1st dimension instead of 2nd dimension features. Like the Indiana Limestone, the Edwards Limestone saw expansion into more negative values in Q3, especially close to the inlet. This is consistent with the findings of enhanced alteration near the inlet that were seen in the 0th dimension. 1st dimensional data from Lueders show negligible change over the course of reaction (Appendix Figure B.4). This core has very few points in Q2 and Q3, indicating few looping pathways that remain effectively unchanged. There is a slight expansion in the post-reaction 2 scan near the outlet that appears closer to the inlet values, which could indicate an increase in self-similarity of the grain phase along the core as reaction progresses. Overall, the relatively small changes in 1st dimension PDs compared with 0th dimension PDs suggest that permeability change in these experiments was not driven by increase in the size of flow loops within the porous medium.

The prior qualitative discussion identified the 0th dimension, Q3 features (connected pore bodies) as the most notable region of change for all three samples, so this region was isolated for

further study. Quantitative analysis focuses on the size and spatial heterogeneity of the connected pore bodies to determine which characteristics are most important for predicting dissolution behavior. Figure 3.7 shows the size distributions of the 0^{th} dimension, Q3 features before and after two stages of reaction. The means and 25^{th}-75^{th} percentiles change slightly after reaction for the Indiana (orange) and Edwards (purple) samples, and slightly more for the Lueders (green) sample. The most striking difference is in the spread of outliers: these extend to larger values for all three cores, especially near the inlet. This shows that the effect seen in the inlet-outlet PD comparison above is present along the full length of the core, and that the greatest size change occurs in outlier pores that are much larger than the bulk of the pore bodies within each system.

All three cores show growth in outliers, but their changes in size distribution behave differently. The boxplots show that Indiana and Edwards Limestones have similar initial distributions, with the bulk of the pore sizes between 2 and 4 voxels. After reaction, there is a shift in skewness to the right. Lueders has a much tighter initial distribution across the length of the core, but again shows rightward skewness after reaction. This is confirmed by a comparison of skewness of size distribution along the core (Figure 3.8). Indiana and Edwards (orange and purple, respectively) have nearly identical, uniform skewness of size distribution prior to reaction and see similar changes after reaction. This could indicate the size and/or number of outlier pores increases after reaction (see further discussion below). The Lueders core, meanwhile, has a great deal of heterogeneity in its initial skewness. Sections 5 and 7 had very high skewness prior to reaction that remained nearly unchanged after reaction. Other areas increased dramatically in skewness, resulting in an overall smoothing to a uniform, higher skewness post-reaction. This suggests that

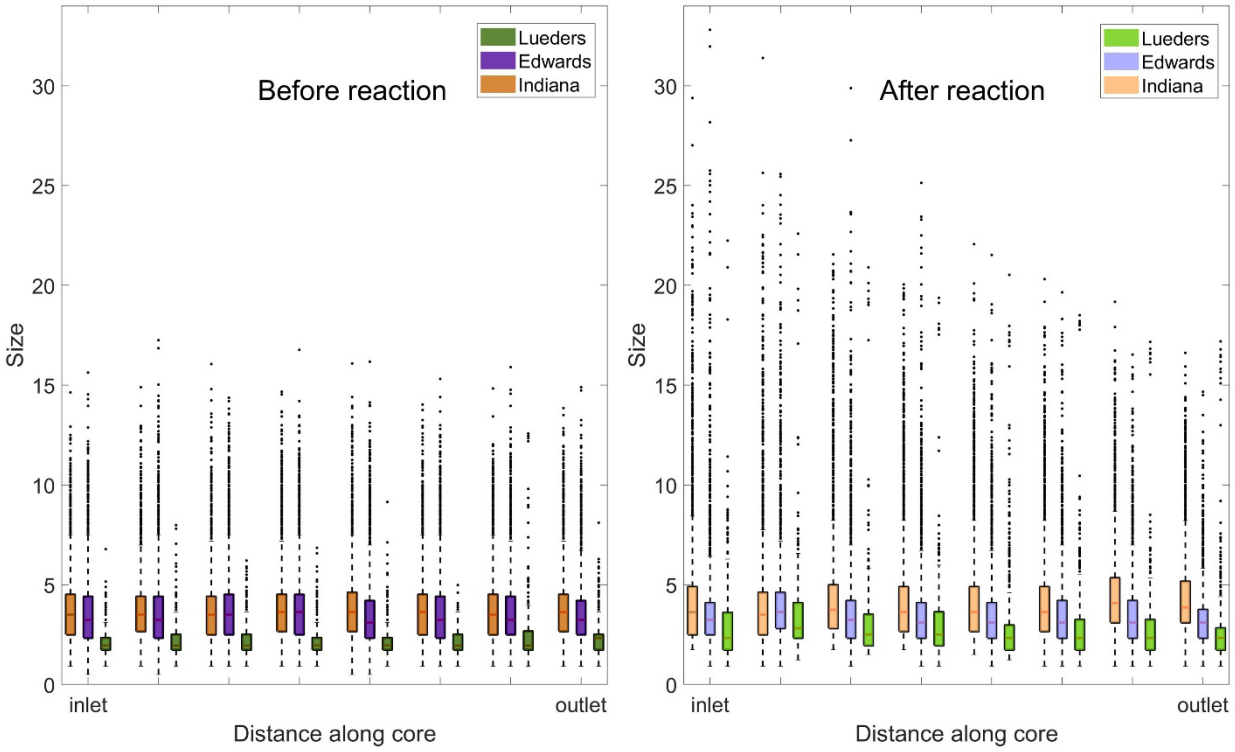

Figure 3.7: Boxplots showing sizes (birth values) of 0^{th} dimension, 3^{rd} quadrant features, the maximally inscribed sphere within connected pore bodies. For each box plot, the red line indicates the median and the boxes represent the 25^{th}-75^{th} percentiles. Outliers are indicated by black dots and indicate points greater than 1.5 interquartile ranges (IQR) beyond the 1^{st} or 3^{rd} quartile. Each dataset has on the order of 10,000 datapoints

the areas of the rock that already had extreme outlier pores saw minor change in the size of those outliers, and areas with fewer, smaller large pores saw the greatest increase. This could be due to the higher surface area-to-volume ratio of the largest pores in the flow path: already large pores have less reactive surface area per volume of reactive fluid passing through, so they experience less change in size over time. This result highlights the importance of analyzing along-core size heterogeneity to predict regions that will experience the greatest change due to dissolution. Locally large pores, if small in comparison to other large pores along the flow path, can experience dramatic growth that may contribute more significantly to net permeability increase.

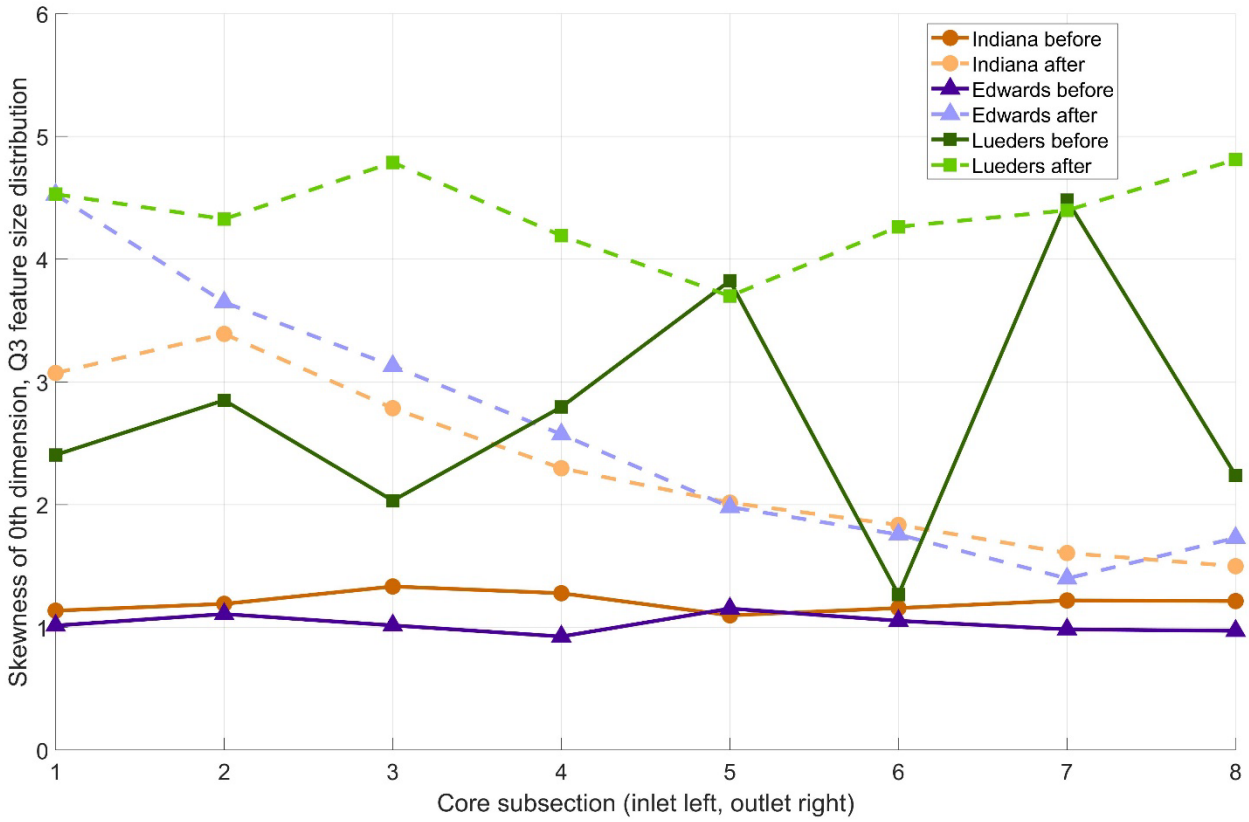

Figure 3.8: Skewness of 0th dimension, Q3 size distributions along the length of each core, before (solid) and after (dashed) reaction.

In discussing skewness of pore size distribution, it is important to note that any pore size distribution generated from XCT data is expected to exhibit some rightward skewness. This is because XCT is a relatively low-resolution imaging method that cannot resolve pores smaller than one voxel, in this case, 15 µm. A common assumption is that features smaller than 2-3 voxels in size cannot reliably be resolved due to partial volume effects. The Lueders limestone in particular had a very low initial permeability (0.12 mD), which suggests that the percolating network of pores and pore throats in the initial media was very unlikely to be resolved fully. Micron- to nanometer- sized pore bodies exist in great numbers in these rocks, as observed in the MIP data above, but they are not expected to be as important for fluid transport. This analysis is limited to the change in the large pores that are expected to dominate flow.

The single largest connected pore body in each subsection (here referred to as a "locally large pore") of each sample was isolated to compare changes depending on initial size and size heterogeneity. Looking at the single largest 0^{th} dimension, Q3 feature for each core subsection, it is again observed that Lueders has a decrease in along-core heterogeneity after reaction (Figure 3.9(a)). Although all the largest pores in each subsection grew to some extent, the along-core size distribution of locally large pores was much smoother than the initial distribution. In contrast, the Edwards and Indiana samples initially had nearly uniform locally large pore sizes and instead showed an increase in size heterogeneity post-reaction (particularly near the inlet). The change in size of each locally large pore was plotted against its initial size and a linear regression was fitted to the data for each sample. (Figure 3.9(b)). In the Indiana and Edwards samples, there was no correlation between initial size and change in size, suggesting that the distance along the core was a stronger driver of pore size increase. However, in the Lueders sample, which initially had a great deal of along-core pore size heterogeneity, the normalized locally large pore size increase was strongly correlated with its initial size ($R^2 = 0.90$). In this sample, this correlation is consistent with the hypothesis that the largest of the large pores do not increase in size as dramatically because they have less reactive surface area per volume of fluid. It also highlights the importance of locally large pores that are relatively small compared to other regions in the flowpath as specific locations that are likely to experience substantial growth under dissolution.

In addition to initial pore size and size distribution, persistence itself provides a metric of pore space heterogeneity that shows some utility in predicting pore size evolution. Figure 3.10 shows the change in mean connected pore body size (0^{th} dimension Q3 size) in each subsection as a function of the initial standard deviation of 0^{th} dimension feature persistence (including both isolated and connected pore bodies). A linear regression fitted to the aggregated data shows

moderate positive correlation ($R^2 = 0.49$, shown here in blue). This is consistent with our understanding of porosity-permeability progression in a rock with an unstable reaction front (Szymczak & Ladd, 2011). Persistence is a proxy for the degree of spatial isolation of a pore body. A system with more isolated pore bodies is more likely to experience flow confined to an existing preferential flow path and is less likely to merge with previously disconnected pores, so as dissolution occurs it expands the existing connected pore bodies. Interestingly, when the rock samples are considered independently, the correlation that was observed in aggregate does not apply. Nor are the size changes aligned with the degree of permeability change observed in each sample (Lueders experienced the greatest increase in permeability, followed by Edwards, followed by Indiana). Analyzing the degree of pore persistence heterogeneity (as measured by standard deviation of 0^{th} dimension persistence) may provide a useful tool for predicting size

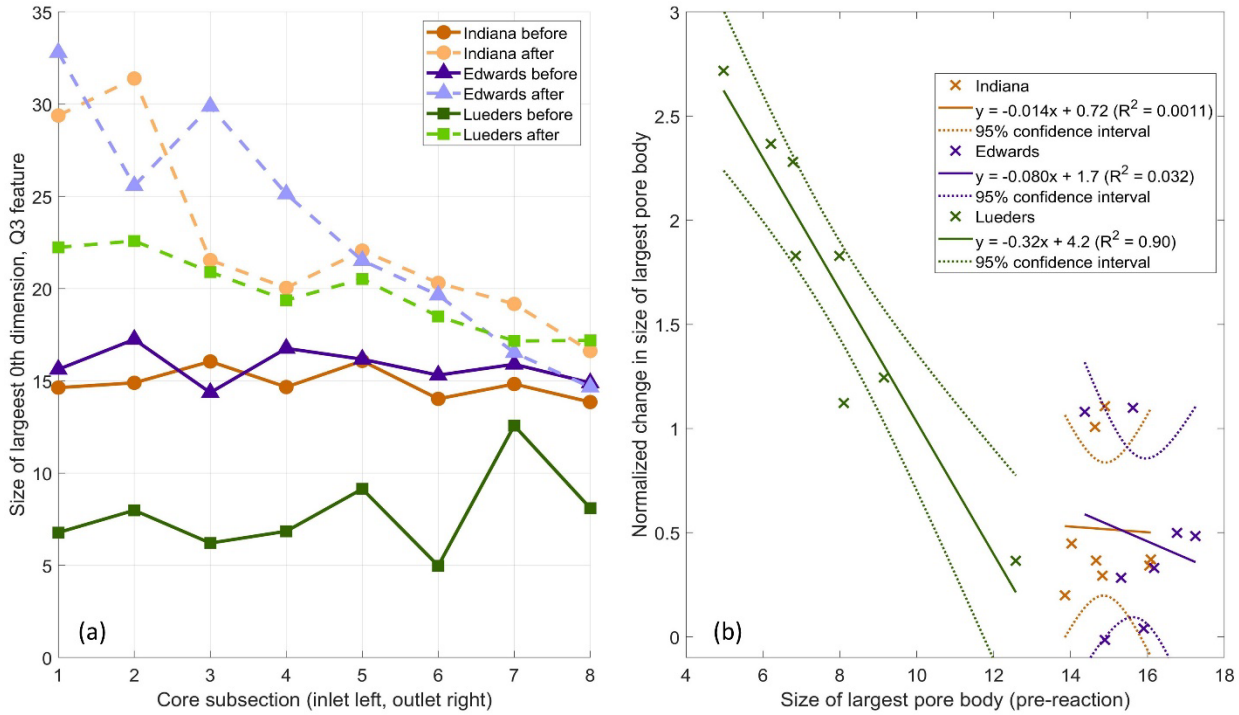

Figure 3.9: (a) Size of the largest 0^{th} dimension, Q3 feature before (solid) and after (dashed) reaction. (b) Change in size of the largest 0^{th} dimension, Q3 feature in each subsection (normalized by initial feature size) as a function of initial size. Markers indicate datapoints, solid lines indicate linear regressions fitted to each sample, and dotted lines indicate 95% confidence intervals around each regression.

change in different dissolving carbonates, but was not found to be useful for predicting regions of change within a given rock core.

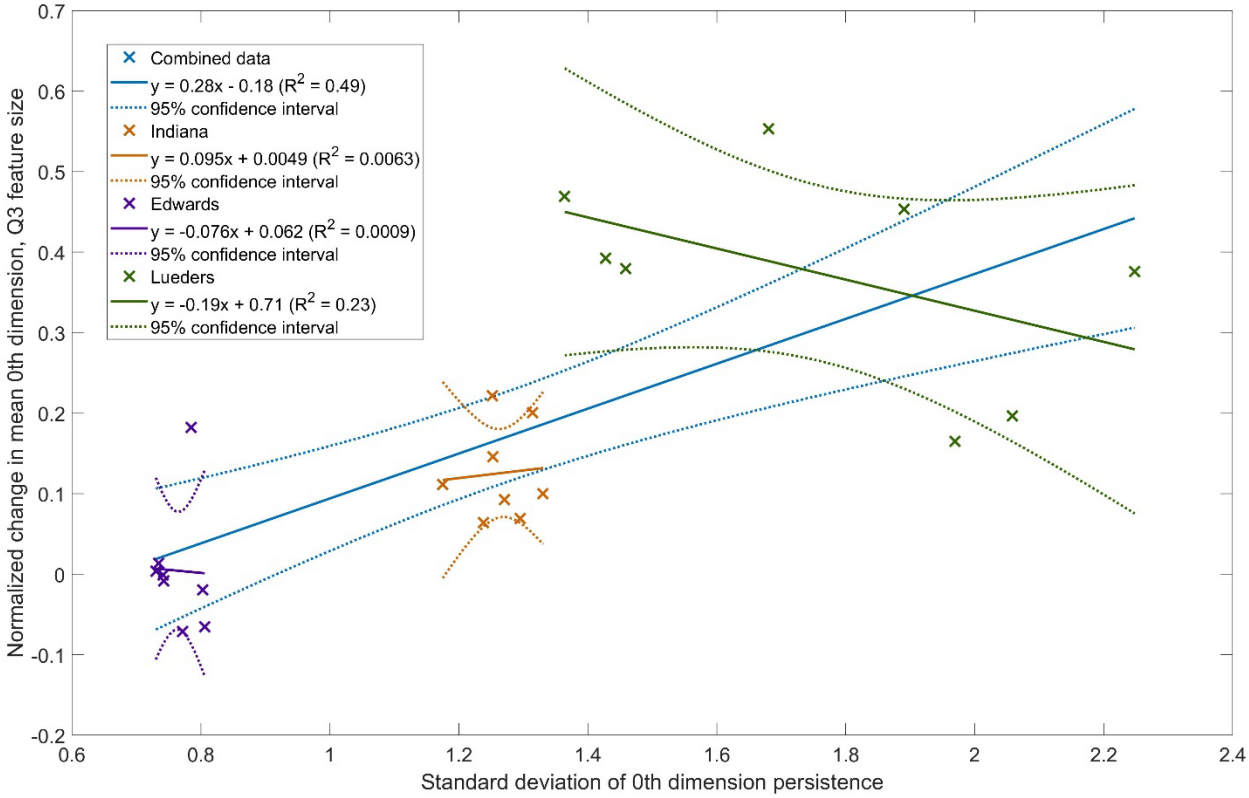

Figure 3.10: Percent change in the mean size of 0th dimension, Q3 features as a function of the initial standard deviation of persistence of all 0th dimension features. Indiana Limestone data are shown in orange, Edwards Limestone data in purple, and Lueders Limestone data in green. Linear regressions are fitted to each set of sample data, as well as in aggregate (blue).

As discussed previously, the 1st dimension features saw little change over the course of reaction, suggesting that changes in looping features did not contribute substantively to permeability change. Boxplots of 1st dimension, Q2 and Q3 feature persistence values are available in Appendix Figure B.5. These values represent the difference between the narrowest pore throat that makes up the loop and the diameter of the grain (Q2) or narrowing region (Q3) that the loop encircles. Changes in each rock core were minor and consistent along the length of the core. This suggests that along-core heterogeneity did not affect 1st dimension feature evolution as much as it did 0th dimension feature evolution. Indiana Limestone (orange) showed

a slight increase in persistence across distribution in each subsection. This is consistent with erosion causing the inner radii of toroidal pore features to decrease.

Edwards Limestone (purple) had a very small decrease in median persistence, which could indicate that the largest features in this dimension merged with other features during dissolution. The Lueders Limestone (green) 1st dimension features had a very tight distribution prior to reaction and saw little change during reaction, other than the appearance of a few large outliers which could again be due to dissolution around a few key narrow points in the mineral space. In this analysis, it is important to note the decrease in overall counts of features in Q2 and Q3 during dissolution: the post-dissolution number of 1st dimension features is a small fraction of the initial number. Many of the loops formed by narrow points in the grain features of original rock cores were washed out during the course of dissolution, so it is only possible to observe the distributions of the limited number that remained after dissolution.

The results of this study support the hypothesis that pore space homology is an important factor in driving regions of larger effects of dissolution, but this is just one among many parameters – both properties of the rocks themselves and reactive flow conditions – that contribute. It is well established that the reactive transport regime, described by the dimensionless Damköhler (Da) and Péclet (Pe) numbers, influence the progression of porosity and permeability in dissolving carbonates (Gouze & Luquot, 2011; Hommel et al., 2018; M. Liu & Mostaghimi, 2017; Mostaghimi et al., 2016; Zhang et al., 2022). Advective Da is a dimensionless parameter that describes the relative importance of advective transport versus chemical kinetics. It is defined as the ratio of the characteristic time of advection to the characteristic time of reaction. A system with a high Da is transport-limited: the chemical reaction outpaces the rate at which unreacted fluid is carried to reaction sites. Pe describes the

relative importance of advective versus diffusive transport and is defined as the ratio of the characteristic time of diffusion to the characteristic time of advection. High Pe indicates a system in which advective flow dominates mass transport. In a laboratory environment using natural rock, precise control of Da and Pe is challenging due to the constantly evolving porosity and reactive surface area. Advective Da was estimated to be on the order of 10^3 to 10^5, and Pe was estimated to be on the order of 10^4 to 10^5, indicating that the reaction was transport-limited and that advective flow dominated over dispersion. A full table of values used for these calculations is available in Appendix Table B.2. The presence of large preferential channels supports the assumption that these experiments were transport-limited and that advection dominated over diffusion, consistent with the findings of Kalia & Balakotaiah, (2007) and Kang et al., (2003). This likely contributed to the enlargement of the largest pore bodies within existing flow channels, whereas a uniform dissolution regime may see more uniform change. The growth of connected pores along existing flow channels is consistent with extensive prior research into the formation and propagation of preferential flowpaths in dissolving carbonates, whereby increased flow velocity in high permeability regions carries more acid to those regions, causing accelerated dissolution relative to other areas of the sample (Fredd & Fogler, 1998; Hoefner & Fogler, 1988). The homogenization of large pore sizes along the flow path (particularly in the Lueders sample) is similar to prior observations of wormhole formation (Rötting et al., 2015; Siddiqui et al., 2006). Future work could use numerical simulations to investigate the relationship between pore space topology evolution and reactive transport regime based on natural rock samples.

3.5 Conclusions

Persistent homology provides a metric of pore network heterogeneity that incorporates both pore size and connectivity information. This analysis can help identify locations within a

porous rock medium that are most likely to change during dissolution and the degree to which pore bodies in a flow path will expand. It also offers a more detailed understanding of the mechanisms by which permeability increases in a dissolving carbonate.

In this study, the two more homogenous limestone cores saw similar behavior: permeability changes were driven by increase in size of large, connected pores. These changes were more pronounced near the inlet, suggesting the initiation of preferential flow paths along the core which were confirmed by visual observation of the XCT data. The more heterogeneous core saw an increase in along-core homogeneity after dissolution. Its largest pores saw little change in size while its smaller controlling pores grew to match the largest. This sample contained a single very large flow path after reaction, and the differences in pore size change are expected to be due to differences in surface area-to-volume ratios.

The initial size of the largest connected pore body showed strong negative correlation with the degree of large pore body size increase in the most heterogeneous core, suggesting that the largest pores in the media were relatively unchanged over the course of dissolution. This implies that even locally large pores along the length of the core can serve as controlling features of permeability increase in the presence of larger pores.

When the three samples were considered in aggregate, the standard deviation of persistence of pore bodies was found to have a moderate positive correlation with the normalized change in mean pore body size, suggesting that a sample with higher spatial variability of pore bodies experiences a greater increase in pore size, highlighting the importance of spatial heterogeneity in predicting dissolution behavior. However, within any individual sample this correlation did not hold, suggesting that differences in spatial variability within a single sample

were relatively unimportant for predicting size change within the sample. This discrepancy would be an interesting topic for future investigation but was beyond the scope of this study.

Improving the understanding of driving features of pore space evolution during dissolution can enhance predictions of porous media behavior in numerous subsurface applications. Through its combined information about pore body size, connectivity, and spatial heterogeneity, persistent homology can identify rock types and locations most susceptible to changes in the pore space.

3.6 References

Abbott, P. L. (1975). On the hydrology of the Edwards Limestone, south-central Texas. *Journal of Hydrology*, *24*(3–4), 251–269. https://doi.org/10.1016/0022-1694(75)90084-0

Arganda-Carreras, I., Kaynig, V., Rueden, C., Eliceiri, K. W., Schindelin, J., Cardona, A., & Sebastian Seung, H. (2017). Trainable Weka Segmentation: a machine learning tool for microscopy pixel classification. *Bioinformatics*, *33*(15), 2424–2426. https://doi.org/10.1093/bioinformatics/btx180

Bazaikin, Y., Gurevich, B., Iglauer, S., Khachkova, T., Kolyukhin, D., Lebedev, M., et al. (2017). Effect of CT image size and resolution on the accuracy of rock property estimates. *Journal of Geophysical Research: Solid Earth*, *122*(5), 3635–3647. https://doi.org/10.1002/2016JB013575

Boving, T. B., & Grathwohl, P. (2001). Tracer diffusion coefficients in sedimentary rocks: correlation to porosity and hydraulic conductivity. *Journal of Contaminant Hydrology*, *53*(1–2), 85–100. https://doi.org/10.1016/S0169-7722(01)00138-3

Buczynski, C., & Chafetz, H. S. (1987). Siliciclastic grain breakage and displacement due to carbonate crystal growth: an example from the Lueders Formation (Permian) of north-central Texas, U.S.A. *Sedimentology*, *34*(5), 837–843. https://doi.org/10.1111/j.1365-3091.1987.tb00807.x

Busenberg, E., & Plummer, L. N. (1986). *A comparative study of the dissolution and crystal growth kinetics of calcite and aragonite* (Studies in Diagenesis No. 1578). U.S. Geological Survey.

Carman, P. (1937). Fluid flow through granular beds, *15*, 150–166.

Delgado-Friedrichs, O., Robins, V., & Sheppard, A. (2015). Skeletonization and Partitioning of Digital Images Using Discrete Morse Theory. *IEEE Transactions on Pattern Analysis and Machine Intelligence*, *37*(3), 654–666. https://doi.org/10.1109/TPAMI.2014.2346172

Dodd, J. R., & Nelson, C. S. (1998). Diagenetic comparisons between non-tropical Cenozoic limestones of New Zealand and tropical Mississippian limestones from Indiana, USA: Is the non-tropical model better than the tropical model? *Sedimentary Geology*, *121*(1–2), 1–21. https://doi.org/10.1016/S0037-0738(98)00070-0

Dong, H., & Blunt, M. J. (2009). Pore-network extraction from micro-computerized-tomography images. *Physical Review E*, *80*(3), 036307. https://doi.org/10.1103/PhysRevE.80.036307

Elson, J. M., Rahn, J. P., & Bennett, J. M. (1983). Relationship of the total integrated scattering from multilayer-coated optics to angle of incidence, polarization, correlation length, and roughness cross-correlation properties. *Applied Optics*, *22*(20), 3207. https://doi.org/10.1364/AO.22.003207

Fredd, C. N., & Fogler, H. S. (1998). Influence of transport and reaction on wormhole formation in porous media. *AIChE Journal*, *44*(9), 1933–1949. https://doi.org/10.1002/aic.690440902

Gouze, P., & Luquot, L. (2011). X-ray microtomography characterization of porosity, permeability and reactive surface changes during dissolution. *Journal of Contaminant Hydrology*, *120–121*, 45–55. https://doi.org/10.1016/j.jconhyd.2010.07.004

Herring, A. L., Robins, V., & Sheppard, A. P. (2019). Topological Persistence for Relating Microstructure and Capillary Fluid Trapping in Sandstones. *Water Resources Research*, *55*(1), 555–573. https://doi.org/10.1029/2018WR022780

Hoefner, M. L., & Fogler, H. S. (1988). Pore evolution and channel formation during flow and reaction in porous media. *AIChE Journal*, *34*(1), 45–54. https://doi.org/10.1002/aic.690340107

Hommel, J., Coltman, E., & Class, H. (2018). Porosity–Permeability Relations for Evolving Pore Space: A Review with a Focus on (Bio-)geochemically Altered Porous Media. *Transport in Porous Media*, *124*(2), 589–629. https://doi.org/10.1007/s11242-018-1086-2

Jiang, F., Tsuji, T., & Shirai, T. (2018). Pore Geometry Characterization by Persistent Homology Theory. *Water Resources Research*, *54*(6), 4150–4163. https://doi.org/10.1029/2017WR021864

Kalia, N., & Balakotaiah, V. (2007). Modeling and analysis of wormhole formation in reactive dissolution of carbonate rocks. *Chemical Engineering Science*, *62*(4), 919–928. https://doi.org/10.1016/j.ces.2006.10.021

Kang, Q., Zhang, D., & Chen, S. (2003). Simulation of dissolution and precipitation in porous media. *Journal of Geophysical Research: Solid Earth*, *108*(B10). https://doi.org/10.1029/2003JB002504

Kozeny, J. (1927). Uber kapillare Leitung das Wassers im Boden. *Royal Academy of Science, Vienna, Proc. Class I*, *136*, 271–306.

Lai, P., Moulton, K., & Krevor, S. (2015). Pore-scale heterogeneity in the mineral distribution and reactive surface area of porous rocks. *Chemical Geology*, *411*, 260–273. https://doi.org/10.1016/j.chemgeo.2015.07.010

Lisitsa, V., Bazaikin, Y., & Khachkova, T. (2020). Computational topology-based characterization of pore space changes due to chemical dissolution of rocks. *Applied Mathematical Modelling*, *88*, 21–37. https://doi.org/10.1016/j.apm.2020.06.037

Liu, M., & Mostaghimi, P. (2017). Characterisation of reactive transport in pore-scale correlated porous media. *Chemical Engineering Science*, *173*, 121–130. https://doi.org/10.1016/j.ces.2017.06.044

Liu, S., & Huang, Z. (2021). Analysis of strength property and pore characteristics of Taihang limestone using X-ray computed tomography at high temperatures. *Scientific Reports*, *11*(1), 13478. https://doi.org/10.1038/s41598-021-92928-z

Moon, C., Mitchell, S. A., Heath, J. E., & Andrew, M. (2019). Statistical Inference Over Persistent Homology Predicts Fluid Flow in Porous Media. *Water Resources Research*, *55*(11), 9592–9603. https://doi.org/10.1029/2019WR025171

Morrow, N., & Buckley, J. (2006). *Wettability and Oil Recovery by Imbibition and Viscous Displacement from Fractured and Heterogeneous Carbonates* (Technical Report No. DE-FC26-02NT15344). University of Wyoming. Retrieved from https://www.osti.gov/servlets/purl/888663

Mostaghimi, P., Blunt, M. J., & Bijeljic, B. (2013). Computations of Absolute Permeability on Micro-CT Images. *Mathematical Geosciences*, *45*(1), 103–125. https://doi.org/10.1007/s11004-012-9431-4

Mostaghimi, P., Liu, M., & Arns, C. H. (2016). Numerical Simulation of Reactive Transport on Micro-CT Images. *Mathematical Geosciences*, *48*(8), 963–983. https://doi.org/10.1007/s11004-016-9640-3

Peng, S., Hu, Q., Dultz, S., & Zhang, M. (2012). Using X-ray computed tomography in pore structure characterization for a Berea sandstone: Resolution effect. *Journal of Hydrology*, *472–473*, 254–261. https://doi.org/10.1016/j.jhydrol.2012.09.034

Prokhorov, D., Lisitsa, V., Khachkova, T., Bazaikin, Y., & Yang, Y. (2022). Topology-based characterization of chemically-induced pore space changes using reduction of 3D digital

images. *Journal of Computational Science*, *58*, 101550. https://doi.org/10.1016/j.jocs.2021.101550

Qajar, J., & Arns, C. H. (2022). Chemically Induced Evolution of Morphological and Connectivity Characteristics of Pore Space of Complex Carbonate Rock via Digital Core Analysis. *Water Resources Research*, *58*(3). https://doi.org/10.1029/2021WR031298

Robins, V, Wood, P. J., & Sheppard, A. P. (2011). Theory and Algorithms for Constructing Discrete Morse Complexes from Grayscale Digital Images. *IEEE Transactions on Pattern Analysis and Machine Intelligence*, *33*(8), 1646–1658. https://doi.org/10.1109/TPAMI.2011.95

Robins, Vanessa, Saadatfar, M., Delgado-Friedrichs, O., & Sheppard, A. P. (2016). Percolating length scales from topological persistence analysis of micro- CT images of porous materials. *Water Resources Research*, *52*(1), 315–329. https://doi.org/10.1002/2015WR017937

Rötting, T. S., Luquot, L., Carrera, J., & Casalinuovo, D. J. (2015). Changes in porosity, permeability, water retention curve and reactive surface area during carbonate rock dissolution. *Chemical Geology*, *403*, 86–98. https://doi.org/10.1016/j.chemgeo.2015.03.008

Siddiqui, S., Nasr-El-Din, H. A., & Khamees, A. A. (2006). Wormhole initiation and propagation of emulsified acid in carbonate cores using computerized tomography. *Journal of Petroleum Science and Engineering*, *54*(3–4), 93–111. https://doi.org/10.1016/j.petrol.2006.08.005

Sukop, M. C., Huang, H., Alvarez, P. F., Variano, E. A., & Cunningham, K. J. (2013). Evaluation of permeability and non-Darcy flow in vuggy macroporous limestone aquifer samples with lattice Boltzmann methods. *Water Resources Research*, *49*(1), 216–230. https://doi.org/10.1029/2011WR011788

Suzuki, A., Miyazawa, M., Minto, J. M., Tsuji, T., Obayashi, I., Hiraoka, Y., & Ito, T. (2021). Flow estimation solely from image data through persistent homology analysis. *Scientific Reports*, *11*(1), 17948. https://doi.org/10.1038/s41598-021-97222-6

Szymczak, P., & Ladd, A. J. C. (2011). Instabilities in the dissolution of a porous matrix. *Geophysical Research Letters*, *38*(7). https://doi.org/10.1029/2011GL046720

Thompson, E. P., Tomenchok, K., Olson, T., & Ellis, B. R. (2021). Reducing User Bias in X-ray Computed Tomography-Derived Rock Parameters through Image Filtering. *Transport in Porous Media*, *140*(2), 493–509. https://doi.org/10.1007/s11242-021-01690-3

Thompson, Ellen P., & Ellis, B. R. (2023). Persistent Homology as a Heterogeneity Metric for Predicting Pore Size Change in Dissolving Carbonates Dataset [Data set]. University of Michigan - Deep Blue Data. https://doi.org/10.7302/X0ZZ-M727

Varnes, D., Finnell, T., & Post, E. (1958). *Graphic-locator method in geologic mapping* (Geological Survey Bulletin No. 1081- A).

Yoo, H., Kim, Y., Jang, H., & Lee, J. (2021). Propagation characteristics of optimum wormhole in carbonate matrix acidizing using micro X-ray CT imaging. *Journal of Petroleum Science and Engineering*, *196*, 108010. https://doi.org/10.1016/j.petrol.2020.108010

Zhang, Y., Jiang, F., & Tsuji, T. (2022). Influence of pore space heterogeneity on mineral dissolution and permeability evolution investigated using lattice Boltzmann method. *Chemical Engineering Science*, *247*, 117048. https://doi.org/10.1016/j.ces.2021.117048

Chapter 4 Evolving Scales of Heterogeneity in Dissolving Limestones Analyzed with XCT-Derived Fractal Dimension

4.1 Introduction

Accurate prediction of carbonate dissolution patterns is essential for the safety and sustainability of numerous subsurface energy applications, including carbon capture utilization and storage (CCUS), geothermal energy production, and enhanced oil recovery (EOR). Dissolution fronts in carbonates can vary widely depending on injection conditions, reservoir chemistry, and physical rock characteristics. Of particular interest are large preferential flow channels that create regions of high permeability and alter the reactive transport regime during flow. In some applications, these preferential flowpaths are desirable because they enable high fluid throughput and extend reach into distal regions of the reservoir; in others they are undesirable because they carry unbuffered reactive fluid deep into the reservoir while leaving other regions near the wellbore untouched. Predicting the development and spatial characteristics of such flowpaths is therefore broadly applicable for subsurface energy projects. Centimeter-scale core plugs are commonly used to estimate petrophysical properties of target reservoirs. It is essential to quantify and analyze the importance of core- and sub-core-scale heterogeneities on dissolution front characteristics and preferential flowpath development. It is also important to observe how the scales of these heterogeneities change over the course of dissolution, as this knowledge can help optimize modeling parameters. X-ray computed tomography (XCT) imaging is an excellent tool for heterogeneity analysis because it allows nondestructive visualization of the pore structures and distribution in these core plug samples.

The fractal dimension (FD) is a quantitative metric of geometric complexity that has been used in the geosciences, including to describe pore space and wormholes formed by dissolution in carbonates. FD was introduced by mathematician Benoit Mandelbrot to describe a curve or shape using non-integer dimensions (Mandelbrot, 1967). A smooth curve occupies very little 2D space and may therefore be approximated as a 1D Euclidean object. A rough curve, however, fills more 2D space and behaves as an object existing between the 1st and 2nd dimensions. An object's FD is a ratio of the space it occupies to the scale at which it is observed. A classical example of this is the coastline paradox, which states that the length of a coastline of a landmass apparently increases when the landmass is observed at closer scale. By measuring the coastline of Great Britain using varying scales of measurement, Mandelbrot found its FD to be 1.25 (Mandelbrot, 1967).

The FD of wormholes resulting from dissolution has been an area of interest in carbonate research for many years as it gives a quantitative parameter with which to compare wormhole complexity (Kalia & Balakotaiah, 2007). In a series of numerical simulations, Maheshwari et al. (2013) investigated the influence of porous media heterogeneity on the FD of resulting wormholes and found an exponential relationship between porosity variability and wormhole FD, supporting the hypothesis that greater pore space heterogeneity results in more complex branching in preferential flowpaths. Liu et al. (2012) modeled wormhole formation under different acid strength and injection conditions and used the FD of acid-etched wormholes to recommend injection conditions for reservoir treatment near oil production wells. Optimization of this parameter can aid in the extractive industries as well as in carbon utilization and other sustainable subsurface energy technologies.

Other, recent works have studied FD of the initial pore network as a predictor of other physical properties. Zhou et al. (2022) used SEM image analysis to study the relationship between pore space FD and diagenetic markers and found a positive linear relationship between FD and both diagenetic dissolution and precipitation in sandstones. Wu et al. (2019) observed consistent variation trends between porosity and FD calculated from XCT data along the length of a low permeability sandstone core. Zhang et al. (2018) found good negative correlation between pore space FD estimated from MICP data and porosity, permeability, sorting coefficient, and skewness. Fu et al. (2019) studied the FD of pore space that formed in manufactured geomaterials and found good correlation between FD (measured from XCT imagery taken at 40 μm voxel size) and porosity, pore shape factor, and pore surface area in aerated concrete blocks. To date, no known work has examined the relationship between the FD of the initial pore network and that of the resulting preferential flowpath.

Numerous prior works have studied the relationship between injection conditions, characterized by the Péclet (Pe), advective Damköhler (Da_I), and diffusive Damköhler (Da_{II}) numbers, and dissolution regime. These studies observe that preferential flowpath formation is promoted by high advective flow and reaction rates relative to diffusion rates (high Pe and Da_{II}). Such conditions concentrate flow (and therefore carry more reactive fluid) along paths of least resistance, exacerbating existing flow channels (Mostaghimi et al., 2016). In an engineered system, forced injection of reactive fluid can create regions of advective-controlled flow, increasing the possibility of wormhole-like features rather than strictly uniform dissolution, so it is valuable to consider means of predicting the properties of such flowpaths.

Injection conditions cannot be considered in isolation from the properties of the rocks themselves when injecting into natural geologic formations. The degree to which pore-scale

heterogeneities influence core- to reservoir-scale heterogeneities is an open area of research. Prior work suggests that such heterogeneities are more important in systems with high Pe and Da_I (Y. Zhang et al., 2022). Other modeling work suggests that nonreactive flow regime in a porous medium becomes less sensitive to Pe as the spatial distribution of pores becomes more heterogeneous (Babaei & Joekar-Niasar, 2016). Similarly, in a study that incorporated reactive flow to simulations of dissolving carbonates with varying degrees of spatial self-similarity, the reaction front destabilized at wider Pe range when the pore network had a higher correlation length (Min Liu & Mostaghimi, 2017). In experimental studies, the presence of heterogeneities such as vugs and styolites has been associated with unstable reaction front formation and wormhole-like structures (Carroll et al., 2013; Siddiqui et al., 2006). Menke et al. (2018) observed higher focusing of preferential flowpaths in a limestone with an initially heterogeneous flowfield compared to one with more homogenous streamlines. These experimental findings are consistent with modeling efforts that also suggest that pore space heterogeneities can initiate the formation of unstable reaction fronts (Hao et al., 2019).

Dissolution can cause an increase in the magnitude of pore space heterogeneities measured transverse to flow. This has been observed as an increase in variance of velocity distribution (Menke et al., 2015). It follows that the correlation length of pore space, or other similar metrics of spatial clustering, would be expected to increase in the plane transverse to flow following nonuniform dissolution. Along the axis of flow, however, heterogeneity of the pore space has been observed to decrease. Pereira Nunes et al. (2016) observed an increase in homogeneity along the axis of flow following dissolution, according to two metrics: a narrowing of the slice-averaged velocity distribution curve and a tendency for slice-average porosity to increase more in low-porosity slices. Thompson et al. (2021) observed an increase in along-core

heterogeneity as measured by the size of the largest macropores and the skewness of the pore size distribution. Little known work to date has quantified the increase in spatial scale of heterogeneity either transverse or longitudinal to flow.

In this study, we compared the FD of the initial pore space to that of the pore space post-dissolution. We also examined the relationship between the FD of the initial pore network and that of the resulting preferential flowpath formed through dissolution. We quantified the FD of three limestone cores using XCT scans, then induced dissolution using dilute acid with a high-pressure core flooding apparatus, and isolated and analyzed the preferential flow channels using repeat XCT imaging. We used spectral analysis to study the scales of variability of the pore space before and after dissolution and found that the post-reaction pore space had higher variance, which was dominated by lower-frequency spectral signals. This indicated a growth in the spatial scale of pore space heterogeneities. We also observed strong positive correlation between pore space FD and flow channel FD, suggesting that more geometrically complex pore space is associated with more branching behavior in preferential flowpaths. Using XCT imagery, we can identify important scales of heterogeneity. We can then make more informed predictions of formations and locations within formations that may experience channeling or branching of preferential flowpaths.

4.2 Materials and Methods

4.2.1 Experimental methods

Three limestone cores -- Indiana, Edwards, and Lueders Limestone -- of 2.5 cm in diameter and 4 cm in length were studied using a series of core flooding and imaging iterations.

Cores were pre-saturated under vacuum prior to flooding. Flooding experiments were performed in a high-pressure flowthrough apparatus. Permeability was determined by flowing

deionized water through the cores at five different flow rates, monitoring the upstream-downstream pressure differential, and calculating permeability using Darcy's Law. Confining pressure was maintained with water, surrounding the core held in a viton sleeve, at least 3.4 MPa (500 psi) higher than flow pressure. The outlet side of the core was open to atmospheric pressure, and an inlet flow plug maintained a constant volumetric flowrate. Hydrochloric acid diluted to pH 3 was flowed through the cores to induce dissolution. Pre- and post-reaction permeability and porosity values are included in Table 4.1.

Table 4.1: Permeability and porosity values for each core.

	Sample	Indiana	Edwards	Lueders
Pre-reaction	Porosity (Saturation method)	0.17	0.25	0.11
	Permeability (mD)	32	9.8	0.12
Post-reaction	Porosity (Saturation method)	0.18	0.27	0.13
	Permeability (mD)	240	170	54

Precise control of Damköhler and Péclet numbers in an experimental setting is challenging, but effort was made to maintain consistent reactive transport regimes (Da_I and Pe >> 1) for all three samples. With an estimated Da_I on the order of 10^3 to 10^5 and an estimated Pe on the order of 10^4 to 10^5 (see Appendix Table C.2f for values used in these estimations), it is reasonable to assume that transport controlled the reaction rate and advection dominated over dispersion.

4.2.2 Imaging and image processing methods

The cores were flushed with water to remove residual acid, then vacuum dried prior to imaging. They were imaged at a voxel resolution of 15 µm using a Nikon XT H 225 ST

industrial CT scanner at the Computed Tomography in Earth and Environmental Sciences (CTEES) laboratory at the University of Michigan. Additional scan parameters are listed in Appendix Table C.1. XCT scanning has an inherent tradeoff between image resolution and field of view; this was the highest resolution at which visualization of the full core diameter was possible using this instrument. Prior work suggests that it is reasonable to assume that FD calculated from XCT data would agree well with a higher-resolution imaging technique. Alfonso et al. (2018) performed a comparative study using scanning electron microscopy (SEM) (0.4 μm/pixel), optical microscopy (OM) (91 μm/pixel), and XCT (260 μm/pixel) and found that the FD was consistent across the three methods. So, while the image datasets used for this study are only able to resolve the macropores of each core sample, it is assumed that the fractal characteristics of those macropores are sufficiently representative of the fractal characteristics of the full (resolved and unresolved) pore network.

After cropping out scanning artifacts near the edge of each core, the resulting image stacks were 2000x2000x2000 voxels. Other scan parameters are included in the Supporting Information (Appendix Table C.1). The images were processed using an unsharp mask filter for contrast enhancement, a bilateral filter for noise reduction, and a beam hardening correction. This filter combination was selected based on prior work by Thompson et al. (2021), which found that these three filters resulted in porosity values that had lower variability and were more consistent with experimental findings. The processed datasets were segmented by machine learning using the Trainable Weka Segmentation plugin for ImageJ (Arganda-Carreras et al., 2017). An example image from each pre-reaction XCT scan before processing, after processing, and after segmentation is shown in Figure 4.1.

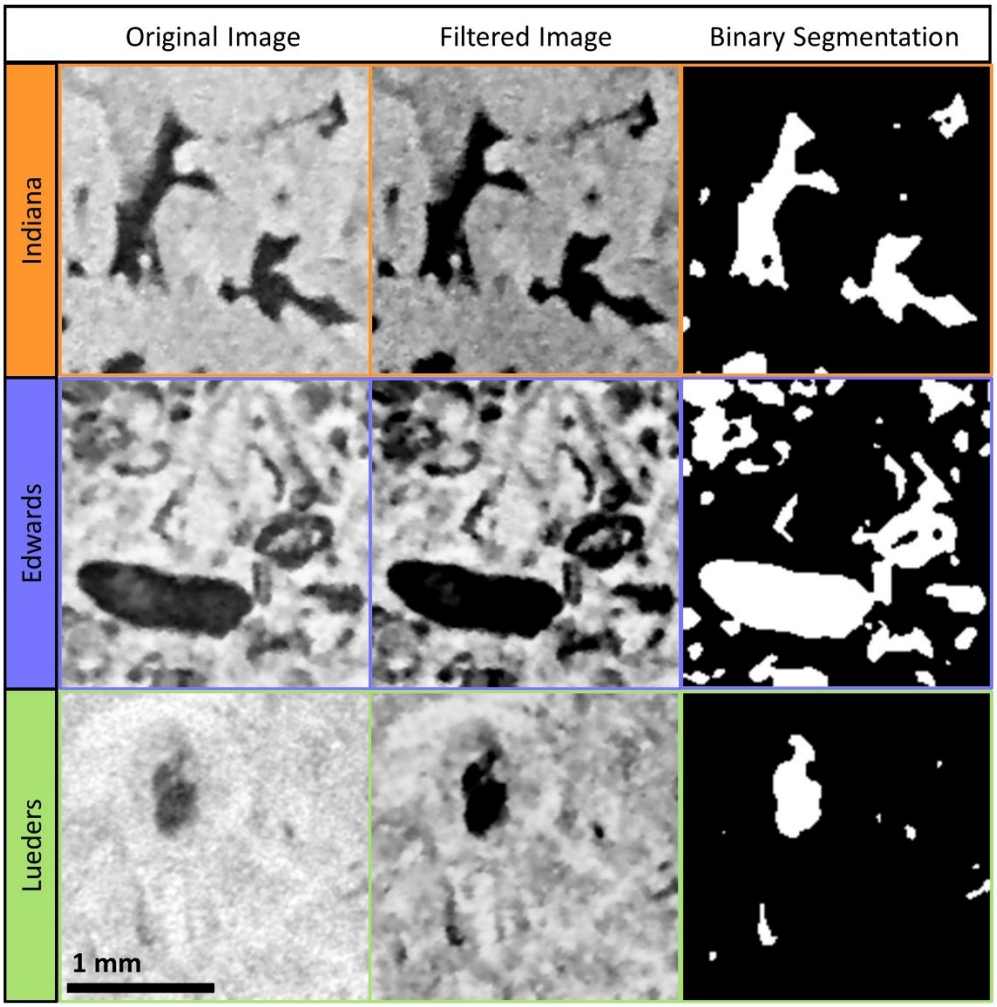

Figure 4.1: Sample image taken from pre-reaction XCT scan of each sample (top to bottom: Indiana, Edwards, Lueders) demonstrating original image (left), processed image (center), and segmented image (right). Figure reprinted with permission from Thompson et al. (2023).

4.3 Data

The image datasets were cropped to 1024x1024x2000 voxels to isolate the core from its background while creating square images of a power of 2 pixels per 2D image slice. Each of the 2000 slices was analyzed using the box counting algorithm with the hausDim package for MATLAB (Costa, 2023). This algorithm begins by creating boxes with a side length ε of one pixel and records the number of occupied boxes as N(ε). It then doubles the box side length to ε = 2 and again records the number of occupied boxes, N(2). This process continues until the side

length is equal to the size of the full image, ε =1024. The number of occupied boxes as a function of the size of the boxes is plotted on a log-log scale. A line is fitted to the data using the least-squares method, and the slope of this line is the FD (Figure 4.2).

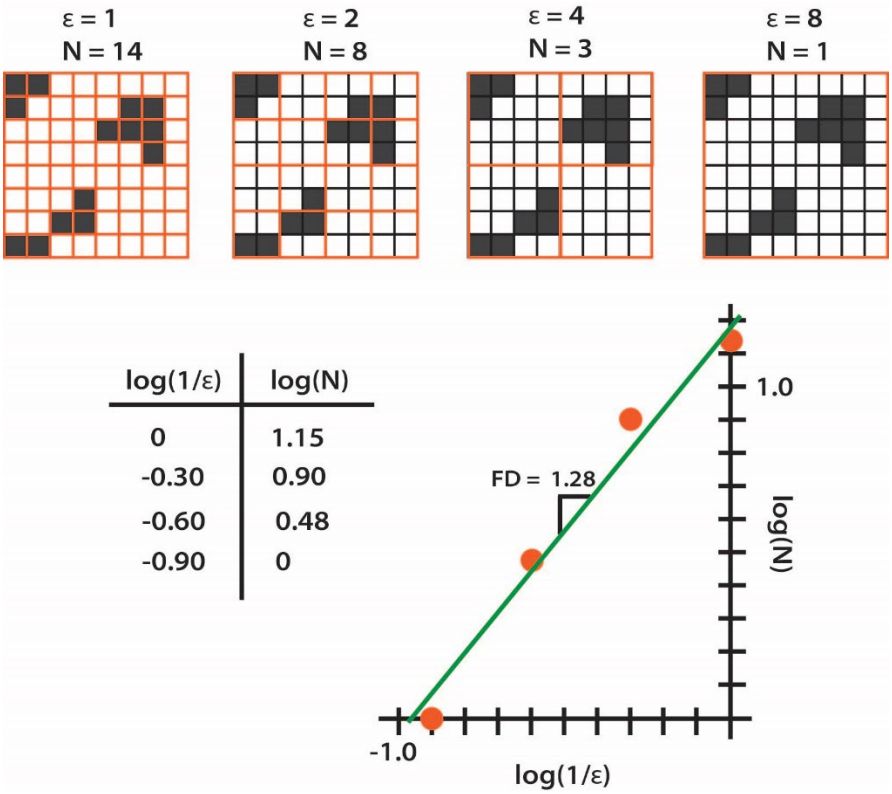

Figure 4.2: Demonstration of the box counting algorithm. The box side length ε increases by powers of 2 and the number of occupied squares is recorded as N(ε). The slope of the log(1/ ε) vs log(N) graph is the fractal dimension FD.

The FD was calculated for each 2D image slice along the length of the core for the pre-reaction pore space, post-reaction pore space, and post-reaction preferential flow path. The autocorrelation of the FD along the flowpath was calculated, and the correlation length was computed. Correlation length describes the spatial scale at which a variable is self-similar and can take on various specific quantitative definitions by discipline. Here it refers to the distance at which the autocorrelation function falls below a value of 1/e (Elson et al., 1983). To reduce the influence of spurious oscillations in the autocorrelation function, 1000 realizations of a Gaussian white noise process with the same variance as that of the sample were generated and plotted

along with the sample autocorrelation. Their upper and lower bounds were used to create confidence intervals about the autocorrelation function.

The FD along the length of the core was analyzed as a spectral series. The datasets had been divided into 250-slice subsections for segmentation due to processing constraints. This resulted in artifacts in the first and last slice of each subsection and discontinuities between subsections. The anomalous values were excluded from analysis and discontinuities were smoothed. The spectral signal was estimated using the Bartlett window closing technique. This is a nonparametric empirical approach to spectral estimation. The process involves computing smoothed spectral estimates with progressively smaller bandwidths and allowing prominent features to emerge. Wide bandwidths tend to have high bias but low variance and can only capture large features in the spectrum. Narrow bandwidths tend towards low bias and high variance and can allow for more detailed observations but with the possibility of instability in the spectral estimate. The objective is to select a bandwidth at which the estimates have converged but have not yet destabilized (Jenkins & Watts, 1968). Window shape can sometimes impact the spectral density estimate; Tukey and Parzen lag windows were also tested and produced nearly identical results.

For the post-reaction scans, the large preferential flowpath was identified through visual inspection and the path was isolated using a 4-neighbor floodfill operation starting at the inlet of the core. This scan, too, was cropped to 1024x1024x2000 voxels, ensuring that the full preferential flow path was included (Figure 4.3). The Indiana and Edwards samples showed larger, branching pathways of preferential dissolution, whereas the Lueders sample was dominated by a single, large channel. This was consistent with the observations of Hao et al. (2019), who found in upscaled simulations that more permeable rocks tended to form multiple

dissolution fingers along the direction of flow, whereas less permeable rocks tended to form a single dissolution channel.

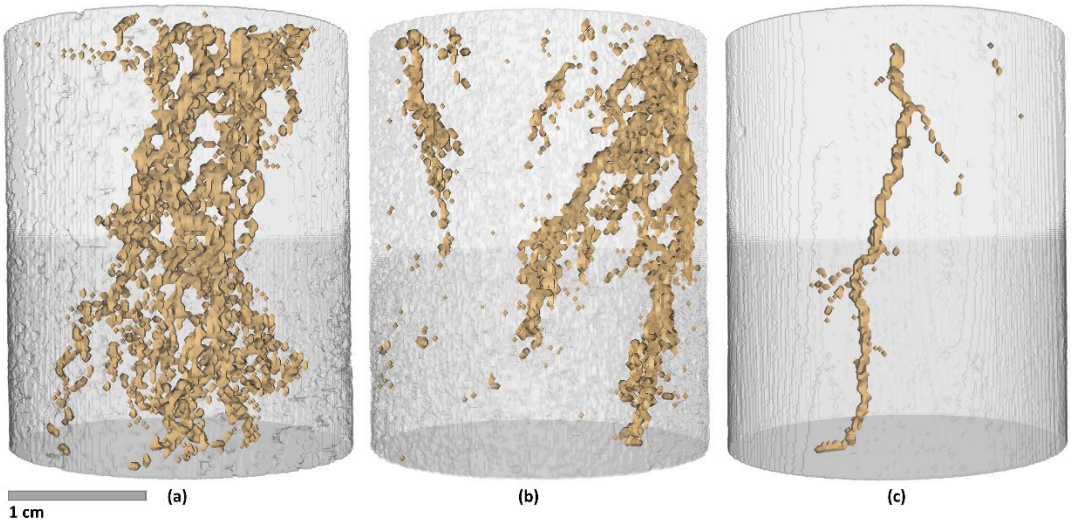

Figure 4.3: 3D tomograms highlighting large preferential flowpaths that formed in each core: (a) Indiana, (b) Edwards, and (c) Lueders Limestone. Reproduced from Thompson & Ellis (2023).

4.4 Results

The FD of the pore space of each image slice was plotted from inlet to outlet for all three cores, before and after chemical reaction. This is shown in Figure 4.4. Indiana and Edwards samples had relatively high, relatively homogeneous FD prior to reaction, and both experienced a drop in FD mean and an increase in FD variance after reaction. These permeable samples had a high porosity and complex pore space along the length of the core, and the drop in mean FD is consistent with a smoothing of complex pore space. This could be due to the dissolution of constriction points resulting in a rounder, smoother flow space, consistent with the observations of Pereira Nunes et al. (2016) and others. The increase in variance could indicate regions of channeling and branching that emerge as the preferential flowpath develops. The Lueders sample, on the other hand, looked quite different before reaction and evolved differently. This sample had a great deal of along-core heterogeneity and a very low overall FD compared to the

other two samples. It showed a modest increase in mean FD after reaction and an increase in variance. This could be due to the presence of large, vuggy pore structures irregularly distributed along the length of the core. The preferential flowpath that developed in Lueders and dominated the post-reaction flow space (shown above in Figure 4.3) was still very smooth and had distinct branches out from the main channel.

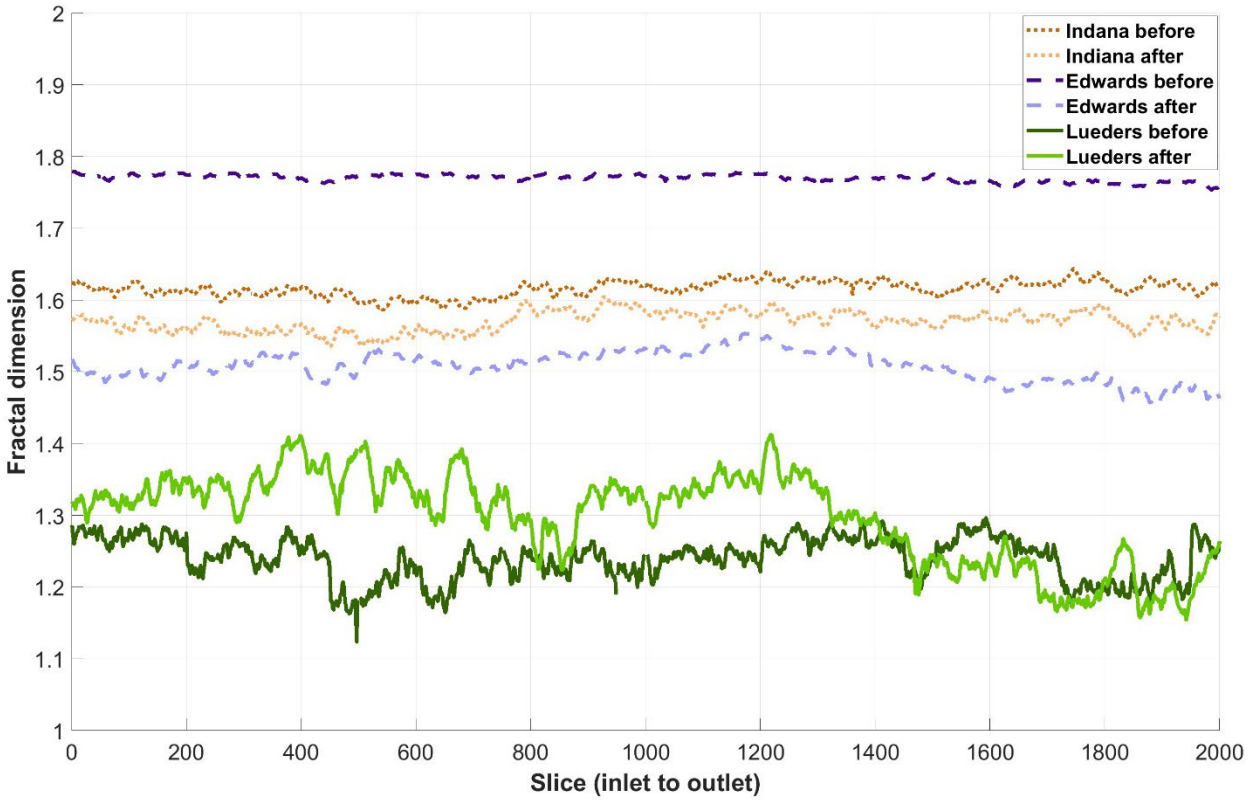

Figure 4.4: The fractal dimension for each core: Indiana (orange dots), Edwards (purple dashes), and Lueders (green solid line). The FD before reaction is shown in dark color, and after reaction in light color. Each slice is 15 μm in length.

The FD of the pre-reaction pore space was compared to the FD of the post-reaction pore space. Figure 4.5 shows the autocorrelation function of the FD for each sample pre- and post-reaction. The confidence intervals generated by realizations of a Gaussian white noise process as described above are shown in light color. The correlation length is shown using a dashed gray line. These results indicate an increase in correlation length for all three samples after reaction.

This suggests that the spatial scale of heterogeneity increased after reaction, and a larger REV would be necessary to fully capture the heterogeneities in fractal dimension after reaction than would be needed pre-reaction. These three samples show a negative relationship between the initial correlation length and the degree of correlation length increase. This may indicate that if the scale of heterogeneities is large prior to reaction, those heterogeneities may be exacerbated but remain roughly the same size. In samples with smaller-scale self-similarity, minor perturbations in the flow field could result in larger-scale regions of similar degrees of complexity.

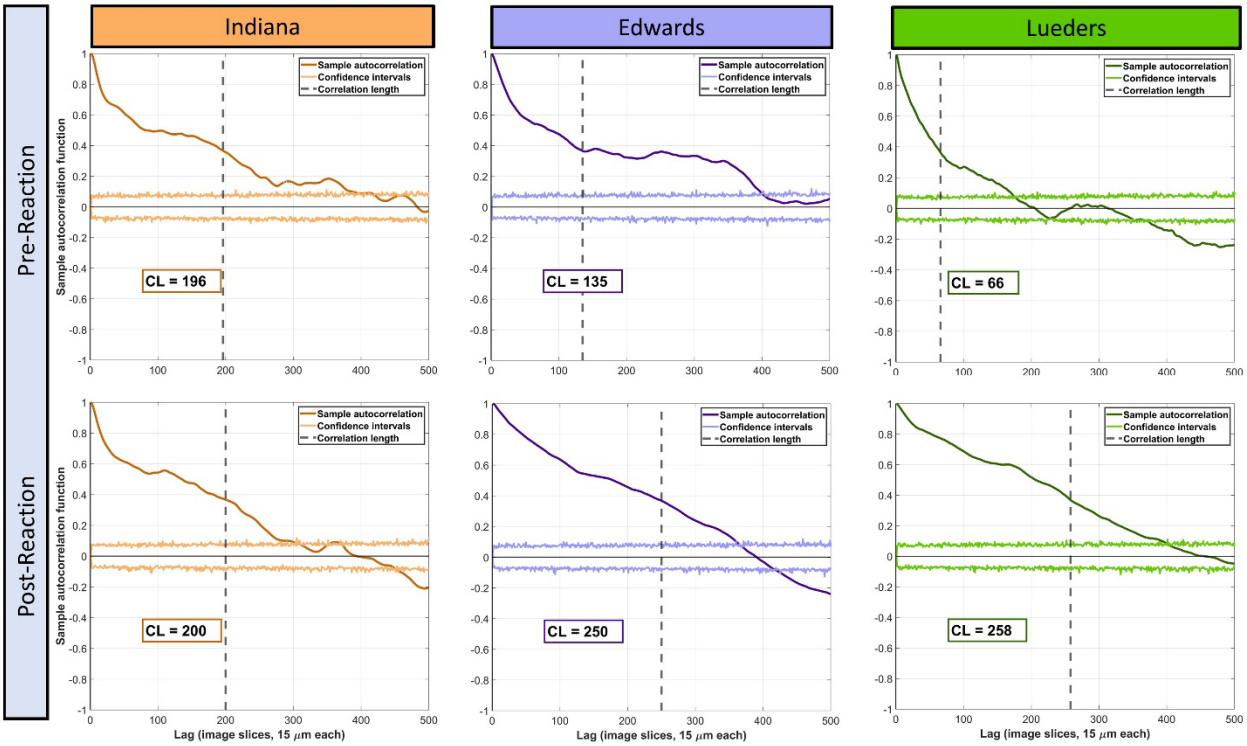

Figure 4.5: Autocorrelation functions for the three samples pre- and post-reaction. Confidence intervals are shown in light color and correlation length is indicated with a dashed gray line.

The spectral signals of the pre-reaction and post-reaction pore spaces were estimated using the Bartlett window closing method, according to the methods described by Jenkins and Watts (1968). Truncation point (L) values of 100 through 2000 were tested, and L=1600 was

determined to be a reasonable stopping point for all scans. At this bandwidth, major features of the sample spectrum have converged from previous bandwidths, but the estimator has not yet destabilized and become erratic. Estimates ranging from L=600 to L=1600 are included in the analyses here. The dominant peaks were identified by visual inspection. These results are shown in Figure 4.6.

In the Indiana Limestone, the shape of the sample spectrum remains relatively unchanged after reaction. Most of the variance is accounted for by the lowest-frequency peak around f = $5x10^{-4}$ (~2000 slices), as is to be expected (Jenkins & Watts, 1968). It is inadvisable to draw any hard conclusions from this frequency because its period is approximately the same length as the full dataset so only one full period was observed, but it is of note that the peak remained post-reaction. In the pre-reaction scan, three other prominent peaks were identified, and two of these (3 and 4) may have merged into a single peak (3) after reaction. The differences are subtle for this sample, yet they point towards a trend that was observed more strongly in the other two samples: the sample spectrum post-reaction is simpler and explained by fewer, lower-frequency peaks.

In the Edwards Sample, the shape of the sample spectrum density function is approximately the same again pre- and post-reaction, but the higher-frequency peaks (2 and 3) have diminished post-reaction, and the low-frequency peak (1) is much steeper and narrower. This indicates that more of the variance is explained by the low-frequency peak and the high-frequency signals are less important after reaction.

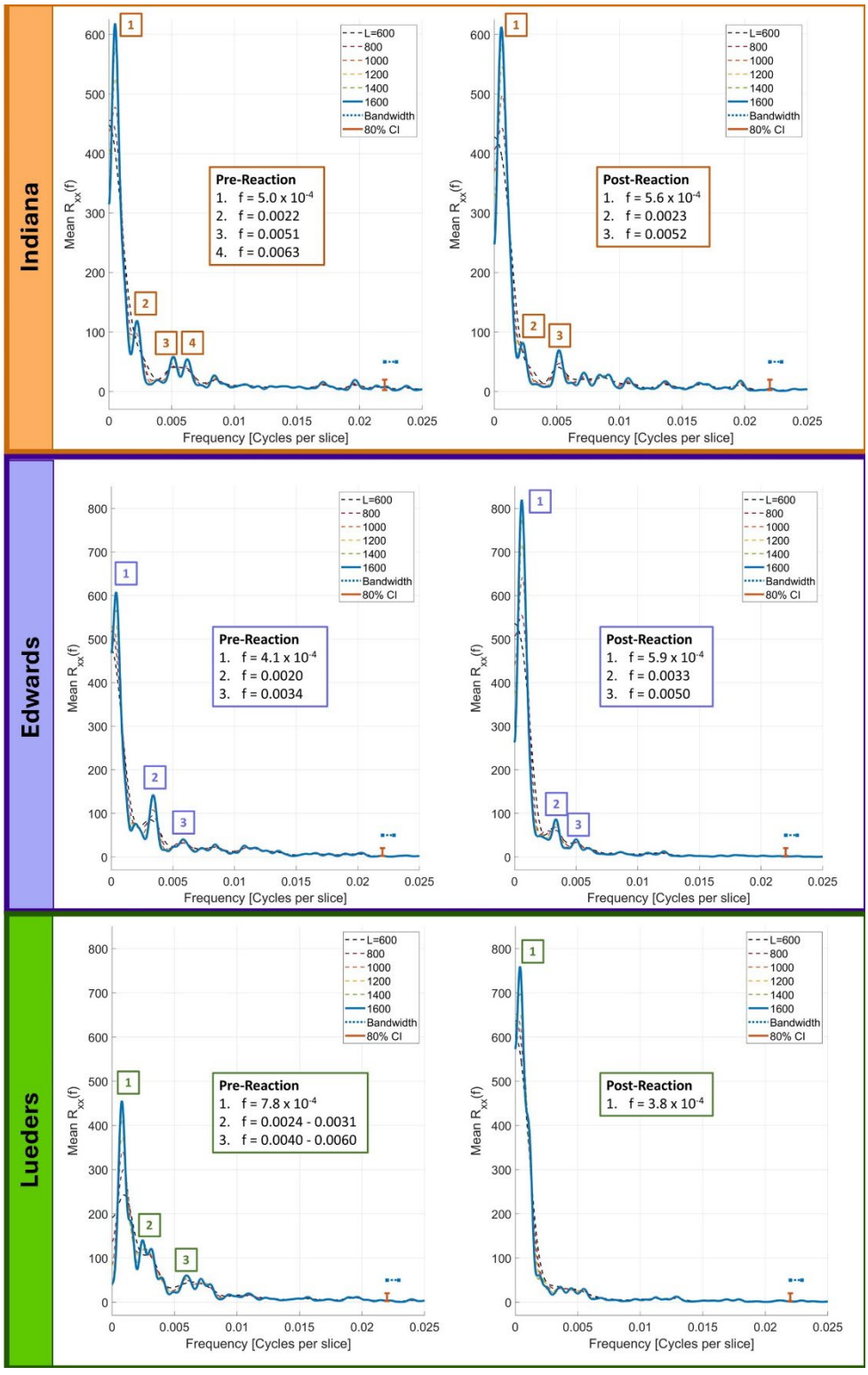

Figure 4.6: Sample spectrum density functions for pre- (left) and post- (right) reaction. Wider bandwidths tested are shown in dashed lines, and the selected stopping bandwidth is shown in bold blue. The 80% confidence interval about this function is shown in orange. Prominent peaks are numbered, and their corresponding frequencies are listed.

The Lueders Limestone sample shows a noticeably more complex pre-reaction spectral density function, with a large peak at low frequency (1) and two clusters of higher-frequency peaks (2 and 3). After reaction, the high-frequency peaks have all but disappeared, and the low-frequency peak is again narrower and steeper than pre-reaction.

These results suggest two main takeaways:

(1) The spectral signal is simplified post-reaction, such that more of the variance is explained by the low-frequency oscillations. So, while the overall post-reaction variance has increased, the smaller-scale heterogeneities that were important pre-reaction have less influence after acid-driven dissolution.

(2) As the spectral signal gets simpler and lower frequencies become more dominant, a larger REV becomes necessary to capture the full picture of pore space heterogeneity. This is agreeable with the observation that smaller-scale heterogeneities lessen in importance: a lower-resolution but larger-scale REV may be preferable to characterize the samples after acid-driven dissolution.

The preferential flowpath that developed in each core was isolated from the post-reaction XCT scan. The FD of the pre-reaction pore space was compared to the FD of the post-reaction preferential flowpath for each 2D image slice from each rock. This resulted in 2000 data points for each of the three rocks (excluding two points from the Lueders Limestone that showed scanning artifacts). These data were considered in aggregate, shown in Figure 4.7. The results show a strong positive correlation between the pre-reaction pore space FD and the post-reaction preferential flow path FD ($R^2 = 0.80$). This suggests that high pore space complexity is associated with higher preferential flow path complexity. A least squares linear regression may

therefore be useful for predicting large-scale regions of higher or lower flowpath complexity in a system with multiple units with different pore space properties, but it loses some utility when observing variation within an individual unit. The data in this regression are clustered by rock, indicating that there is greater variability between rocks than among any given rock (for both the predictor and response variables). This model fits the Lueders data (green) moderately well, but consistently underestimates the response variable for the Indiana datapoints (orange) and consistently overestimates the response variable for the Edwards datapoints (purple), making it challenging to interpret the predictive capability of the pre-reaction pore space FD within any given core.

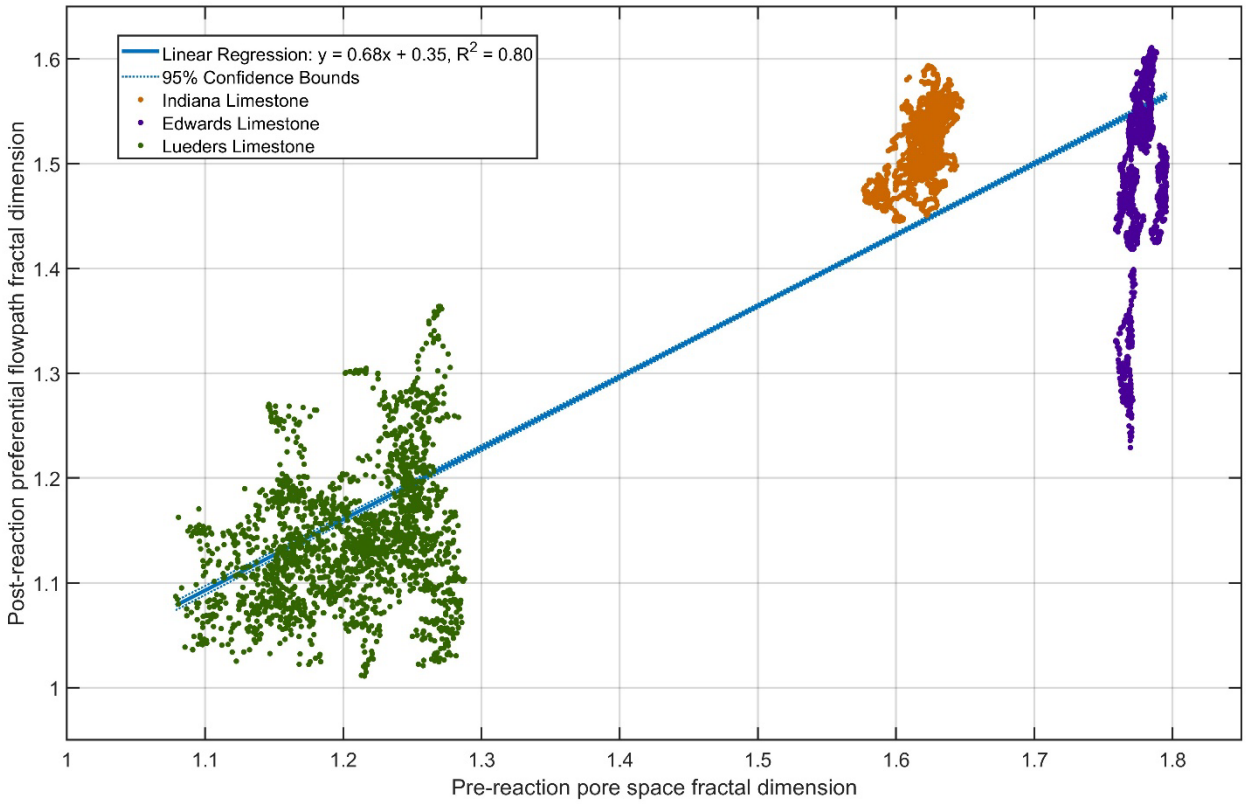

Figure 4.7: Pre-reaction pore space FD versus post-reaction preferential flowpath FD, fitted with a least-squares linear regression ($R^2 = 0.80$). Data are color-coded by rock: Lueders in green, Indiana in orange, and Edwards in purple.

4.5 Conclusions

Predicting the evolution of carbonate rock properties under the influence of acid-driven dissolution is essential for the development of sustainable subsurface energy technologies. Small-scale heterogeneities have been found to have an impact on upscaled reservoir behavior, but it is not always known to what extent. Optimizing the scale at which observations are collected and systems are simulated will be crucial for advancing these technologies. XCT is an excellent tool for analyzing laboratory-scale physical characteristics because it is nondestructive and widely available. In this study, the fractal dimension of the pore space was computed from XCT data before and after acid core flooding of three limestone samples.

The correlation function of the fractal dimension along the direction of flow was found to increase after reaction for all three samples. This suggests that the scale of heterogeneity increased as a result of reaction, and a larger field of view would be necessary to fully capture the variability of the pore fractal dimension than was needed prior to reaction. The along-core fractal dimension was analyzed as a spectral series, and for all three samples the series simplified and was dominated by lower-frequency signals after reaction. This suggests that smaller-scale heterogeneities that contributed to overall variance prior to reaction lessened in importance. It indicates that a larger sample size will be necessary to fully represent the variability in geometric complexity, but also that lower resolution is likely sufficient after reaction.

Each core formed a large preferential flowpath during dissolution. The flowpath was isolated from XCT datasets and its fractal dimension along the length of the core was compared to the fractal dimension of the initial pore space. When all datapoints for all samples were considered in aggregate, there was a good positive correlation between these two variables, suggesting that rock samples with more complex pore space yield more complex branching in

preferential flowpaths. However, there was little to no correlation within any core, suggesting that heterogeneities in pore space along the length of the core are not predictive of locations of complex branching and channeling at the sub-core scale. These findings contribute to a growing body of research investigating the scales of heterogeneity in carbonates and their influence on reactive transport behavior.

4.6 References

Alfonso, I., Beltrán, A., Abatal, M., Castro, I., Fuentes, A., Vázquez, L., & García, A. (2018). Fractal Dimension Determination of Rock Pores by Multi-Scale Analysis of Images Obtained Using OM, SEM and XCT. *Fractals, 26*(05), 1850067. https://doi.org/10.1142/S0218348X18500676

Arganda-Carreras, I., Kaynig, V., Rueden, C., Eliceiri, K. W., Schindelin, J., Cardona, A., & Sebastian Seung, H. (2017). Trainable Weka Segmentation: a machine learning tool for microscopy pixel classification. *Bioinformatics, 33*(15), 2424–2426. https://doi.org/10.1093/bioinformatics/btx180

Babaei, M., & Joekar-Niasar, V. (2016). A transport phase diagram for pore-level correlated porous media. *Advances in Water Resources, 92*, 23–29. https://doi.org/10.1016/j.advwatres.2016.03.014

Boving, T. B., & Grathwohl, P. (2001). Tracer diffusion coefficients in sedimentary rocks: correlation to porosity and hydraulic conductivity. *Journal of Contaminant Hydrology*, *53*(1–2), 85–100. https://doi.org/10.1016/S0169-7722(01)00138-3

Busenberg, E., & Plummer, L. N. (1986). *A comparative study of the dissolution and crystal growth kinetics of calcite and aragonite* (Studies in Diagenesis No. 1578). U.S. Geological Survey.

Carroll, S., Hao, Y., Smith, M., & Sholokhova, Y. (2013). Development of scaling parameters to describe CO2–rock interactions within Weyburn-Midale carbonate flow units. *International Journal of Greenhouse Gas Control, 16*, S185–S193. https://doi.org/10.1016/j.ijggc.2012.12.026

Costa, A. (2023). Hausdorff (Box-Counting) Fractal Dimension. Matlab Central File Exchange. Retrieved from https://www.mathworks.com/matlabcentral/fileexchange/30329-hausdorff-box-counting-fractal-dimension

Elson, J. M., Rahn, J. P., & Bennett, J. M. (1983). Relationship of the total integrated scattering from multilayer-coated optics to angle of incidence, polarization, correlation length, and

roughness cross-correlation properties. *Applied Optics, 22*(20), 3207. https://doi.org/10.1364/AO.22.003207

Fu, J., & Yu, Y. (2019). Experimental Study on Pore Characteristics and Fractal Dimension Calculation of Pore Structure of Aerated Concrete Block. *Advances in Civil Engineering, 2019*, 1–11. https://doi.org/10.1155/2019/8043248

Hao, Y., Smith, M. M., & Carroll, S. A. (2019). *Multiscale modeling of CO2-induced carbonate dissolution: From core to meter scale*. International Journal of Greenhouse Gas Control, 88, 272–289. https://doi.org/10.1016/j.ijggc.2019.06.007

Jenkins, G. M., & Watts, D. G. (1968). *Spectral analysis and its applications*. San Francisco, Calif.: Holden-Day.

Kalia, N., & Balakotaiah, V. (2007). Modeling and analysis of wormhole formation in reactive dissolution of carbonate rocks. *Chemical Engineering Science, 62*(4), 919–928. https://doi.org/10.1016/j.ces.2006.10.021

Lai, P., Moulton, K., & Krevor, S. (2015). Pore-scale heterogeneity in the mineral distribution and reactive surface area of porous rocks. *Chemical Geology, 411*, 260–273. https://doi.org/10.1016/j.chemgeo.2015.07.010

Liu, Min, & Mostaghimi, P. (2017). Characterisation of reactive transport in pore-scale correlated porous media. *Chemical Engineering Science, 173*, 121–130. https://doi.org/10.1016/j.ces.2017.06.044

Liu, Ming, Zhang, S., & Mou, J. (2012). Fractal nature of acid-etched wormholes and the influence of acid type on wormholes. *Petroleum Exploration and Development, 39*(5), 630–635. https://doi.org/10.1016/S1876-3804(12)60086-X

Maheshwari, P., Ratnakar, R. R., Kalia, N., & Balakotaiah, V. (2013). 3-D simulation and analysis of reactive dissolution and wormhole formation in carbonate rocks. *Chemical Engineering Science, 90*, 258–274. https://doi.org/10.1016/j.ces.2012.12.032

Mandelbrot, B. (1967). How Long Is the Coast of Britain? Statistical Self-Similarity and Fractional Dimension. *Science, 156*(3775), 636–638. https://doi.org/10.1126/science.156.3775.636

Menke, H. P., Bijeljic, B., Andrew, M. G., & Blunt, M. J. (2015). Dynamic Three-Dimensional Pore-Scale Imaging of Reaction in a Carbonate at Reservoir Conditions. *Environmental Science & Technology, 49*(7), 4407–4414. https://doi.org/10.1021/es505789f

Menke, H. P., Reynolds, C. A., Andrew, M. G., Pereira Nunes, J. P., Bijeljic, B., & Blunt, M. J. (2018). 4D multi-scale imaging of reactive flow in carbonates: Assessing the impact of heterogeneity on dissolution regimes using streamlines at multiple length scales. *Chemical Geology, 481*, 27–37. https://doi.org/10.1016/j.chemgeo.2018.01.016

Morrow, N., & Buckley, J. (2006). *Wettability and Oil Recovery by Imbibition and Viscous Displacement from Fractured and Heterogeneous Carbonates* (Technical Report No. DE-FC26-02NT15344). University of Wyoming. Retrieved from https://www.osti.gov/servlets/purl/888663

Mostaghimi, P., Liu, M., & Arns, C. H. (2016). Numerical Simulation of Reactive Transport on Micro-CT Images. *Mathematical Geosciences, 48*(8), 963–983. https://doi.org/10.1007/s11004-016-9640-3

Pereira Nunes, J. P., Blunt, M. J., & Bijeljic, B. (2016). Pore-scale simulation of carbonate dissolution in micro-CT images. *Journal of Geophysical Research: Solid Earth, 121*(2), 558–576. https://doi.org/10.1002/2015JB012117

Siddiqui, S., Nasr-El-Din, H. A., & Khamees, A. A. (2006). Wormhole initiation and propagation of emulsified acid in carbonate cores using computerized tomography. *Journal of Petroleum Science and Engineering, 54*(3–4), 93–111. https://doi.org/10.1016/j.petrol.2006.08.005

Thompson, E. P., & Ellis, B. R. (2023). Persistent Homology as a Heterogeneity Metric for Predicting Pore Size Change in Dissolving Carbonates. *Water Resources Research, 59*(9), e2023WR034559. https://doi.org/10.1029/2023WR034559

Thompson, E. P., Tomenchok, K., Olson, T., & Ellis, B. R. (2021). Reducing User Bias in X-ray Computed Tomography-Derived Rock Parameters through Image Filtering. *Transport in Porous Media, 140*(2), 493–509. https://doi.org/10.1007/s11242-021-01690-3

Wu, Y., Tahmasebi, P., Lin, C., Zahid, M. A., Dong, C., Golab, A. N., & Ren, L. (2019). A comprehensive study on geometric, topological and fractal characterizations of pore systems in low-permeability reservoirs based on SEM, MICP, NMR, and X-ray CT experiments. *Marine and Petroleum Geology, 103*, 12–28. https://doi.org/10.1016/j.marpetgeo.2019.02.003

Zhang, K., Pang, X., Zhao, Z., Shao, X., Zhang, X., Li, W., & Wang, K. (2018). Pore structure and fractal analysis of Lower Carboniferous carbonate reservoirs in the Marsel area, Chu-Sarysu basin. *Marine and Petroleum Geology, 93*, 451–467. https://doi.org/10.1016/j.marpetgeo.2018.03.027

Zhang, Y., Jiang, F., & Tsuji, T. (2022). Influence of pore space heterogeneity on mineral dissolution and permeability evolution investigated using lattice Boltzmann method. *Chemical Engineering Science, 247*, 117048. https://doi.org/10.1016/j.ces.2021.117048

Zhou, N., Wang, M., Lu, S., Dodd, T. J. H., Liu, W., & Guan, Y. (2022). Evolution of Fractal Pore Structure in Sedimentary Rocks. *Earth and Space Science, 9*(6). https://doi.org/10.1029/2021EA002167

Chapter 5 Conclusions

5.1 Conclusions and implications

This dissertation contributes to a growing body of research in using imaging technology to characterize carbonate rock core samples and predict their behavior when subjected to acid-driven dissolution. Prior work suggests that pore space heterogeneities at the scales observed in the laboratory may influence behavior at the reservoir scale, but it is not known to what extent (An et al., 2020; Babaei & Joekar-Niasar, 2016; Erfani et al., 2019; Guo et al., 2020; Liu & Mostaghimi, 2017; Navarre-Sitchler & Jung, 2017). Most of the efforts to quantify this impact have been computational (An et al., 2020; Babaei & Joekar-Niasar, 2016; Erfani et al., 2019; Guo et al., 2020; Liu & Mostaghimi, 2017; Navarre-Sitchler & Jung, 2017). These provide useful context for expected results and the ability to forecast many scenarios, but they cannot capture the full scope of complexities present in natural systems. Prior experimental studies have been largely qualitative in nature (Al-Khulaifi et al., 2017; Menke et al., 2017). In this dissertation, I have developed quantitative metrics of heterogeneity from X-ray computed tomography (XCT) imagery of natural carbonate samples and tested their ability to predict various aspects of pore space evolution during dissolution observed in laboratory studies.

The research presented in **Chapter 2** studied the impact of image processing filters on petrophysical properties derived from XCT data. The use of three image filters in succession was found to result in significant improvement in the accuracy and precision of porosity estimates in limestones when digitally derived values were compared to experimental values. XCT data are

commonly used to estimate system porosity because XCT analysis is nondestructive and widely available. Porosity is used for other downstream estimates of petrophysical properties, including permeability, which is an essential input for reservoir-scale simulations of flow. Estimates of porosity depend on segmentation of XCT data into pore and mineral space, a process that can be highly subjective and prone to user bias (Deng et al., 2016; Iassonov et al., 2009; Leu et al., 2014; Pini & Madonna, 2016). Reducing the impact of user bias is essential for making objective assessments of core samples and their influence on potential project viability. This work is particularly impactful because it finds improvements for benchtop XCT scanners, which are lower resolution than synchrotron scanners but much more widely available and commonly used.

In **Chapter 3**, a novel approach to studying the pore space in XCT scans of rock cores was applied and yielded new insight into the evolution of pore space during dissolution. Persistent topology is a tool borrowed from algebraic topology that quantitatively describes topological features. When applied to imaging data of rock samples, it can provide detailed information about the size, connectivity, and spatial distribution of pore space (Suzuki et al., 2021). Each of these (size distribution, pore network connectivity, and pore spatial distribution) has been studied independently, but persistent topology allows the simultaneous investigation of all three parameters. Prior research has found persistent topology to be an effective predictor of nonreactive flow characteristics and percolation behavior (Dong & Blunt, 2009; Herring et al., 2019; Moon et al., 2019; Robins et al., 2016, p. 201; Suzuki et al., 2021). Some recent numerical simulation studies have found persistent topology to correlate well with dissolution front formation, but prior to this work no known studies had performed experimental work to benchmark the topological changes that occur in a pore network due to chemical reaction (Lisitsa et al., 2020; Prokhorov et al., 2022). Our study found permeability changes to be driven by the

growth of large, connected pores. The largest connected pore body in each section of the core was isolated, and its size change was studied. It was found that the largest of the large pores saw little size increase, whereas locally large pores that were smaller than their neighbors grew substantially. The ability to isolate specific regions where pore growth is expected can help optimize the computational efficiency of modeling work. This work also reinforces the validity of using the relatively low-resolution XCT data available from benchtop XCT scanners for analysis and predictive work. The most important pore spaces for permeability development in all three samples studied were well above the spatial resolution of benchtop XCT scanners.

Chapter 4 applies another metric of heterogeneity derived from XCT data – the pore space fractal dimension – to quantitatively describe the pore network's geometric complexity. The fractal dimension along the length of the core was studied using spectral analysis before and after acid-promoted dissolution. This revealed the dominant frequencies of along-core heterogeneity that contributed to variance. In all three samples studied, the post-reaction spectral signals were dominated by lower-frequency signals; higher-frequency signals lessened in importance or disappeared altogether. This is important because it reveals the changes in the relevant scales of heterogeneity that occur as a result of chemical reaction. As preferential flowpaths develop as the rocks dissolve, small heterogeneities are washed out. This suggests that in modeling such a system, a larger spatial scale of observation at lower resolution would be preferable for capturing the variability in pore space complexity. Optimizing spatial scales and resolution (while maximizing computational processing efficiency) is crucial for upscaling laboratory work to the meter and kilometer scale. This is an early step advancing our understanding of how reactive transport processes translate across scales in natural systems. In addition, the preferential flowpath that developed in each rock sample was isolated and its fractal

dimension was studied. We observed a good positive correlation between the pore space complexity and the branching complexity of the preferential flowpath when all three samples were considered, but poor correlation within any one sample. This suggests that the pore space complexity analyzed from XCT data is a good predictor of how much that rock will branch versus channel. It also suggests that sub-centimeter perturbations in geometric complexity are not as important for determining branching locations. This helps optimize the scales at which we characterize sample heterogeneity and use those characterizations to inform larger models.

In summary, this dissertation advances the field of reactive transport in porous media through the following contributions:

(1) Improving the estimates of primary rock characteristics gathered from XCT, a commonly used imaging technology. This will improve the accuracy of downstream parameters derived from these data and therefore confidence in predictions of system viability and performance.

(2) Identifying regions within a core where the greatest increases in pore size are expected. This will aid in optimizing modeling resolution for system performance.

(3) Determining how spatial scales of heterogeneity evolve during dissolution. This will help modeling efforts by optimizing the scale at which heterogeneities are observed and represented in numerical simulations of reactive flow.

(4) Identifying samples that are expected to experience complex branching or channeling preferential flowpaths. This will aid in larger-scale predictions of the spatial extent of reaction that will be expected.

(5) Demonstrating the efficacy of three tools from applied mathematics and statistics (persistent homology, fractal dimension, and spectral analysis) for analyzing 3D

imagery data and predicting the evolution of limestone pore spaces during dissolution. Interdisciplinary work in the sciences and engineering is essential for understanding the interplay between designed systems and the natural world.

5.2 Future work

Advancement of the work in this dissertation follows three suggested lines of inquiry:

(1) *Furthering our understanding of how imaging and image processing affect rock parameter estimates.* The work published in Chapter 2 tested the effects of image processing parameters on XCT-derived porosity, permeability, and pore size distribution based on binary segmentation. Binary segmentation is still the predominant method in the field, but some efforts have used a three-phase segmentation approach (pore, mineral, mixed) to quantify sub-voxel pore space and its impact on total porosity (Qajar et al., 2013; Qajar & Arns, 2022). Further research is necessary to optimize the XCT imaging and processing parameters to obtain accurate results for macro- and micro-porosity from imaging data with >1 μm voxel size.

In addition, there is ample opportunity for furthering the impact of image processing optimization by studying its impact on downstream rock parameter estimates. The work in Chapter 2 mostly focused on porosity, which is a primary parameter often used to extrapolate to other rock properties. A case study was performed on one sample to test the consistency of pore size distribution and permeability estimates compared to experimental data. The pore size distribution analysis was limited by the differences in resolution between imaging and experimental technology. The micro-porosity optimization described above would allow this work to continue with more samples with different pore size distributions. The permeability analysis was done using a computational fluid dynamics model, but the size and resolution of the model was limited by computing resources. Future work would apply high performance

computing resources to gain further understanding of these samples at higher resolution and size. Finally, other parameters including pore network coordination number and other inputs into pore network models, Betti number and other topological metrics, mineral composition, and impacts on reactive transport modeling results all merit investigation.

(2) *Optimizing scales of observation and analysis*. As computational researchers apply the knowledge gained in laboratory experiments to their numerical simulations at the meter to kilometer scale, it is critical to optimize the scale at which we capture sample heterogeneity to maximize processing efficiency. The work in Chapters 3 and 4 suggests that the most influential changes in the pore space as a result of dissolution tend to occur at larger scales than the minimum resolution we can observe using microscopic methods. Furthermore, the results of Chapter 4 suggest that the relevant scales of heterogeneity tend to increase after dissolution has occurred. To validate these findings, investigation at multiple scales is recommended. This would ideally involve the imaging of smaller cores at higher resolution and larger cores at coarser resolution to determine if the same results hold. Results of this area of investigation would help reservoir-scale modelers maximize simulation efficiency by selecting the most relevant grid size for parameter representation.

(3) *Investigating dominant frequencies of heterogeneity.* In Chapter 4 we introduced the use of spectral analysis of a spatially discretized dataset to observe changes in the dominant frequencies of fractal dimension heterogeneity in three carbonate rock samples. XCT data is well-suited to this analytical approach because it generates thousands of images of a sample along the length of the flowpath. This opens many opportunities for analyzing the spectral signal of other rock parameters – porosity, mean pore size, pore size variance, pore correlation length, micropore fraction, and more – and how they change during dissolution. Quantifying changes in

these dominant frequencies can help to optimize the scales of heterogeneity that we study and track in dissolving carbonate systems. This analysis could aid in the development of reservoir-scale simulations of flow through engineered subsurface systems before and after permeability promotion with acid dissolution.

5.3 References

Al-Khulaifi, Y., Lin, Q., Blunt, M. J., & Bijeljic, B. (2017). Reaction Rates in Chemically Heterogeneous Rock: Coupled Impact of Structure and Flow Properties Studied by X-ray Microtomography. *Environmental Science & Technology, 51*(7), 4108–4116. https://doi.org/10.1021/acs.est.6b06224

An, S., Hasan, S., Erfani, H., Babaei, M., & Niasar, V. (2020). Unravelling Effects of the Pore-Size Correlation Length on the Two-Phase Flow and Solute Transport Properties: GPU-based Pore-Network Modeling. *Water Resources Research, 56*(8). https://doi.org/10.1029/2020WR027403

Babaei, M., & Joekar-Niasar, V. (2016). A transport phase diagram for pore-level correlated porous media. *Advances in Water Resources, 92*, 23–29. https://doi.org/10.1016/j.advwatres.2016.03.014

Deng, H., Fitts, J. P., & Peters, C. A. (2016). Quantifying fracture geometry with X-ray tomography: Technique of Iterative Local Thresholding (TILT) for 3D image segmentation. *Computational Geosciences, 20*(1), 231–244. https://doi.org/10.1007/s10596-016-9560-9

Dong, H., & Blunt, M. J. (2009). Pore-network extraction from micro-computerized-tomography images. *Physical Review E, 80*(3), 036307. https://doi.org/10.1103/PhysRevE.80.036307

Erfani, H., Joekar-Niasar, V., & Farajzadeh, R. (2019). Impact of Microheterogeneity on Upscaling Reactive Transport in Geothermal Energy. *ACS Earth and Space Chemistry, 3*(9), 2045–2057. https://doi.org/10.1021/acsearthspacechem.9b00056

Guo, R., Dalton, L. E., Fan, M., McClure, J., Zeng, L., Crandall, D., & Chen, C. (2020). The role of the spatial heterogeneity and correlation length of surface wettability on two-phase flow in a CO2-water-rock system. *Advances in Water Resources, 146*, 103763. https://doi.org/10.1016/j.advwatres.2020.103763

Herring, A. L., Robins, V., & Sheppard, A. P. (2019). Topological Persistence for Relating Microstructure and Capillary Fluid Trapping in Sandstones. *Water Resources Research, 55*(1), 555–573. https://doi.org/10.1029/2018WR022780

Iassonov, P., Gebrenegus, T., & Tuller, M. (2009). Segmentation of X-ray computed tomography images of porous materials: A crucial step for characterization and quantitative analysis of pore structures. *Water Resources Research, 45*(9). https://doi.org/10.1029/2009WR008087

Leu, L., Berg, S., Enzmann, F., Armstrong, R. T., & Kersten, M. (2014). Fast X-ray Micro-Tomography of Multiphase Flow in Berea Sandstone: A Sensitivity Study on Image Processing. *Transport in Porous Media, 105*(2), 451–469. https://doi.org/10.1007/s11242-014-0378-4

Lisitsa, V., Bazaikin, Y., & Khachkova, T. (2020). Computational topology-based characterization of pore space changes due to chemical dissolution of rocks. *Applied Mathematical Modelling, 88*, 21–37. https://doi.org/10.1016/j.apm.2020.06.037

Liu, M., & Mostaghimi, P. (2017). Characterisation of reactive transport in pore-scale correlated porous media. *Chemical Engineering Science, 173*, 121–130. https://doi.org/10.1016/j.ces.2017.06.044

Menke, H. P., Bijeljic, B., & Blunt, M. J. (2017). Dynamic reservoir-condition microtomography of reactive transport in complex carbonates: Effect of initial pore structure and initial brine pH. *Geochimica et Cosmochimica Acta, 204*, 267–285. https://doi.org/10.1016/j.gca.2017.01.053

Moon, C., Mitchell, S. A., Heath, J. E., & Andrew, M. (2019). Statistical Inference Over Persistent Homology Predicts Fluid Flow in Porous Media. *Water Resources Research, 55*(11), 9592–9603. https://doi.org/10.1029/2019WR025171

Navarre-Sitchler, A., & Jung, H. (2017). Complex Coupling of Fluid Transport and Geochemical Reaction Rates: Insights from Reactive Transport Models. *Procedia Earth and Planetary Science, 17*, 5–8. https://doi.org/10.1016/j.proeps.2016.12.004

Pini, R., & Madonna, C. (2016). Moving across scales: a quantitative assessment of X-ray CT to measure the porosity of rocks. *Journal of Porous Materials, 23*(2), 325–338. https://doi.org/10.1007/s10934-015-0085-8

Prokhorov, D., Lisitsa, V., Khachkova, T., Bazaikin, Y., & Yang, Y. (2022). Topology-based characterization of chemically-induced pore space changes using reduction of 3D digital images. *Journal of Computational Science, 58*, 101550. https://doi.org/10.1016/j.jocs.2021.101550

Qajar, J., & Arns, C. H. (2022). Chemically Induced Evolution of Morphological and Connectivity Characteristics of Pore Space of Complex Carbonate Rock via Digital Core Analysis. *Water Resources Research, 58*(3). https://doi.org/10.1029/2021WR031298

Qajar, J., Francois, N., & Arns, C. H. (2013). Microtomographic Characterization of Dissolution-Induced Local Porosity Changes Including Fines Migration in Carbonate Rock. *SPE Journal, 18*(03), 545–562. https://doi.org/10.2118/153216-PA

Robins, V., Saadatfar, M., Delgado-Friedrichs, O., & Sheppard, A. P. (2016). Percolating length scales from topological persistence analysis of micro- CT images of porous materials. *Water Resources Research, 52*(1), 315–329. https://doi.org/10.1002/2015WR017937

Suzuki, A., Miyazawa, M., Minto, J. M., Tsuji, T., Obayashi, I., Hiraoka, Y., & Ito, T. (2021). Flow estimation solely from image data through persistent homology analysis. *Scientific Reports, 11*(1), 17948. https://doi.org/10.1038/s41598-021-97222-6

Appendices

Appendix A: Supplementary Information for Chapter 2

Appendix Table A.1 shows the complete list of XCT scan parameters used in this study.

Appendix Table A.1: XCT scan parameters.

	Indiana Limestone	Edwards Limestone	Berea Sandstone	Berea Sandstone high-res
Beam energy (kV)	180	160	179	68
Beam current (μA)	75	77	65	68
Power (W)	11.7	12.3	11.6	4.6
Magnification	7.102	6.896	6.896	25.006
Exposure (s)	1	1	1	4
Gain (dB)	24	24	24	24
Minimize artifacts	Yes	Yes	Yes	Yes
Optimize	Yes	Yes	Yes	Yes
Frames per projection	4	4	4	4

Appendix Figure A.1 shows the results of the sensitivity analysis performed on different numbers of training regions of interest.

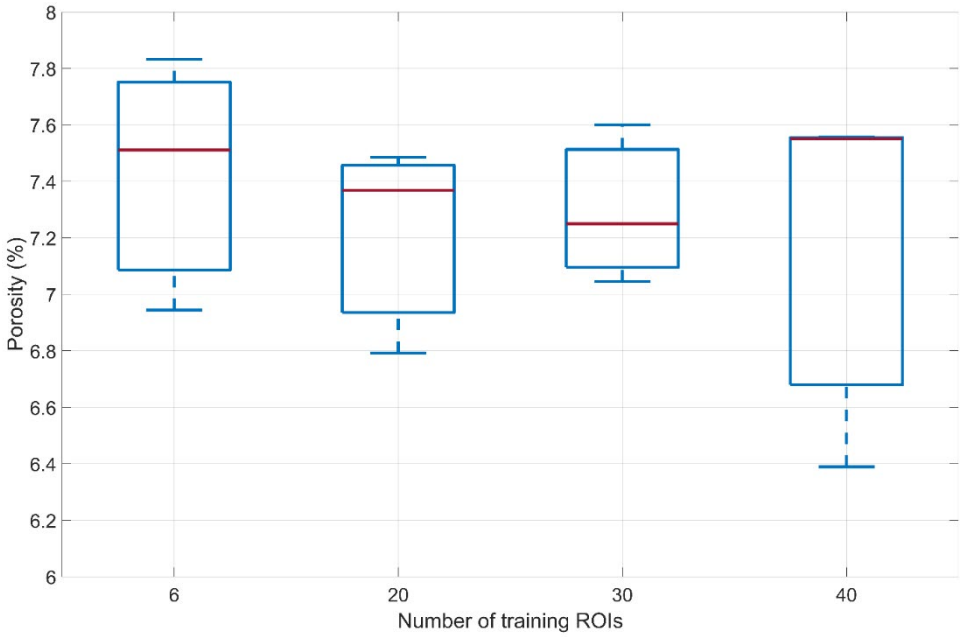

Appendix Figure A.1: Number of training regions sensitivity analysis showing box and whisker plots of porosity values obtained using different numbers of training regions (n=3 for each). Red lines show medians, boxes show 25th through 75th percentiles, and whiskers show most extreme data points.

Appendix Table A.2 shows the results of the sensitivity analysis performed on the disconnect particles parameter. Mean pore radius shows little sensitivity to k above k≈0.2. Standard deviation of pore radius is also relatively insensitive to k except at very low values. This is illustrated in Figure 2.8 by the very similar peaks and widths of the curves corresponding to high k values. Skewness shows the most sensitivity at low k values.

Appendix Table A.2: Disconnect particles parameter sensitivity analysis. This table shows the sensitivity of mean, standard deviation, and skewness to changes in k value from the base case of k=0.7.

k	**Mean pore radius (µm)**	% change from k=0.7 value	**Standard deviation of pore radius (µm)**	% change from k=0.7 value	**Skewness**	% change from k=0.7 value
0	**73.76**	-20.16	**65.41**	19.80	**6.40**	611.29
0.1	**82.07**	-11.17	**65.05**	19.13	**3.06**	240.66
0.2	**88.17**	-4.57	**61.17**	12.04	**1.78**	98.43
0.3	**90.18**	-2.39	**58.74**	7.58	**1.38**	53.50
0.4	**91.15**	-1.34	**57.07**	4.52	**1.17**	30.12
0.5	**91.80**	-0.63	**56.01**	2.59	**1.04**	15.50
0.6	**92.14**	-0.26	**55.08**	0.88	**0.95**	5.87
0.7	**92.39**	--	**54.60**	--	**0.90**	--
0.8	**92.47**	0.10	**54.37**	-0.43	**0.88**	-2.45
0.9	**92.50**	0.12	**54.33**	-0.50	**0.87**	-3.08
1	**92.50**	0.12	**54.33**	-0.50	**0.87**	-3.08

Matlab code used for image analysis is included below.

Matlab Code for bilateral filter parameterization:

```
%Matlab code to find sigma_r parameter for bilateral filter in imageJ


%Input: before running, import Excel sheet ROI2.xls into Matlab. This Excel file has
one
%column per ROI. Rows 1-256 are counts for each intensity value, row 257 is
%the mean intensity value for that ROI, row 258 is the standard deviation.
%There are no header columns or rows.

data = table2array(ROI2WF);               %convert from excel table to an array
sigmaRarray = zeros(1,length(data(1,:))); %initialize

for i = 1:size(data,2)
    mu = data(257,i);                     %mean intensity for ith ROI
    sigma = data(258, i);                 %stdev intensity for ith ROI
    alpha = round(mu - sigma);            %starting value of alpha=mean-stdev
    if alpha<1
        alpha=1;
    end
    beta = round(mu + sigma);             %starting value of beta=mean+stdev
    if beta>258
        beta = 258;
    end

    histo=0;                              %initialize

    while histo < 0.95                    %stop when 95% of values are included in
range
        histo = sum(data(alpha:beta,i))/sum(data(1:256,i));
        val = beta-alpha;                 %range
                if alpha > 1
                    alpha = alpha - 1;    %step bottom bound down by one
                else
                    alpha = 1;            %keep alpha=1 if already at lowest possible
value
                end
                if beta < 256
                    beta = beta + 1;      %step upper bound up by one
                else
                    beta = 256;           %keep beta=256 if already at highest
possible value
                end
    end
    sigmaRarray(i)=val;
end

sigmaR = max(sigmaRarray)
```

Matlab Code for beam hardening correction:

```
% code to import stack of images from imagej
%
% Before running:
% 1) update fname name to import a new stack
% 2) update image input parameters (nX, nY, limitval, zshift)
fname = 'IndianaLS01_Post1_bilateral.tif';
info = imfinfo(fname);
imageStack = zeros(963,963); %change to size of image
numberOfImages = length(info);
for k = 1:numberOfImages
    currentImage = imread(fname, k, 'Info', info);
    imageStack(:,:,k) = currentImage;
end

% imageStack is variable A for Beam Hardening Function to be applied
A = imageStack;

% adjust parameters in BHC_Function before running
[CorrectedStack] = BHC_function(A);

% we achieved "CorrectedStack Variable" after BHC_function
% convert each layer of stack to tiff with same file output
imwrite(CorrectedStack(:,:,1),'IndianaLS01_Post1_BH.tif');
for i = 2:size(CorrectedStack, 3)
imwrite(CorrectedStack(:,:,i),'IndianaLS01_Post1_BH.tif','WriteMode','append');
end

function [CorrectedStack] = BHC_function(A)
% To find coefficients “a” of best fit to a function expressed by: MTMa = MTf
% M_corr = BH corrected image
% Surfacefit = Surface fit values

% Image input parameters (update for each new stack)
nX=963; % X dimension of the input image
nY=963; % Y dimension
limitval=0; %This is the value for black background on my image (min set by auto in
imagej, which is 0)
zshift=118; % This can be changed according to image grey-scale range, this value is
what imagej shows the average to be

% Main function
for i = 1:size(A,3) %create for loop to apply function to each slice
    slice = A(:,:,i);
[r,c,v] = find(slice > limitval);
M= zeros(size(c,1),6);
M(:,1)=1;
M(:,2)=c; % x indices
```

```
M(:,3)=r; % y indices
M(:,4)=c.^2;
M(:,5)=c.*r;
M(:,6)=r.^2;

cyl = slice > limitval; % To extract the grey-scale value of only the object material
of the 2-D slice.
R = cyl.*slice;
[m,n,f]= find(R);
a = (M'*M)\(M'*f);
p = a(1).*M(:,1)+ a(2).*M(:,2)+ a(3).*M(:,3)+ a(4).*M(:,4)+ a(5).*M(:,5)+
a(6).*M(:,6);
corr= f - p + zshift;
S = sparse(r, c, corr, nX, nY);
M_corr=full(S);
p1=sparse(r, c, p, nX,nY);
Surfacefit=full(p1);
M_corr=uint16(M_corr); %corrected slice

output(:,:,i) = M_corr; %inputing each new corrected slice into a 3-D matrix
end

CorrectedStack = output;
end
```

Appendix B: Supplementary Information for Chapter 3

Appendix Table B.1 shows the X-ray computed tomography (XCT) scan parameters used in this study. Appendix Table B.2 shows values used to estimate Damköhler and Péclet numbers. Appendix Figure B.1 shows XCT imagery of preferential flowpaths near the inlet of each rock sample. Appendix Figure B.2-4 show three figures of 1st dimension persistence diagrams (PDs) for the three rock cores used in this study. Each figure shows PDs from the section closest to the inlet and the section closest to the outlet at three stages of dissolution. Appendix Figure B.5 shows boxplots of 1st dimension persistence values before and after reaction.

Appendix Table B.1: XCT scan parameters.

	Edwards Limestone	Indiana Limestone	Lueders Limestone
Beam energy (kV)	169	175	170
Beam current (µA)	74	74	76
Power (W)	12.5	13.0	13.330
Magnification	13.330	13.337	13.330
Voxel size (µm)	15	15	15
Exposure time (s)	1	1	1
Gain (dB)	24	24	24
Minimize ring artifacts	Yes	Yes	Yes
Frames per projection	2	2	2
Filter	None	None	None

Appendix Table B.2: Values used to calculate dimensionless parameters to describe reactive flow regime.

Parameter	Variable	Units	Indiana	Edwards	Lueders	Source
Porosity	φ	--	0.154	0.244	0.138	MIP data
Length	L	m	4.08×10^{-2}	4.00×10^{-2}	4.08×10^{-2}	Measured
Diameter	d	m	2.50×10^{-2}	2.50×10^{-2}	2.50×10^{-2}	Measured
Cross-sectional area	A	m^2	4.91×10^{-4}	4.91×10^{-4}	4.91×10^{-4}	Calculated
Core volume	V	m^3	2.00×10^{-5}	1.96×10^{-5}	2.00×10^{-5}	Calculated
Sample mass	m	kg	3.89×10^{-2}	4.58×10^{-2}	4.78×10^{-2}	Measured
Pore volume	V_p	m^3	3.08×10^{-6}	4.79×10^{-6}	2.76×10^{-6}	Calculated
Pore characteristic lengthscale	l	m	1.01×10^{-5}	4.99×10^{-6}	1.56×10^{-4}	MIP data
Equilibrium concentration Ca^{2+}	C_{eq}	$mol\text{-}m^{-3}$	0.976	0.976	0.976	Modeled in Visual MINTEQ
Reaction rate	r	$mol\text{-}m^{-2}\text{-}s^{-1}$	8.91×10^{-5}	8.91×10^{-5}	8.91×10^{-5}	Busenberg & Plummer (1986)
Specific surface area	SSA	$m^2\text{-}g^{-1}$	0.34	0.20	0.79	Lai et al. (2015); Morrow et al. (2006)
Reactive surface area	SA	m^2	13.2	9.20	37.7	SA = SSA * m
Characteristic time of reaction	τ_{rxn}	s	0.003	0.006	0.001	$\tau\_rxn=\varphi*V*Ceq/(r*SA)$

Diffusivity	D	m^2-s	1 x 10^{-11}	1 x 10^{-11}	1 x 10^{-11}	Boving & Grathwohl (2001)
Dynamic viscosity	μ	Pa-s	8.90 x 10^{-4}	8.90 x 10^{-4}	8.90 x 10^{-4}	Constant for water at 20 C
Density of water	ρ	kg-m^{-3}	998.21	998.21	998.21	Constant for water at 20 C
Kinematic viscosity	ν	m^2-s^{-1}	8.92 x 10^{-7}	8.92 x 10^{-7}	8.92 x 10^{-7}	Constant for water at 20 C
Flowrate	Q	m^3-s^{-1}	3.33 x 10^{-7}	5.00 x 10^{-7}	1.67 x 10^{-8}	Measured
Reynolds number	Re	--	0.050	0.023	0.043	$Re = \rho u L/\mu$
Peclet number	Pe	--	1.80 x 10^7	1.67 x 10^7	1.00 x 10^6	$Pe=uL/D$
Characteristic time of advection	τ_{adv}	s	9.25	9.58	166	$\tau_{adv} = V_p/Q$
Damköhler number	Da	--	3.6 x 10^3	1.7 x 10^3	2.1 x 10^5	$Da = \tau_{adv}/\tau_{rxn}$

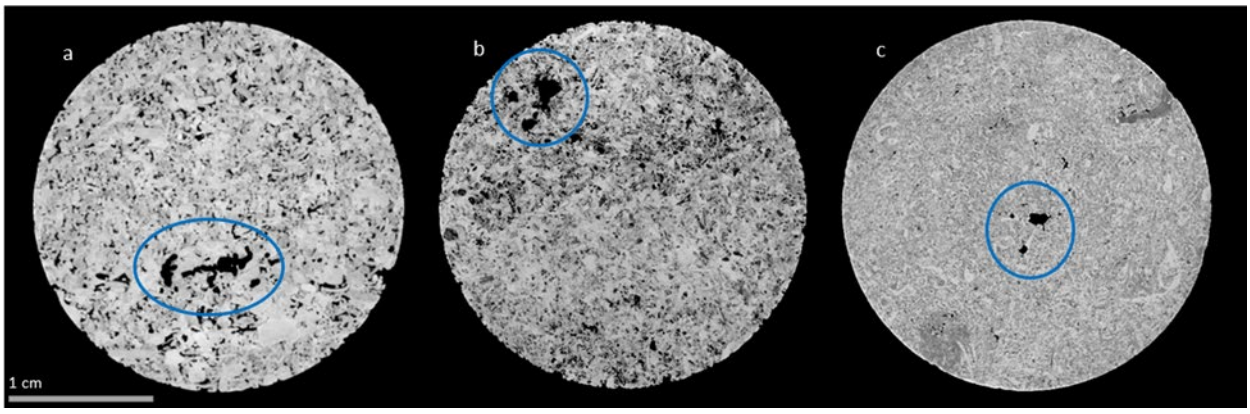

Appendix Figure B.1: Large preferential flowpaths visible in XCT data for (a) Indiana, (b) Edwards, and (c) Lueders Limestones.

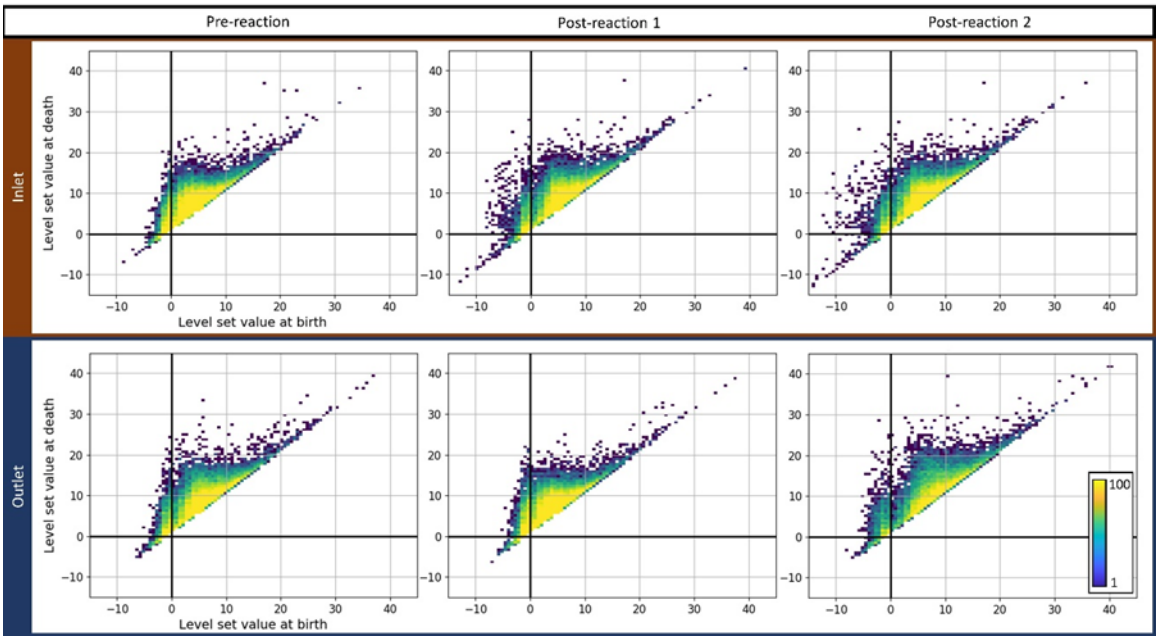

Appendix Figure B.2: 1st dimension persistence diagrams for Indiana Limestone at three stages of reaction, near inlet (top) and outlet (bottom) of core.

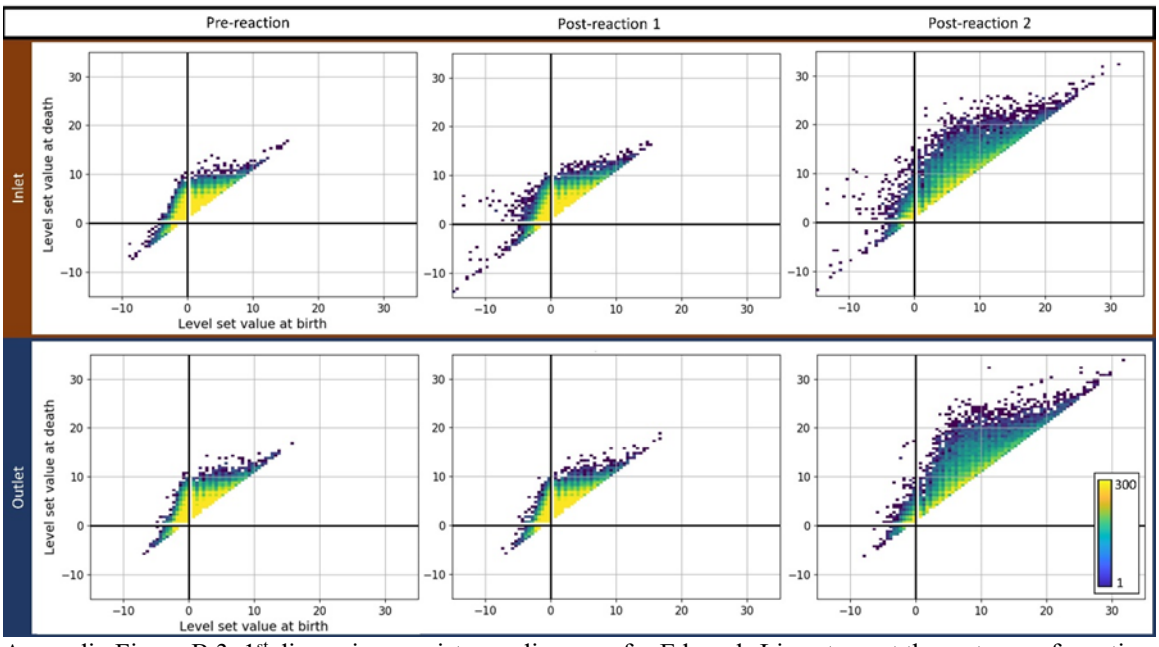

Appendix Figure B.3: 1st dimension persistence diagrams for Edwards Limestone at three stages of reaction, near inlet (top) and outlet (bottom) of core.

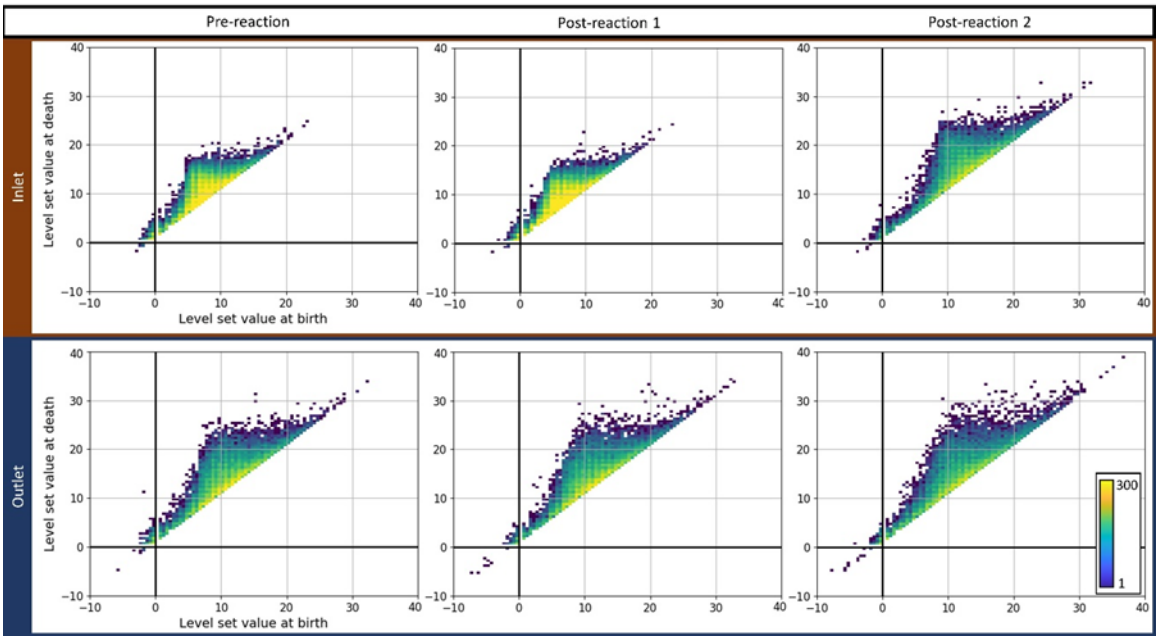

Appendix Figure B.4: 1st dimension persistence diagrams for Lueders Limestone at three stages of reaction, near inlet (top) and outlet (bottom) of core.

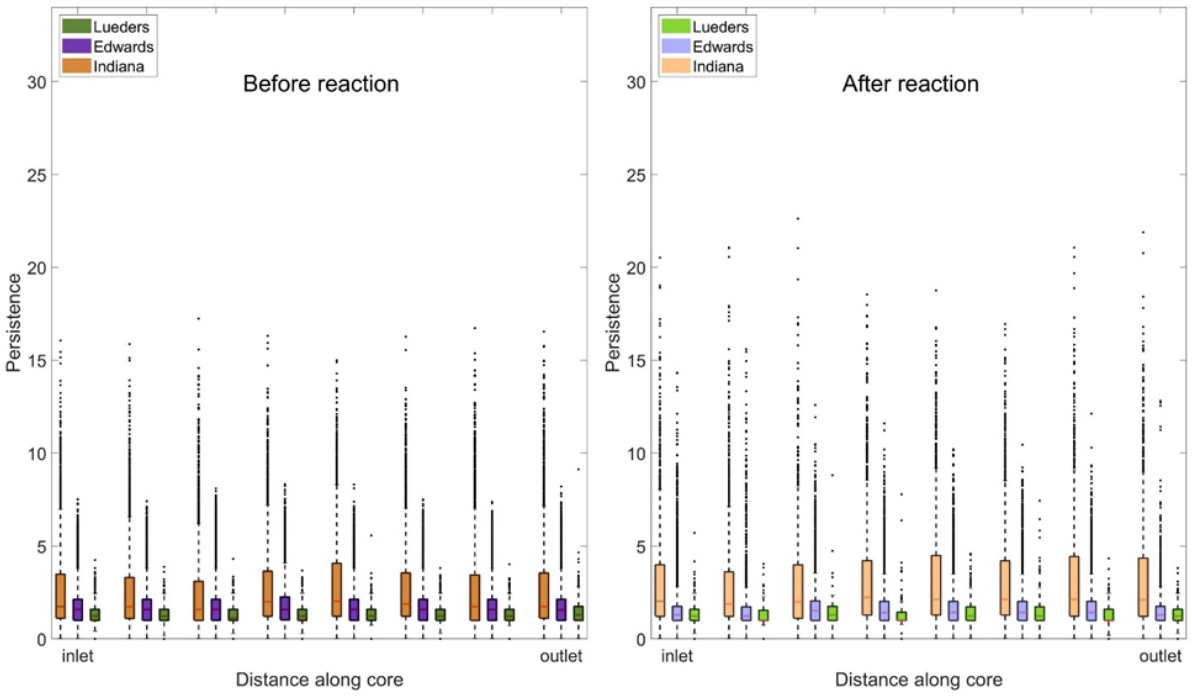

Appendix Figure B.5: Persistence values of 1st dimension topological features from Q2 and Q3 before and after reaction. In each boxplot, the red line indicates the median, the boxes show the 25th-75th percentiles, whiskers extend to 1.5 IQR beyond the boxes. Pre-reaction distributions are in dark colors, post-reaction distributions are in light colors, and outliers are shown with black dots.

Appendix C: Supplementary Information for Chapter 4

Appendix Table C.1: XCT scan parameters. Reproduced from Thompson & Ellis (2023).

	Edwards Limestone	Indiana Limestone	Lueders Limestone
Beam energy (kV)	169	175	170
Beam current (μA)	74	74	76
Power (W)	12.5	13.0	13.330
Magnification	13.330	13.337	13.330
Voxel size (μm)	15	15	15
Exposure time (s)	1	1	1
Gain (dB)	24	24	24
Minimize ring artifacts	Yes	Yes	Yes
Frames per projection	2	2	2
Filter	None	None	None

Appendix Table C.2: Values used to calculate dimensionless parameters to describe reactive flow regime. Reproduced from Thompson & Ellis (2023).

Parameter	Variable	Units	Indiana	Edwards	Lueders	Source
Porosity	φ	--	0.154	0.244	0.138	MIP data
Length	L	m	4.08×10^{-2}	4.00×10^{-2}	4.08×10^{-2}	Measured
Diameter	d	m	2.50×10^{-2}	2.50×10^{-2}	2.50×10^{-2}	Measured
Cross-sectional area	A	m^2	4.91×10^{-4}	4.91×10^{-4}	4.91×10^{-4}	Calculated
Core volume	V	m^3	2.00×10^{-5}	1.96×10^{-5}	2.00×10^{-5}	Calculated
Sample mass	m	kg	3.89×10^{-2}	4.58×10^{-2}	4.78×10^{-2}	Measured

Pore volume	V_p	m^3	3.08×10^{-6}	4.79×10^{-6}	2.76×10^{-6}	Calculated
Pore characteristic lengthscale	l	m	1.01×10^{-5}	4.99×10^{-6}	1.56×10^{-4}	MIP data
Equilibrium concentration Ca^{2+}	C_{eq}	$mol\text{-}m^{-3}$	0.976	0.976	0.976	Modeled in Visual MINTEQ
Reaction rate	r	$mol\text{-}m^{-2}\text{-}s^{-1}$	8.91×10^{-5}	8.91×10^{-5}	8.91×10^{-5}	Busenberg & Plummer (1986)
Specific surface area	SSA	$m^2\text{-}g^{-1}$	0.34	0.20	0.79	Lai et al. (2015); Morrow et al. (2006)
Reactive surface area	SA	m^2	13.2	9.20	37.7	SA = SSA * m
Characteristic time of reaction	τ_{rxn}	s	0.003	0.006	0.001	τ_rxn=φ*V*Ceq/(r*SA)
Diffusivity	D	$m^2\text{-}s$	1×10^{-11}	1×10^{-11}	1×10^{-11}	Boving & Grathwohl (2001)
Dynamic viscosity	μ	Pa-s	8.90×10^{-4}	8.90×10^{-4}	8.90×10^{-4}	Constant for water at 20 C
Density of water	ρ	$kg\text{-}m^{-3}$	998.21	998.21	998.21	Constant for water at 20 C
Kinematic viscosity	ν	$m^2\text{-}s^{-1}$	8.92×10^{-7}	8.92×10^{-7}	8.92×10^{-7}	Constant for water at 20 C
Flowrate	Q	$m^3\text{-}s^{-1}$	3.33×10^{-7}	5.00×10^{-7}	1.67×10^{-8}	Measured

Reynolds number	Re	--	0.050	0.023	0.043	$Re = \rho u L/\mu$
Peclet number	Pe	--	1.80×10^7	1.67×10^7	1.00×10^6	$Pe=uL/D$
Characteristic time of advection	τ_{adv}	s	9.25	9.58	166	$\tau_{adv} = V_p/Q$
Damköhler number	Da	--	3.6×10^3	1.7×10^3	2.1×10^5	$Da = \tau_{adv}/\tau_{rxn}$